Dust masses for a large sample of core-collapse supernovae from optical emission line asymmetries: dust formation on 30-year time-scales

Maria Niculescu-Duvaz,[1] M. J. Barlow [ID],[1]★ A. Bevan [ID],[1] R. Wesson [ID],[1] D. Milisavljevic,[2] I. De Looze [ID],[3] G. C. Clayton [ID],[4] K. Krafton,[4] M. Matsuura [ID][5] and R. Brady[1]

[1]*Department of Physics and Astronomy, University College London, Gower Street, London WC1E 6BT, UK*
[2]*Department of Physics and Astronomy, Purdue University, 525 Northwestern Avenue, West Lafayette, IN 47907, USA*
[3]*Sterrenkundig Observatorium, Ghent University, Krijgslaan 281 – S9, B-9000 Gent, Belgium*
[4]*Department of Physics and Astronomy, Louisiana State University, Baton Rouge, LA 70803, USA*
[5]*School of Physics and Astronomy, Cardiff University, Cardiff CF24 3AA, UK*

ABSTRACT

Modelling the red–blue asymmetries seen in the broad emission lines of core-collapse supernovae (CCSNe) is a powerful technique to quantify total dust mass formed in the ejecta at late times (>5 yr after outburst) when ejecta dust temperatures become too low to be detected by mid-infrared (IR) instruments. Following our success in using the Monte Carlo radiative transfer code DAMOCLES to measure the dust mass evolution in SN 1987A and other CCSNe, we present the most comprehensive sample of dust mass measurements yet made with DAMOCLES, for CCSNe aged between 4 and 60 yr after outburst. Our sample comprises multi-epoch late-time optical spectra taken with the Gemini/Gemini Multi-Object Spectrographs (GMOS) and Very Large Telescope (VLT) X-Shooter spectrographs, supplemented by archival spectra. For the 14 CCSNe that we have modelled, we confirm a dust mass growth with time that can be fit by a sigmoid curve that is found to saturate beyond an age of $\sim$30 yr, at a mass of $0.23^{+0.17}_{-0.12}$ M$_\odot$. For an expanded sample including dust masses found in the literature for a further 11 CCSNe and six CCSN remnants, the dust mass at saturation is found to be $0.42^{+0.09}_{-0.05}$ M$_\odot$. Uncertainty limits for our dust masses were determined from a Bayesian analysis using the affine invariant Markov chain Monte Carlo ensemble sampler EMCEE with DAMOCLES. The best-fitting line profile models for our sample all required grain radii between 0.1 and 0.5 μm. Our results are consistent with CCSNe forming enough dust in their ejecta to significantly contribute to the dust budget of the Universe.

Key words: supernovae: general – supernovae: individual: SN 1957D – supernovae: individual: SN 1970G – supernovae: individual: SN 1979C – dust, extinction – ISM: supernova remnants.

1 INTRODUCTION

Since the discovery of large amounts of dust in highly redshifted young galaxies (e.g. Bertoldi et al. 2003; Watson et al. 2015; Laporte et al. 2017), the origin of the bulk of the cosmic dust in the Universe has been debated. It has been proposed that a significant fraction of cosmic dust, particularly at high redshifts, is formed in the ejecta of core-collapse supernovae (CCSNe), with Morgan & Edmunds (2003) and Dwek, Galliano & Jones (2007) estimating that each CCSN would need to produce $\geq$0.1 M$_\odot$ of dust for this to be the case. Theoretical models predict that CCSNe can form $>$0.1 M$_\odot$ of dust (Nozawa et al. 2003; Sarangi & Cherchneff 2015). However, in theoretical simulations the amount of ejecta-formed dust found to be destroyed by the reverse shock has varied between 0 and 100 per cent depending on the details of the simulation (Nath, Laskar & Shull 2008; Silvia, Smith & Michael Shull 2010; Bocchio, Jones & Slavin 2014; Micelotta, Dwek & Slavin 2016; Kirchschlager et al. 2019; Slavin et al. 2020; Priestley et al. 2021). A more comprehensive knowledge of dust masses, grain sizes, and radial locations is needed

for a range of different types of CCSNe of different ages in order to inform dust destruction simulations.

Over the last few decades, the capability of CCSNe to form large amounts of dust has been well established. Model fits to the spectral energy distributions (SEDs) of warm dust emitting at mid-infrared (IR) wavelengths as measured with the *Spitzer Space Telescope* found dust masses of only around 10^{-4}–10^{-2} M$_\odot$ to be present in CCSNe and supernova remnants (SNRs), less than the theoretical predictions (Sugerman et al. 2006; Rho et al. 2009; Fabbri et al. 2011). This changed with the work of Matsuura et al. (2011), who used *Herschel Space Observatory* observations of SN 1987A taken 23 yr after outburst to probe previously undetectable cold dust emitting at far-IR wavelengths and found a cold dust mass of $\sim$0.5 M$_\odot$. Follow-up Atacama Large Millimeter/submillimeter Array (ALMA) observations of SN 1987A (Indebetouw et al. 2014) resolved this dust component to be in the centre of the remnant. Since then, far-IR data have been utilized to detect cold dust masses of 0.04–1.0 M$_\odot$ in several SNRs, including Cas A, with ages ranging from several hundred to several thousand years old (Gomez et al. 2012; De Looze et al. 2017, 2019; Temim et al. 2017; Chawner et al. 2019; Priestley, Barlow & De Looze 2019; Niculescu-Duvaz et al. 2021).

★ E-mail: mjb@star.ucl.ac.uk

There is a current lack of far-IR or submillimetre telescopes with sensitivities sufficient to detect supernovae beyond the Local Group, and existing observations have only been able to detect cold dust in nearby Galactic and Magellanic Cloud core-collapse supernova remnants (CCSNRs). However, Lucy et al. (1989) showed for SN 1987A that dust located within the emitting gas can produce a red–blue line asymmetry in the broad-line profiles. This effect is caused by light from the receding redshifted side of a CCSNe being attenuated by more dust than light from the approaching blueshifted side. Since then, many authors have noted the presence of red–blue asymmetries in the line profiles of CCSNe (e.g. Smith, Foley & Filippenko 2008 for SN 2006jc; Mauerhan & Smith 2012 for SN 1998S; and Gall et al. 2014 for SN 2010jl), while Milisavljevic et al. (2012) presented a sample of 10 late-time CCSN spectra that all displayed varying degrees of blueshifted emission peaks in their optical line profiles.

We note that Anderson et al. (2014) discussed the observed blueshifting of Hα emission peaks during the very early post-explosion phases of Type II CCSNe and attributed this to the Hα emission line formation radius during such early phases being at or within the effective photospheric radius of the expanding ejecta, with much of the redshifted Hα emission consequently occulted by the photospheric disc. However, they showed from theoretical modelling that by epochs greater than $\sim$150 d post-explosion the effective photospheric radius should have moved within the formation zone for Hα emission line photons, with no blueshifting of Hα emission peaks by this mechanism predicted beyond this epoch, in agreement with observations. Any subsequent blueshifting of emission line peaks can therefore be attributed to the effects of newly formed dust within the ejecta.

To increase the number of CCSNe with known dust mass determinations, Bevan & Barlow (2016) presented the Monte Carlo radiative transfer code DAMOCLES that quantifies the amount of newly formed dust causing absorption and scattering of supernova ejecta line emission. It is able to treat arbitrary dust/gas geometries, a range of velocity and density distributions, and dust and gas clumping configurations, as well as handling a wide range of grain species and radii. Bevan & Barlow (2016) used DAMOCLES to model the line profiles in the optical spectra of SN 1987A between 714 and 3604 d, allowing them to determine the ejecta-condensed dust mass. Their results were in agreement with the work of Wesson et al. (2015) for epochs in common, showing a steady increase in dust mass with time and that by day 3604 the dust mass in SN 1987A was $\sim$0.1 M$_\odot$. Since the dust mass on days 8500–9200 had reached 0.6–0.8 M$_\odot$ (Matsuura et al. 2011; Wesson et al. 2015), most of the dust in this CCSN must have formed after day 3604. Bevan, Barlow & Milisavljevic (2017) also applied DAMOCLES to model the line profiles of three other objects, SN 1980K, SN 1993J, and Cas A, finding ejecta dust masses ranging from 0.1 M$_\odot$ for SN 1993J to 1.1 M$_\odot$ for Cas A.

Wesson et al. (2015) tracked the dust mass evolution in SN 1987A over its first 25 yr by modelling its optical to far-IR SEDs, where they found the dust mass grew from 3×10^{-3} M$_\odot$ at 615 d to 0.8 M$_\odot$ at 9200 d. Wesson et al. (2015) noted that large grains >2 μm in radius were required to fit the SED of SN 1987A at late epochs. Wesson et al. (2015) were able to fit a sigmoid curve to SN 1987A's slow dust mass evolution with time. The dust mass evolution over a period of 10 yr in SN 2005ip, quantified from red–blue line asymmetry fits by Bevan et al. (2019), confirmed the dust-growth trend seen for SN 1987A by Wesson et al. (2015). A similar trend for SN 2010jl at early epochs is also seen (Gall et al. 2014; Bevan et al. 2020). Theoretical predictions of dust mass growth in CCSNe do not agree with these trends, with e.g. Sarangi & Cherchneff (2015) and Sluder,

Milosavljević & Montgomery (2018) predicting that most of the dust should form quite rapidly, within the first 3 yr post-explosion.

Dwek, Sarangi & Arendt (2019) have argued that this dichotomy can be resolved if ejecta dust masses actually grow to their final values within 2–3 yr, with most of the dust initially hidden in optically thick clumps – with the continued expansion of the ejecta these clumps would eventually become optically thin, revealing the full dust mass. However, by combining DAMOCLES optical line profile modelling with MOCASSIN optical–IR SED modelling, Wesson & Bevan (2021) have shown that SN 1987A cannot have formed a dust mass larger than 0.01 M$_\odot$ by day 1000, even with optically thick clumps. Dust masses larger than this value that can fit the observed SED cannot match the observed optical line profiles and dust masses larger than 0.01 M$_\odot$ that can fit the observed line profiles cannot fit the observed SED.

Independent evidence for the slow growth of supernova dust with time has come from the work of Liu et al. (2018), whose study of pre-solar SiC dust grains from supernovae used the radioactive ^{49}V–^{49}Ti chronometer to show that the dust grains formed at least 2 yr, and most likely 10 yr, after the parent star had exploded. This time-scale is consistent with the work of Ott et al. (2019), who measured barium isotope ratios in supernova-condensed dust grains found in primitive meteorites, and inferred that the dust grains had condensed about 20 yr after explosion.

The time at which CCSN observational dust mass growth plateaus or saturates is still unclear, as the dust-mass growth curve is still sparsely sampled in the evolutionary stage between a supernova and an SNR, at ages between 20 and 100 yr. It is around this stage where the effect of the reverse shock on the ejecta dust also starts to become significant, so it is particularly important to determine the dust masses in CCSNe of a similar age to and older than SN 1987A. It can also be argued that even for earlier times there are not yet enough CCSN dust mass estimates available to be able to discern correlations between dust mass, grain radius, and CCSN properties such as progenitor mass and SN subtype. In this work, we aim to increase the sample of CCSNe that have derived dust masses with robustly quantified uncertainties across a range of ages. We also try, where possible, to constrain the dust grain radius and composition.

The spectra that are modelled in this paper are drawn from a Gemini/Gemini Multi-Object Spectrographs (GMOS) and Very Large Telescope (VLT) X-Shooter late-time survey of CCSN spectra (Wesson et al., in preparation). For their sample they selected CCSNe that had been discovered before 2013 and which, with a few exceptions, had occurred in host galaxies at distances <30 Mpc. From the 306 initially selected CCSNe, they retained the CCSNe covered by *Hubble Space Telescope* (*HST*) optical images taken after the explosion date. In addition, in order to avoid confusion by dense star fields, they only selected CCSNe that were located in more isolated galaxy parts. The final X-Shooter plus GMOS sample consisted of 55 CCSNe that had exploded between 1957 and 2012. Broad emission lines were detected from 14 of these supernovae. The modelling of the line profiles of 12 of these objects using DAMOCLES is reported in this paper. DAMOCLES models for a 13th, SN 2005ip, have already been published by Bevan et al. (2019), while DAMOCLES models for the 14th, SN 1995N, are reported by Wesson et al. (submitted). For eight of the CCSNe that had X-Shooter or GMOS spectral detections, we were able to supplement those data with archival spectra, which also provided us with late-time spectra of two further CCSNe, SN 1993J and SN 1998S, that have broad-line detections.

As discussed by Wesson et al. (in preparation), a key characteristic that appears to be required for very late time emission from CCSNe to be detectable is the presence of strong interactions between the

Table 1. Gemini GMOS observations – details of targets modelled in this work.

Name	Date	Epoch (d)	Program	Exp. time (s)	Central λ (Å)	Galaxy	D (Mpc)	SN Type
SN 1957D	24 Apr 2015	20 949	GS-2015A-Q-53	3 × 900	5970	NGC 5236	4.6	II
SN 1957D	7 Mar 2018	22 010	GS-2018A-Q-311	6 × 1200	5970	NGC 5236		
SN 1970G	22 May 2016	16 733	GN-2016A-Q-85	4 × 900	5225	NGC 5457	6.7	II-L
SN 1979C	16 Apr 2015	13 150	GN-2015A-Q-56	3 × 600	5970	NGC 4321	15.0	II-L
SN 1979C	12 May 2017	13 907	GN-2017A-Q-72	12 × 600	5970			
SN 1980K	23, 24 Apr 2016	12 988	GN-2016A-Q-85	4 × 900	5225	NGC 6946	7.7	II-L
SN 1980K	8, 12 May 2018	13 734	GN-2018A-Q-313	6 × 1200	5970			
SN 1986E	9 Apr 2015	10 588	GN-2015A-Q-56	3 × 900	5970	NGC 4302	17.0	II-L
SN 1986E	17 Apr 2018	11 692	GN-2018A-Q-313	6 × 900	5970	NGC 4302		
SN 2004et	28 Apr 2015	3849	GN-2015A-Q-56	3 × 900	5225	NGC 6946	7.7	II-P
SN 2004et	25 Apr 2017	4577	GN-2017A-Q-72	12 × 600	5970	NGC 6946		
SN 2007it	19 Apr 2015	2775	GS-2015A-Q-53	3 × 900	5970	NGC 5530	12.0	II
SN 2007it	1 Mar 2018	3822	GS-2018A-Q-311	6 × 1200	5970	NGC 5530		
SN 2010jl	22 Jan 2016	1906	GN-2016A-Q-85	4 × 900	5225	UGC 5189A	49	IIn
SN 2011ja	26 Feb 2014	807	GS-2014A-Q-70	6 × 900.48	5970	NGC 4945	3.6	II
SN 2011ja	9 Jun 2015	1275	GS-2015A-Q-53	3 × 900	5970	NGC 4945		
SN 2011ja	17 Feb 2018	2259	GS-2018A-Q-311	6 × 1200	5970	NGC 4945		

Table 2. ESO VLT X-Shooter observations – details of targets modelled in this work.

Name	Date	Epoch (d)	OB ID	UVB (s)	VIS (s)	NIR (s)	Galaxy	D (Mpc)	SN Type
Programme 097.D-0525(A)									
SN 1957D	08 June 2016	21 360	1342702	1145.76	1051.76	6 × 200	NGC 5236	4.6	II
SN 1957D	26 Jan 2017	21 592	1342707	1145.76	1051.76	6 × 200	NGC 5236		
SN 1957D	27 Jan 2017	21 593	1342710	1145.76	1051.76	6 × 200	NGC 5236		
SN 1957D	28 Jan 2017	21 598	1342713	1145.76	1051.76	6 × 200	NGC 5236		
SN 1996cr	10 May 2016	7360	1343004	1145.76	1051.76	6 × 200	ESO 097−13	4.2	IIn:
SN 1996cr	12 May 2016	7362	1343009	1145.76	1051.76	6 × 200	ESO 097−13		
SN 1996cr	08 June 2016	7389	1343012	1145.76	1051.76	6 × 200	ESO 097−13		
SN 2011ja	10 May 2016	1611	1342667	1145.76	1051.76	6 × 200	NGC 4945	3.6	II
SN 2011ja	10 May 2016	1611	1342671	1145.76	1051.76	6 × 200	NGC 4945		
SN 2011ja	10 May 2016	1611	1342674	1145.76	1051.76	6 × 200	NGC 4945		
Programme 0103.D-0281(A)									
SN 1996cr	01 May 2019	8446	2292225	1522.00	1500.00	5 × 300	ESO 097−13	4.2	IIn:
SN 1996cr	29 May 2019	8474	2291103	1522.00	1500.00	5 × 300	ESO 097−13		

supernova ejecta and circumstellar material (Fesen et al. 1999; Milisavljevic et al. 2012). Such interactions may make broad-line emission from the ejecta detectable through one or all of these mechanisms: (a) irradiation of ejecta material by X-ray and ultraviolet (UV) photons emitted from shocked interaction regions (Wesson et al., in preparation); (b) emission from a reverse shock propagating back into the ejecta (Fesen & Weil 2020); or (c) ejecta emission from heating by a pulsar wind nebula (e.g. the Crab Nebula or SN 1957D; Long et al. 2012; Owen & Barlow 2015). The dust responsible for blueshifting the emission line peaks must be located either in, or interior to, the line-emitting material.

2 OBSERVATIONS

Most of the optical spectra we model in this work are from the Gemini GMOS and VLT X-Shooter late-time spectroscopic survey of CCSNe presented by Wesson et al. (in preparation), where fuller details of the observations can be found. A summary of the GMOS and X-Shooter spectra modelled in this work can be found in Tables 1 and 2. For some objects we also model archival data or unpublished spectra, which are summarized in Table 3.

The Gemini GMOS-South (GMOS-S) and GMOS-North (GMOS-N) spectra generally cover the range 4400–7500 Å. All spectra were obtained in long-slit mode using the B600 grating, with a slit width of 0.75 arcsec. The spectra were taken at two or three central wavelength settings and coadded to prevent important spectral features from falling in detector gaps. The spectra have a resolution of 3.5 Å at a wavelength of 6000 Å. The 2D spectra were bias-corrected, flat-fielded, and wavelength calibrated using the IRAF GEMINI package, and corrected for cosmic rays using the LACOS package of Van Dokkum (2001). The sky subtraction regions were determined by visual inspection and the spectra were extracted using 15 rows centred on the supernova's position.

The X-Shooter spectra were taken in integral field unit (IFU) mode, with a field of view of 4 × 1.8 arcsec², using an effective slit width of 0.6 arcsec. The spectral resolving powers were 8600 for the 3000–5600 Å UVB region and 13 500 for the 5500–10 200 Å VIS region. Objects were acquired using blind offsets from nearby stars, and extracted from a circular aperture with a radius of 1 arcsec, and sky subtracted using an annulus with inner–outer radii of 1–2 arcsec. The data were reduced using the software package REFLEX (Freudling et al. 2013), which is implemented in the KEPLER workflow engine and automated the data reduction process.

Table 3. Summary of archival/supplementary supernova spectra modelled in this work.

SN	Epoch (d)	Type	Host galaxy	D (Mpc)	Reference
1957D	11 371	II	NGC 5236	4.0	Long, Blair & Krzeminski (1989)
	19 459				Long et al. (2012)
1970G	16 693	II-L	NGC 5457	6.7	This paper
1979C	5146	II-L	NGC 4321	15.0	Fesen et al. (1999)
	10 575				Milisavljevic et al. (2009)
1980K	12 977	II-L	NGC 6946	7.7	This paper
1986E	3712	II-L	NGC 4302	17.0	Cappellaro, Danziger & Turatto (1995)
1993J	8417	IIn	M81	3.6	This paper
1996cr	3603	IIn	ESO 097−13	4.2	Bauer et al. (2008)
1998S	258	IIn	NGC 3877	17.0	Fransson et al. (2005)
	440				Fransson et al. (2005)
	1170				Pozzo et al. (2004)
	2148				Fransson et al. (2005)
	6574				Smith et al. (2017)
2004et	646	II-P	NGC 6946	7.7	Fabbri et al. (2011)
2012au	2277	Ib/c	NGC 4790	24.0	Milisavljevic et al. (2018)

For each spectrum the continuum was normalized to unity throughout, using the interactive STARLINK package DIPSO (Howarth et al. 2014).

3 MODELLING RED–BLUE LINE PROFILE ASYMMETRIES USING DAMOCLES

3.1 Methodology

This work is motivated by the overwhelming presence of blueshifted asymmetries in the emission line profiles of CCSNe. Out of a sample of 10 supernovae, Milisavljevic et al. (2012) noted that all the supernova emission lines showed some degree of blueshifting, which they suggested was due to internal dust obscuration. Similarly, upon a visual inspection of our sample of 14 CCSNe, all SNe either exhibited a red scattering wing and/or a blueshifted peak, which can both be caused by dust absorption and scattering. If dust formation in supernovae was less prevalent, and if emission line asymmetries were instead due to physical asymmetries in the ejecta, then for CCSNe older than approximately 300 d we would expect to observe roughly equal numbers having redshifted or blueshifted emission line peaks. This is not the case. Given the statistical significance of this finding, we assume that if the emission line peaks of a supernova are blueshifted, or an extended red scattering wing is present, this is caused by dust internal to the supernova, which we then quantify with the Monte Carlo radiative transfer code DAMOCLES.

DAMOCLES is written in FORTRAN 95, and parallelized with OPENMP. It models line photons subjected to scattering and absorption by dust in expanding ejecta. Total energy conservation is not a requirement, as it is assumed that any packet absorbed by dust would be re-emitted outside the wavelength range of interest and thus no longer contributes to the resulting line profile. In addition to this, the absorption and scattering of radiation by dust is assumed to be independent of the dust temperature. It has been benchmarked (Bevan & Barlow 2016) against analytic models of theoretical line profiles based on work by Gerasimovic (1933), and also against numerical models of SN 1987A produced by Lucy et al. (1989). DAMOCLES is able to treat any arbitrary dust/gas geometry, a range of velocity and density distributions, and dust and gas clumping configurations, as well as handling a wide range of grain species and radii. Our approach to modelling the line profiles follows the same principles as described for SN 1987A by Bevan & Barlow (2016),

where a more detailed description of DAMOCLES can also be found. In all cases, the parameter space was examined manually to find the best-fitting model. The free parameters of the models were the dust mass M_d, grain radius a, outer expansion velocity V_{max}, emitting shell radius ratio R_{in}/R_{out}, and the density profile index β, such that the density profile $\rho \propto r^{-\beta}$.

The manual fitting process can be briefly described as follows: V_{max} is determined from the point at which the observed profile vanishes on the blue side, while V_{min} is constrained by the width of the 'flat-top' region of the emission line profile, i.e. the region between the velocity of the blueshifted peak found at $-V_{min}$ and an inflection point in the profile found at $+V_{min}$. Thus the R_{in}/R_{out} value is set so that the model line profile matches various inflection points of the observed profile, and the density profile β is identified from the gradient of the observed line profile wings. Having fixed these values, we then iterate over the grain radius and dust mass to fit the observed profile (in the case of the Bayesian fitting process described below, the above procedures are done automatically).

We assume that at these late epochs the line-emitting gas is optically thin, with the emissivity distribution proportional to the square of the local gas density. The gas was kept smoothly distributed throughout. We assume that the supernova ejecta is in free expansion, such that $V_{max}t = R_{out}$, where t is the age of the supernova. However, this assumption does not hold for the intermediate-width components (IWCs) or for some hydrogen-emitting shells in some CCSNe models, and the R_{out} of the components is a free parameter in such cases. Unless otherwise specified, we keep the dust and the gas coupled in our simulations (so the smoothly distributed dust and the gas have the same V_{max}, R_{in}/R_{out}, and β values). We adopted intrinsic line flux ratios for the [O III] 4959, 5007 Å, [O II] 7319, 7330 Å, and [O I] 6300, 6363 Å doublets fitted by the DAMOCLES models of 2.98, 1.23, and 3.13, respectively (Zeippen 1987; Baluja & Zeippen 1988; Storey & Zeippen 2000).

We modelled the line profiles using smooth or clumped dust distributions. Clumps were adopted to have radii equal to $R_{out}/40$. The clumped dust models used the same V_{max} and R_{in}/R_{out} parameters as the coupled gas distribution, although distributed by a β_{clump} parameter, the clump distribution power-law index, instead of the β value used for the gas and for smoothly distributed dust models. From a 10D Bayesian model of SN 1987A 714 d post-explosion (Bevan 2018), values of 3 were found to be preferred for the clump distribution power-law index and filling factors of <0.25. We fixed

the clump distribution power-law index to 3 and set the filling factor to 0.10 in order to reduce the number of free parameters required in our models. Varying the clump number density distribution power-law index over values of 1–5 was found to change the dust mass needed to provide a good fit by a factor of ∼3.

We modelled a few SNe where instead of smoothly distributed gas, we used clumped gas coupled to the clumped dust, in order to determine the degree to which gas clumping would affect the derived dust mass. The amount by which the dust mass required to fit the line profiles changed was dependent on the difference between the best-fitting β index, derived from the smoothly distributed dust gas model, and the fixed dust clump number density distribution index of 3. SN 1996cr, for which models required the highest value of β out of the SNe in our sample, was found to require a dust mass 3.5× smaller in order to fit the line profiles when the gas and dust were colocated in clumps. SN 1970G, on the other hand, which was best fitted with a smoothly distributed gas β value of −0.1, required a factor of 2 larger dust mass to fit the Hα line profile when the gas and dust were colocated in clumps.

A clumped dust model will present less of a scattering wing and attenuate the red wing of the line profile less than for a smooth dust model, given no change in other model parameters between the two cases. This is because when the dust is located in clumps, radiation is subject to less scattering and to less absorption. Therefore, for a clumped dust model to match the line profile generated by a smooth dust model, both a small modification to the grain radius to produce a larger albedo and a dust mass larger than for the smooth case by a factor of 1.5–3 are required. Several authors found that dust needed to be present in optically thick clumps in order to reproduce early observations of SN 1987A (Lucy et al. 1989, 1991; Bouchet et al. 1996; Kozma & Fransson 1998). So, for all objects in this work, the final dust masses we report are those found from clumped models, on the grounds that dust is more likely to exist in clumps for the CCSNe in our sample, rather than in a smoothly distributed medium.

Most line profiles can be fit using either 100 per cent amorphous carbon (AmC) or 100 per cent silicate dust with grain sizes with matching albedos, apart from cases where a large red scattering wing requires the dust species to have an albedo greater than 0.7, which could only be achieved by using silicate dust with grain radii in the range 0.1–1.0 μm. For CCSNe where we cannot confirm the grain species but can roughly constrain the grain radius for each species, we present our final dust mass for the object using a 50:50 AmC to astronomical silicate dust species mixture, as some proportion of both carbon grains and silicates are often found to be needed from SED modelling of SN dust, e.g. for Cas A, see Rho et al. (2008), Arendt et al. (2014), and De Looze et al. (2017), while for 1E 0102−7912, see Rho et al. (2009) and Sandstrom et al. (2009).

All models were convolved to the spectral resolution of the optical data. For all figures showing line profile fits to optical data, 'dust-free' and dusty model line profiles are shown. These model line profiles have the same gas distribution, but the dusty model couples this gas distribution to a dust distribution and the dust-free model does not. This is to aid the reader to visualize how adding dust to the simulation affects the shape of the model line profile. The parameters for smooth and clumped AmC and silicate dust species are included in the tables listing model parameters. As was demonstrated in Niculescu-Duvaz et al. (2021), the choice of silicate grain species barely affects the dust optical depth in the optical regime, hence we use astronomical silicate species with the optical constants of Draine & Lee (1984) in our models. Our AmC models use the BE amorphous carbon optical constants of Zubko et al. (1996). For some CCSNe in our sample, the grain radius of the species could not be constrained, often due to

insufficient signal-to-noise ratio (S/N) in the observed line profiles, which also meant an upper limit could not be established on the dust mass. In these cases, we present results using conservative grain sizes for both the smoothly distributed and clumped 100 per cent AmC and 100 per cent silicate dust models to provide a rough estimate of possible dust mass values. For these CCSNe, we provide lower limits to the dust masses, given by the dust mass required to attenuate the line profiles using the grain radius that required the lowest dust masses, which was 0.1 μm for a 50:50 AmC to silicate ratio.

In order to quantify errors on the model parameters, we also conducted a Bayesian analysis on all supernova spectra, with the exception of those that exhibited multiple emission components. The Bayesian approach to modelling line profiles with DAMOCLES is described by Bevan (2018). It combines an affine invariant Markov chain Monte Carlo (MCMC) ensemble sampler, EMCEE (Goodman & Weare 2010; Foreman-Mackey et al. 2013) with DAMOCLES to sample the posterior probability distribution of the input parameters, which is defined by Bayes' theorem:

$$P(\theta|D) \propto P(\theta)P(D|\theta). \tag{1}$$

In this equation, D is the data, θ is the set of parameters of the model, $P(\theta)$ is our prior understanding of the probability of the parameters, and $P(D|\theta)$ is the likelihood, which is the probability of obtaining the data for a given set of parameters. The likelihood function is proportional to $\exp{-\chi_{red}^2}$, where $\chi_{red}^2 = \chi^2/\upsilon$, and υ is the number of degrees of freedom and χ^2 is expressed in equation (2):

$$\chi^2 = \sum_{i=1}^{n} \frac{(f_{mod,i} - f_{obs,i})^2}{\sigma_i^2}. \tag{2}$$

In this equation, $f_{mod,i}$ is the modelled flux in bin i, $f_{obs,i}$ is the observed flux in frequency bin i, and σ_i is the combined Monte Carlo and observational uncertainty in bin i. The modelled line profile from which $f_{mod,i}$ is sampled has its peak normalized to the peak flux of the observed line profile. The priors for each model are given in uniform space, apart from the dust mass and grain radius that span several magnitudes, so they are given in log-uniform space.

The final posterior probability distributions are presented as a series of 2D contour plots, where each pair of parameters is marginalized over the other parameters. A 1D marginalized posterior probability distribution for each parameter is also presented. The 'best-fitting' parameter value from the Bayesian analysis is given as the median of the marginalized 1D probability distribution, as many deviated from a Gaussian distribution. The lower and upper limits represent the 16th and 84th quartiles for the same 1D probability distribution. The Bayesian model fits presented in this work usually use either a 100 per cent AmC or 100 per cent silicate dust composition, and in cases where we present a final dust mass using a 50:50 AmC to silicate dust ratio, which is determined manually, we find the percentage errors on the dust mass from the limits found by the Bayesian analysis and scale them to that value. As we had to run many models, we restricted our parameter space to five dimensions, explored by 250 walkers. For each parameter, the number of iteration steps for the autocorrelation function to initially decay down towards zero can be estimated to be one autocorrelation time. This value was checked for every parameter in every Bayesian model. We checked that each model was run for five or more autocorrelation times to ensure convergence. We also checked the acceptance fraction for each simulation, which averaged at around 0.3.

For emission line profiles where IWCs took up a large part of the profile, we could not use a Bayesian analysis to evaluate the errors, as the Bayesian version of DAMOCLES can only model single

component emission lines. In these cases we used χ^2 estimates to evaluate the goodness of fit, and compared the χ^2 values of dusty and dust-free models. We present a χ^2 value for every dusty model. The uncertainty limits on our final dust mass are then given by a 35 per cent variation in χ^2 when varying only the dust mass and fixing all other parameters, as this value leads to uncertainties on the dust mass that are of a similar magnitude to the uncertainties found from Bayesian inference.

3.2 Application to CCSNe

3.2.1 SN 1957D

SN 1957D is the oldest supernova modelled in this work. It was first discovered by H. Gates on 1957 December 28 in M83, when it was well past maximum light, so its exact explosion date is unknown. We adopt an M83 redshift of 0.00115 for SN 1957D (Meyer et al. 2004).

We modelled the [O III] 4959, 5007 Å emission from SN 1957D at 11 371, 19 459, and 21 535 d post-explosion. Observational data for the first two epochs are summarized in Table 3. We combined all the GMOS and X-Shooter spectra of SN 1957D (Tables 1 and 2) to make the nominal day 21 535 spectrum. As we could not constrain the dust species, smooth and clumped AmC and silicate dust models for all epochs can be found in Table 4. Our clumped silicate dust-affected [O III] 4959, 5007 Å line profile models can be found in Figs 1 and 2 for all epochs. From a manual investigation of the parameter space, we found the best-fitting models to the line profile shapes required similar V_{max}, β, and R_{in}/R_{out} for the three epochs, where there appeared to be a possible small increase of dust mass over time. Because of the presence of a persistent red scattering wing, we found that our clumped dusty models required a grain radius of 0.4 μm for 100 per cent AmC grains, 100 per cent silicate dust grains, or a 50:50 carbon to silicate mixture in order to provide the best model fits to the [O III] doublet at all epochs. The derived dust masses at all epochs in SN 1957D were found to be low compared to the dust masses that we find for SN 1979C and SN 1980K at similar epochs. Table 4 lists the derived dust parameters for 100 per cent AmC or 100 per cent silicate compositions. For a 50:50 carbon to silicate mixture the best-fitting dust masses were $0.012^{+0.048}_{-0.012}$, $0.035^{+0.075}_{-0.030}$, and $0.05^{+0.50}_{-0.048}$ M$_\odot$ for days 11 371, 19 459, and 21 535.

In order to constrain the uncertainties on the model parameters, we ran a Bayesian MCMC analysis for days 11 371 and 21 535 of SN 1957D using 100 per cent carbon dust. The resulting corner plot for the day 11 371 model can be found in Fig. A1. We were able to constrain the AmC grain radius at 11 371 d to be >0.1 μm, where the median value of the grain radius 1D posterior probability distribution was 0.3 μm, very similar to our previously estimated grain radius of 0.4 μm. As this was the epoch with the best S/N, we fixed the grain radius derived at this epoch to be the value adopted for our manual models at the other epochs. The dust mass that we had derived for an AmC carbon grain species, from a manual examination of parameter space, was a factor of 2.5 smaller than the median value derived from the 1D posterior probability distribution for the dust mass. We applied the percentage errors taken from the Bayesian analysis to our best-fitting dust mass derived from a manual fit for 50:50 AmC to silicate dust using a grain radius of 0.4 μm, to derive absolute upper and lower limits. The parameters were less well constrained at day 21 535 due to a lower S/N [O III] profile, and the median dust mass was five times less than our best-fitting model for clumped carbon grains, but our manually estimated value was well within the error uncertainties on the dust mass from the Bayesian analysis.

We considered the S/N of the day 19 459 spectrum to be too low to conduct a Bayesian analysis, and instead derived a dust mass of $0.035^{+0.065}_{-0.030}$ M$_\odot$ for a 50:50 AmC to silicate mixture with a grain radius of 0.3 μm, where a dust-free model gave a χ^2 of 1.4, while the dusty models returned an average χ^2 of 0.8.

3.2.2 SN 1970G

SN 1970G was discovered on 1970 July 30 (Detre & Lovas 1970). It is located in the galaxy M101, (for which we adopted a redshift of $z = 0.000811$ from Sabater et al. 2012). It was classified as a Type II-L supernova from its light curve (Young & Branch 1989), although Barbon, Ciatti & Rosino (1979) considered that it could be a transitional object between II-P and II-L,

As the red wing of the Hα profile was cut off in our GMOS-N spectrum of SN 1970G taken at 16 733 d post-explosion, we combined it with a Multiple Mirror Telescope (MMT) spectrum taken 16 693 d post-explosion, averaging to an epoch of 16 713 d. Both spectra had detections of broad Hα 6563 Å and [O I] 6300, 6363 Å, with a weaker detection of [O III] 4959, 5007 Å. The GMOS spectrum was convolved to the resolution of the MMT spectrum of 7Å. Unfortunately, part of the red wing in the MMT spectrum was tainted by what appears to be an absorption feature and by nebular [S II] 6717, 6731 Å emission. These were removed from the Hα line before modelling with DAMOCLES. We omit models of the [O I] 6300, 6363 Å line due to low S/N and the blending of its red wing with the Hα line.

Our DAMOCLES models for SN 1970G were constructed for an age of 16 713 d, with the best-fitting clumped silicate dust models for the Hα profile shown in Fig. 3. The parameters for the smooth and for the clumped AmC and silicate dust models are listed in Table 4. The grain radius or grain species cannot be well constrained from the Hα line, due to gaps in the line profile in the red wing. We thus present conservative grain radius estimates for both smoothly distributed and clumped 100 per cent AmC and 100 per cent silicate dust models. The clumped dust mass derived from the best fits to the Hα profile ranges from 0.02 M$_\odot$ for a 100 per cent AmC dust distribution to 0.1 M$_\odot$ for a 100 per cent silicate distribution. All the dusty models had a lower χ^2 value than for the dust-free case ($\chi^2 = 1.58$). We found a marginal improvement of the χ^2 value for a 100 per cent silicate dust model over a 100 per cent amorphous carbon model. Therefore, our preferred dust mass for SN 1970G is $0.10^{+1.22}_{-0.097}$ M$_\odot$, where the limits are taken from a Bayesian inference.

A similar χ^2 value can be obtained by decoupling the Hα emitting gas from the dust, which is distributed using the parameters found for the freely expanding [O I]-emitting ejecta model. No additional dust component coupled to the Hα emitting region is required. The χ^2 value is minimized when there is a small overlap between the radii of the Hα shell and the ejecta dust shell, so as to induce some dust absorption on the red wing of the Hα line.

The Hα and [O I] emission line models require different V_{max}, R_{in}/R_{out}, and β values, indicating that the two emitting species are not colocated. The assumption of an Hα distribution that is expanding freely and coupled with the dust can create a model that fits the profile well, but leads to derived dust masses that are of a factor of ∼5 less than the dust masses derived from the [O I] modelling.

3.2.3 SN 1979C

SN 1979C was discovered on 1979 April 19 in M100 (Mattei et al. 1979). It was thought to be a Type II-L supernova from the fast decline

Table 4. Parameters used in the DAMOCLES models of the broad emission lines of SN 1957D, SN 1970G, SN 1980K, and SN 1993J for spherically symmetric smooth and clumped dust models. 'a' is the dust grain radius. The value of a derived at day 21 535 for SN 1957D has been fixed for all epochs. The 'Per cent Sil' column stands for the percentage of the dust species that is astronomical silicate, where the remainder is amorphous carbon dust. The optical depth is calculated from R_{in} to R_{out} at the central line wavelengths ([O III] = 5007 Å, [O I] = 6300 Å, Hα = 6563 Å).

| SN	Line	Epoch (d)	Clumped?	Per cent Sil	a (μm)	V_{max} (km s^{-1})	V_{min} (km s^{-1})	β_{gas}	R_{out} (10^{15} cm)	R_{in} (10^{15} cm)	M_{dust} (10^{-2} M$_\odot$)	τ	χ^2
1957D	[O III]	11 371	No	0	0.4	5800	870	2.5	1079	140.3	0.5	0.17	
1957D	[O III]	11 371	Yes	0	0.4	5800	870	2.7	1079	140.3	1.0	0.31	
1957D	[O III]	11 371	No	100	0.2	5800	870	2.5	1079	140.3	0.4	0.32	
1957D	[O III]	11 371	Yes	100	0.4	5800	870	2.5	1079	140.3	1.4	0.18	
1957D	[O III]	19 459	No	0	0.4	6800	1020	2.4	1265	164.5	1.5	0.16	0.89
1957D	[O III]	19 459	Yes	0	0.4	6800	1020	2.4	1265	164.5	2.5	0.41	0.76
1957D	[O III]	19 459	No	100	0.2	6800	1020	2.4	1265	164.5	0.8	0.11	0.84
1957D	[O III]	19 459	Yes	100	0.4	6800	1020	2.4	1265	164.5	3.5	0.14	0.83
1957D	[O III]	21 535	No	0	0.4	7500	962	2.5	1377	179.0	3.0	0.15	
1957D	[O III]	21 535	Yes	0	0.4	7500	962	2.5	1377	179.0	5.0	0.27	
1957D	[O III]	21 535	No	100	0.2	7500	962	2.5	1377	179.0	2.0	0.22	
1957D	[O III]	21 535	Yes	100	0.4	7500	962	2.5	1377	179.0	7.0	0.19	
1970G	Hα	16 713	No	AmC	0.20	6700	2546	−0.3	968.6	290.6	1.5	0.34	
1970G	Hα	16 713	Yes	AmC	0.25	6700	2546	−0.3	968.6	290.6	1.5	0.34	
1970G	Hα	16 713	No	Sil	0.20	6600	3960	−0.3	954.2	572.5	7.0	0.61	
1970G	Hα	16 713	Yes	Sil	0.20	6600	3960	−0.1	954.2	572.5	10.0	1.12	
1980K	Hα	13 169	No	0	3.50	5300	4505	1.5	593.1	504.0	40.0	0.53	
1980K	Hα	13 169	Yes	0	3.50	5300	4505	1.5	593.1	504.0	60.0	0.81	
1980K	Hα	13 169	No	100	0.10	5300	4505	1.5	593.1	504.0	20.0	0.92	
1980K	Hα	13 169	Yes	100	0.10	5300	4505	1.5	593.1	504.0	60.0	2.91	
1980K	[O I]	13 169	No	0	3.50	5300	3445	1.5	593.1	385.5	40.0	0.67	
1980K	[O I]	13 169	Yes	0	3.50	5300	3445	1.5	593.1	385.5	60.0	0.97	
1980K	[O I]	13 169	No	100	0.10	5300	3445	1.5	593.1	385.5	20.0	1.43	
1980K	[O I]	13 169	Yes	100	0.10	5300	3445	1.5	593.1	385.5	60.0	4.13	
1993J	[O III]	8417	No	0	0.20	5800	4408	5	421.8	320.6	1.3	0.86	
1993J	[O III]	8417	Yes	0	0.20	5800	4408	5	421.8	320.6	2.5	1.66	
1993J	[O III]	8417	No	100	0.04	5800	4408	5	421.8	320.6	25.0	0.82	
1993J	[O III]	8417	Yes	100	0.04	5800	4408	5	421.8	320.6	50.0	1.64	
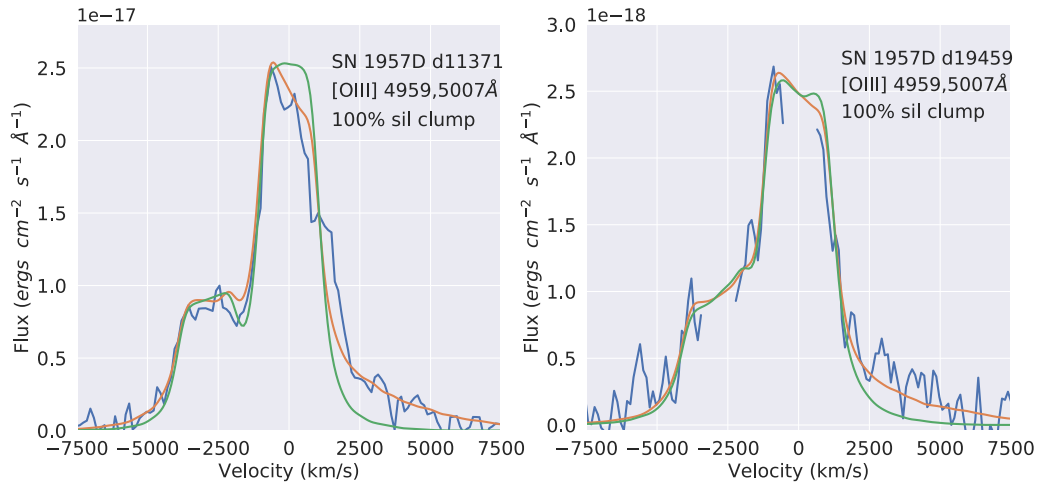
Figure 1. DAMOCLES models of the [O III] 4959, 5007 Å profiles of SN 1957D 11 371 and 19 459 d post-explosion. The green line is the dust-free model, the orange line is the dust-affected model, and the blue line is the observed spectral line. Clumped dust models with 100 per cent astronomical silicate are shown.
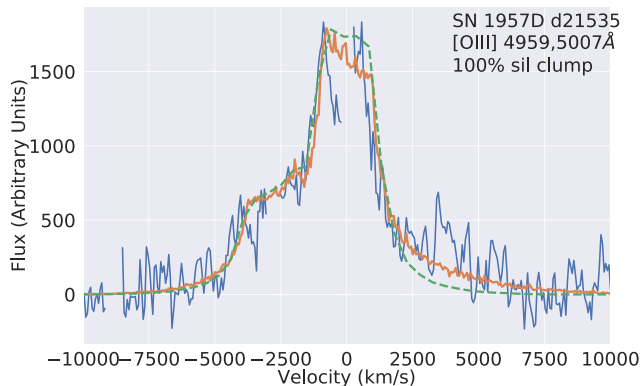

Figure 2. DAMOCLES model of the [O III] profiles of SN 1957D 21 535 d post-explosion. The green line is the dust-free model, the orange line is the dust-affected model, and the blue line is the observed spectral line. Clumped dust models with 100 per cent astronomical silicate are shown.

of its light curve and absence of a plateau (Panagia et al. 1980). The explosion was considered unusually bright when compared to other Type II-Ls, with a peak M_B of −20 mag (Young & Branch 1989).

Fig. 4 shows the evolution of the spectra through 5146, 10 575, 13 150, and 13 907 d. The spectra have been corrected for the redshift of the host galaxy of $z = 0.00525$ (Van Driel et al. 2016). At the earliest epoch, the oxygen doublets are double peaked, most noticeably the [O II] 7319, 7330 Å profile, with a weaker peak centred at 0 km s^{-1}. The central peak declines in brightness over 10 000 d until it is barely visible at 13 907 d. The Hα profiles at day 10 575 and beyond notably lack this central peak, and are far more symmetric than the forbidden oxygen emission lines. We interpreted the central peak to be an IWC, possibly formed by an ejecta–circumstellar media (CSM) interaction, while we term the broader underlying profile to be the broad component (BC), which represents the fast-expanding ejecta. We assumed a simple model set-up for the oxygen lines at days 5146 and 13 150 and for the [O III] doublet at day 13 907, in which the dust has formed in the ejecta, and is therefore coupled with the BC, and the separate component emitting the IWC is located where $R_{\mathrm{in,IWC}} \approx R_{\mathrm{out,BC}}$, and whose redshifted emission is affected by absorption by the ejecta dust. We found that no separate dust component colocated with the IWC was necessary, but note that the

shape of the IWC on day 5146 is unclear due to the lower resolution, while at later epochs the IWC is faint, so we cannot rule out this possibility.

Models of the [O I] 6300, 6363 Å and [O II] 7319, 7330 Å doublets at an epoch of 5146 d are shown in Fig. 5. We did not model the [O III] 4959, 5007 Å doublet at 5146 d as there were several poorly subtracted narrower nebular lines present that, given the low resolution, obscured the line profile shape. The dust was optically thick at this epoch. We found that for a dust clump of 100 per cent astronomical silicate $\tau = 4.4$ at a line wavelength of 7319 Å.

We modelled the [O I] 6300, 6363 Å, [O II] 7319, 7330 Å, and [O III] 4959, 5007 Å doublets at days 10 575 and 13 907 post-explosion. The best-fitting clumped silicate dust models are shown in Figs 6 and 7.

We modelled the Hα line profile at day 13 150, as it was slightly less blended with the [O I] profile at this epoch than at day 13 907, which can be seen in Fig. 8. We used a dust clumping mass fraction of 0.95 for all our clumped models at all epochs. A diagram showing the adopted distributions of the Hα and oxygen emitting regions for SN 1979C can be seen in Fig. A7.

The grain radius was originally constrained for a smooth AmC dust model from the scattering wing of the [O II] 7319, 7330 Å line profile at day 13 907, which had the best S/N of all the line profiles for any epoch. The albedo for this dust grain radius was 0.48. For a clumped amorphous carbon dust composition, as well as for a smooth and clumped silicate dust composition, we found dust grain radii that best matched this albedo. These grain sizes, along with the rest of the model parameters, are listed for all the modelled lines in Table 5. The grain radius derived at this epoch was fixed for the other epochs. The dust masses derived using 100 per cent silicate compositions are much higher than for the 100 per cent AmC models, leading us to favour dust models for SN 1979C that have a silicate proportion of 50 per cent or less. For consistency with the other CCSNe modelled in our sample, we use a 50:50 AmC to silicate dust composition with a single grain radius, for which in this case the best-fitting grain radius was 0.1 μm, to report our final preferred dust masses.

From a manual parameter space examination, the [O I], [O II], and [O III] lines at day 10 575 all required similarly large dust masses, where the [O I] and [O II] doublets could be well fitted with models of matching parameters. We note that the [O III] distribution differs from that of [O I] and [O II] in requiring a higher β value, which
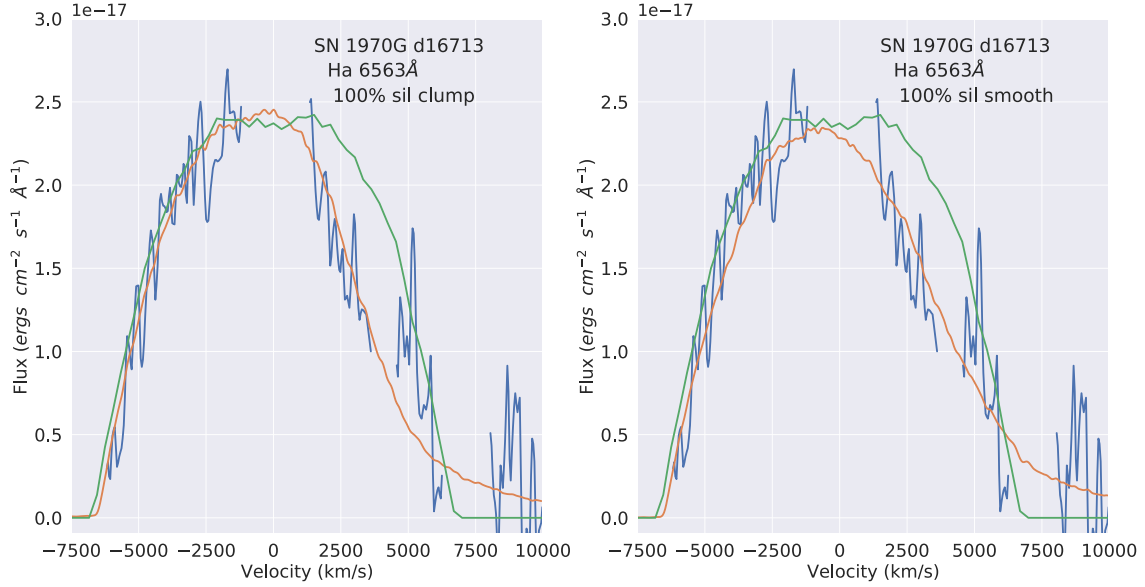
Figure 3. DAMOCLES models of the Hα profile of SN 1970G 16 713 d post-explosion. The green line is the dust-free model, the orange line is the dust-affected model, and the blue line is the observed spectral line. Clumped and smooth dust models of 100 per cent astronomical silicates are shown.
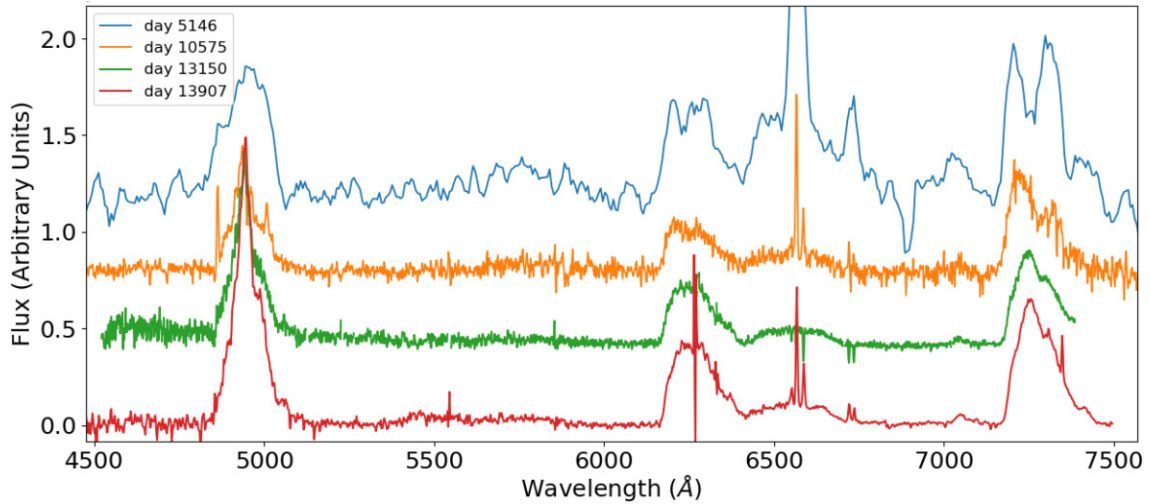

Figure 4. The evolution of the optical spectrum of SN 1979C. Information on the spectra is summarized in Tables 1 and 3.

implies the [O III] gas is more densely distributed than the other oxygen ion species. A higher β value requires more dust to provide the same amount of absorption as a model with a lower β, which has led to slightly higher dust masses derived from modelling the [O III] doublet in comparison to the other oxygen ion lines. These trends also apply to the spectral lines at day 13 907 post-explosion.

Using a Bayesian analysis, we evaluated the errors on the ejecta dust masses at days 10 575 and 13 907 that were derived from the [O II] doublet, where the resulting corner plots can be found in Figs A2 and A3. We removed the IWC component to the [O II] line at both epochs prior to modelling. The oxygen line profiles appear significantly redshifted between days 10 575 and 13 907, so quantifying the errors on the derived dust masses is particularly important. Simulations for both epochs were run with 100 per cent clumped AmC dust, where the median dust mass at both epochs agreed very well with our initial estimates for the 100 per cent AmC dust masses shown in Table 5. We therefore extrapolated the dust

mass uncertainties to our 50:50 AmC to silicate dust masses for a 0.1 μm single-size grain radius, leading to dust masses of $0.65^{+0.85}_{-0.43}$ and $0.30^{+0.13}_{-0.15} \, M_{\odot}$ at days 10 575 and 13 907. Whilst the median values would indicate dust destruction between the two epochs, the large error bars on the dust mass at day 10 575 mean we cannot definitely conclude that dust destruction is happening. However, this possibility makes SN 1979C a particularly interesting target for continuing observations. We also note that both Bayesian runs favoured grain radii of 0.03–0.63 μm for 100 per cent AmC grains, where the 1D probability distribution at day 13 907 peaked at the same grain radii found with the manual fitting process, namely ∼0.2 μm.

To model the Hα line at day 13 150, we decoupled the dust and gas distributions, where the dust distribution shared that of the [O II] and [O I] models for day 13 907, and the gas was located such that $R_{in,H\alpha} = R_{out,O}$. We found a good fit to the Hα line with this simple model, seen in Fig. 8. The χ^2 for the dusty models averaged 0.9, while it was 1.5 for the dust-free model.
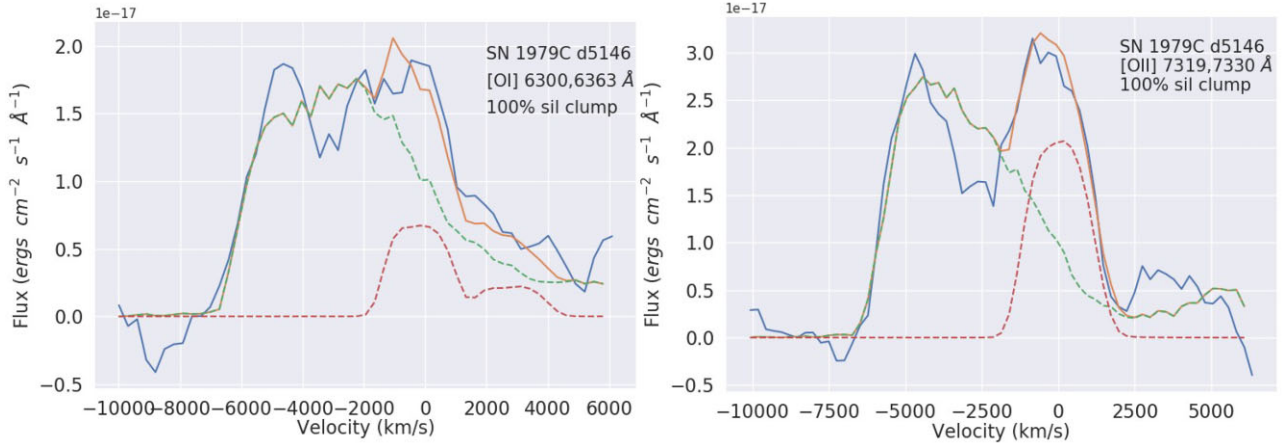
Figure 5. DAMOCLES models of the [O I] and [O II] profiles of SN 1979C. The blue lines are from the observed day 5146 spectrum presented by Fesen et al. (1999). The red and green dashed lines are the DAMOCLES models of the intermediate-width component (IWC) and broad component (BC), and the orange line is the sum of these two components. Clumped dust models consisting of 100 per cent astronomical silicates are shown.
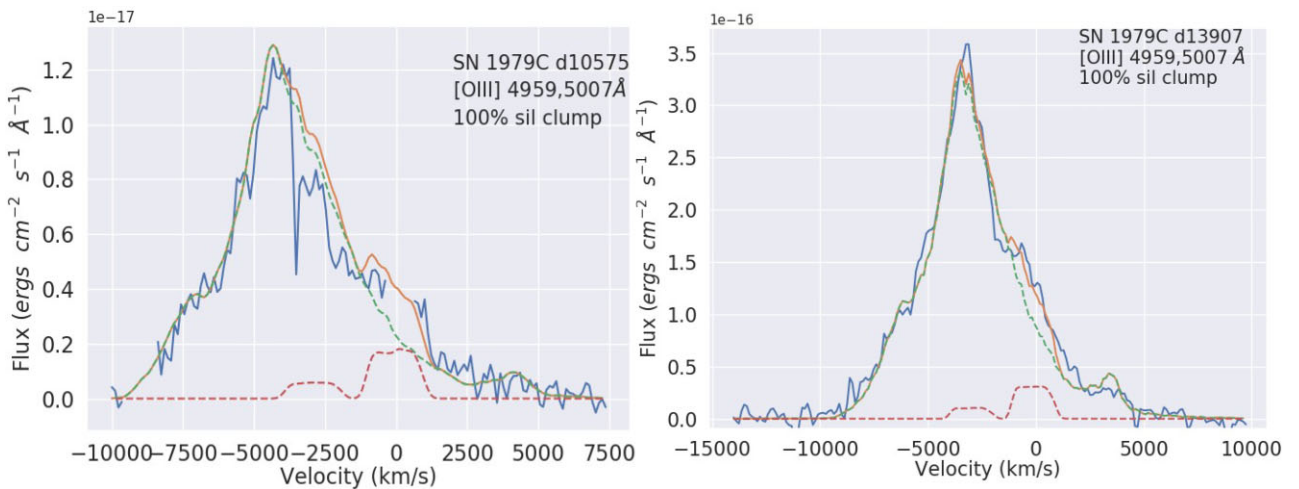

Figure 6. DAMOCLES models of the [O III] profile of SN 1979C at 10 575 and 13 907 d post-explosion. The red and green dashed lines are the DAMOCLES models of the IWC and BC, and the orange line is the sum of these two components. Clumped dust models of 100 per cent astronomical silicates are shown.

3.2.4 SN 1980K

SN 1980K was discovered by P. Wild on 1980 October 28 in NGC 6946, and reached a peak brightness of $V = 11.4$ mag a few days later (Buta 1982). Montes et al. (2000) estimated an explosion date for SN 1980K of 1980 October 2, which we use in this work. The detection of a broad Hα line in early spectra and a linearly decaying light curve after peak brightness resulted in its classification as a Type II-L SN (Barbon et al. 1979). The emergence of a near-IR flux excess in 1981 led Dwek (1983) to surmise that there could be dust in SN 1980K, but they could not resolve whether the dust was newly formed in the ejecta or pre-existing grains in a CSM. Milisavljevic et al. (2012) presented a spectrum of SN 1980K obtained 30 yr after explosion (on day 10 964) and postulated that there could be dust present in the ejecta based on the observed blueshifting of their Hα and [O I] line profiles. The profiles of the day 10 964 lines were modelled using DAMOCLES by Bevan et al. (2017, hereafter B17), who derived a dust mass of ∼0.2 M$_\odot$ for a dust composition that was deduced to be dominated by silicate grains, from the presence of extended red scattering wings.

We have summed the day 12 977 MMT spectrum of SN 1980K (Table 3) with our GMOS spectra taken at a mean epoch of 13 361 d after explosion (Table 1), correcting for the small recessional velocity of the host galaxy (40 km s^{-1}). The resulting 'day 13 169' spectrum of SN 1980K has a slightly higher S/N than the day 10 964 spectrum taken 6 yr earlier by Milisavljevic et al. (2012) and modelled by B17, but not a high enough S/N to conduct a Bayesian analysis. We have modelled the [O I] 6300, 6363 Å and Hα lines using the same species and grain radius values as B17. Our best-fitting clumped silicate dust models are shown in Fig. 9, with the parameters listed in Table 4. The model parameters for the [O I] line we found were similar to those of B17, although the density exponent of $\beta = 1.5$ required for our best-fitting models was lower than their day 10 964 best-fitting value of $\beta = 4.0$. The best-fitting dust mass required to attenuate the [O I] line profile, for a 100 per cent clumped silicate model with a grain radius of 0.1 μm, was $0.60^{+3.29}_{-0.57}$ M$_\odot$. It was possible to fit the Hα line profile with similar parameters as those used to model the [O I] line. Therefore, we ran a Bayesian analysis of the Hα and [O I] line simultaneously using a silicate dust grain species, which provided the dust mass uncertainty limits on the value referenced above. The
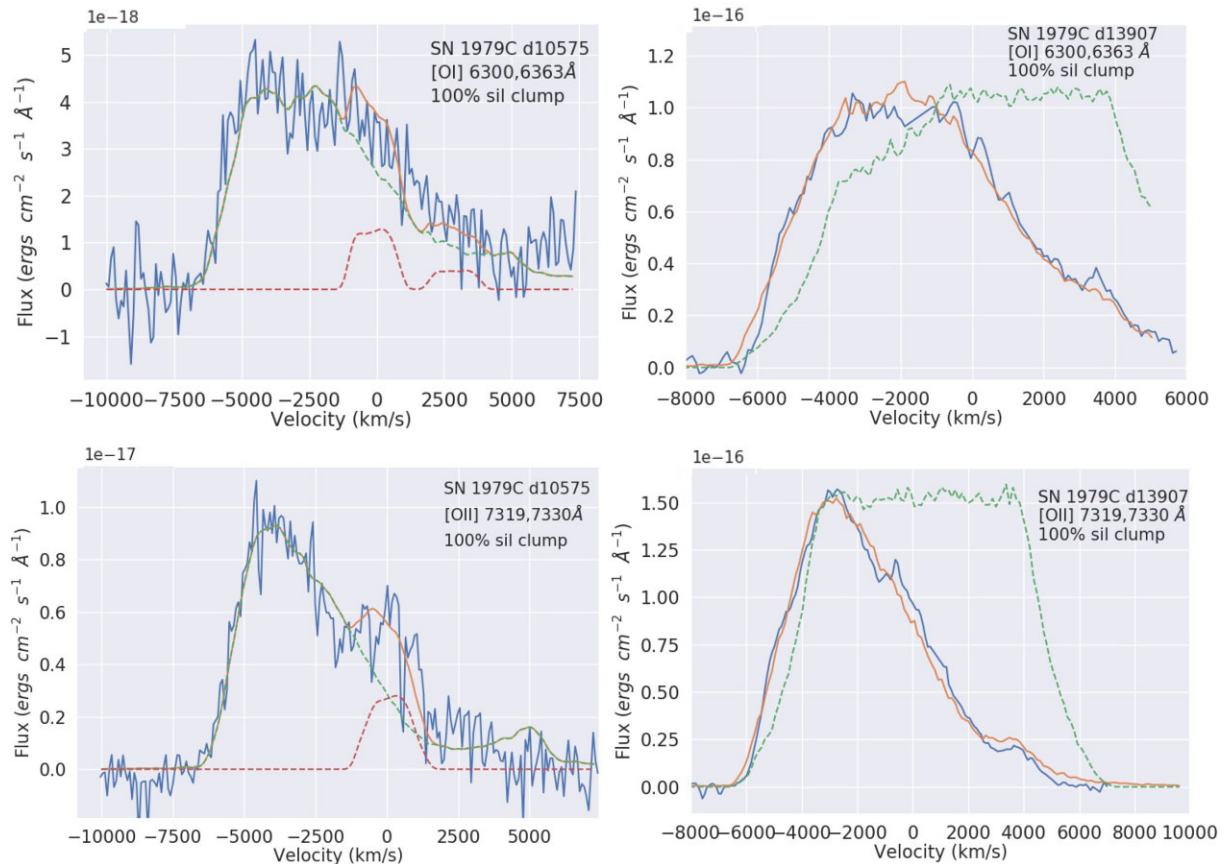
Figure 7. DAMOCLES models of the [O I] and [O II] doublets in SN 1979C at 10 575 and 13 907 d post-explosion. For day 10 575, the red and green dashed lines are the DAMOCLES models of the IWC and BC, and the orange line is the sum of these two components. For day 13 907, as no IWC is required the orange line is the BC. The green dashed line is the dust-free model. Clumped dust models of 100 per cent astronomical silicates are shown.
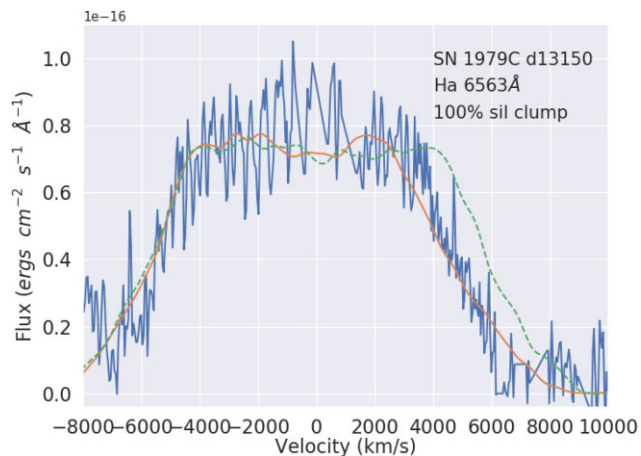

Figure 8. DAMOCLES model of the Hα profile of SN 1979C at 13 150 d post-explosion. The green dashed line is the dust-free model. The orange line represents the best-fitting dusty model, where the dust is assumed to consist of 100 per cent silicate dust clumps, located with the freely expanding [O II] ejecta at day 13 907, where the parameters for this dust distribution are given in Table 5.

day 10 964 dust mass of 0.3 M$_\odot$ derived by B17 using the same grain parameters is within our calculated uncertainties.

Setting the $R_{\rm in}$ value for the Hα-emitting gas to be equal to the $R_{\rm out}$ value of the [O I] distribution, as in the case of SN 1979C, could

not replicate the observed Hα line profile, as then the absorption induced by the dust that is coupled with the [O I]-emitting ejecta produced an overabsorption of the red wing of the Hα line. The adopted distributions of the Hα and oxygen-emitting regions in SN 1980K can be seen in Fig. A7.

3.2.5 SN 1993J

SN 1993J is located in the nearby M81 galaxy and was discovered on 1993 March 28 (Ripero et al. 1993). Baron et al. (1993) established an explosion date of 1993 March 27. The asymmetries in the broad oxygen lines in the late-time spectra led Fransson et al. (2005) and Milisavljevic et al. (2012) to speculate on the presence of dust in the SN, and modelling by B17 of the red–blue asymmetries in the latter's day 6101 spectrum using DAMOCLES yielded an ejecta silicate dust mass of $\sim$0.1 M$_\odot$. Zsíros, Nagy & Szalai (2022) modelled archival 3.6–24 μm *Spitzer* SEDs of SN 1993J, obtained between 3875 and 5359 d post-explosion, and found there could be either $\sim$5 $\times$ 10^{-3} M$_\odot$ of silicate dust or $\sim$1 $\times$ 10^{-3} M$_\odot$ of amorphous carbon dust, emitting at $T \sim$ 200 K, significantly less than the $\sim$0.1 M$_\odot$ found by B17, which we attribute to the insensitivity of the *Spitzer* measurements to colder dust emitting longwards of 24 μm.

For SN 1993J we modelled the [O III] 4959, 5007 Å doublet profile from an MMT spectrum taken 8417 d post-explosion (Table 3). This spectrum had a lower S/N than the day 6101 spectrum of Milisavljevic et al. (2012) that was modelled by B17, enabling only the [O III] doublet to be modelled by us. We corrected the spectrum

Table 5. Parameters used in the DAMOCLES models of SN 1979C at various epochs for smooth and clumped for 100 per cent AmC dust (AmC) or 100 per cent astronomical silicate dust (Sil) of radius a, for the broad component (BC) and intermediate-width component (IWC). a is derived from fitting the oxygen lines at day 13 907 and is fixed at the other epochs. The optical depth is calculated from R_{in} to R_{out} at the central line wavelength ([O I] = 6300 Å, [O II] = 7319 Å, [O III] = 5007 Å, Hα = 6563 Å).

| Epoch (d)	Line	Comp.	Clumped?	Species	a (μm)	V_{max} (km s^{-1})	V_{min} (km s^{-1})	β_{gas}	R_{out} (10^{15} cm)	R_{in} (10^{15} cm)	τ	M_{dust} (M$_\odot$)	χ^2
5146	[O III]	BC	Yes	AmC	0.20	6700	5360	4.5	302.0	241.0	22.0	0.15	3.43
5146	[O III]	BC	No	AmC	0.13	6700	5360	4.5	297.0	237.0	6.2	0.03	4.32
5146	[O III]	BC	Yes	Sil	0.06	6800	5440	4.5	297.0	237.0	10.6	2.40	3.38
5146	[O III]	BC	No	Sil	0.05	6800	5440	4.5	297.0	237.0	2.8	1.00	4.00
5146	[O I]	IWC				1800	1260	0.1	430.0	301.0			
5146	[O I]	BC	Yes	AmC	0.20	7000	5320	4.5	311.2	236.5	12.9	0.10	1.72
5146	[O I]	BC	No	AmC	0.13	7000	5320	4.5	311.2	236.5	4.1	0.02	2.33
5146	[O I]	BC	Yes	Sil	0.06	7000	5320	4.5	311.2	236.5	17.3	2.40	1.70
5146	[O I]	BC	No	Sil	0.05	7000	5320	4.5	311.2	236.5	3.8	0.70	2.15
5146	[O I]	IWC				1800	1260	0.1	430.0	301.0			
10575	[O III]	BC	Yes	AmC	0.15	6900	4485	6.0	630.4	409.8	16.2	0.35	1.96
10575	[O III]	BC	No	AmC	0.13	6900	4485	6.0	630.4	409.8	4.2	0.08	1.96
10575	[O III]	BC	Yes	Sil	0.04	6900	4485	6.0	630.4	409.8	16.5	12.0	1.94
10575	[O III]	BC	No	Sil	0.04	6900	4485	6.0	630.4	409.8	3.4	2.50	1.92
10575	[O III]	IWC				1300	910	0.1	1000	700.0			
10575	[O I]	BC	Yes	AmC	0.20	7000	4410	4.5	639.6	402.9	16.0	0.45	0.46
10575	[O I]	BC	No	AmC	0.13	6800	4080	4.5	621.3	372.8	5.4	0.09	0.47
10575	[O I]	BC	Yes	Sil	0.06	6600	4950	5.5	603.0	452.3	11.7	10.0	0.47
10575	[O I]	BC	No	Sil	0.05	6600	4950	5.5	603.0	452.3	7.0	3.00	0.48
10575	[O I]	IWC				1400	980	0.1	1000	700.0			
10575	[O I]	BC	Yes	AmC	0.20	6800	4760	4.0	621.3	434.9	6.9	0.45	
10575	[O I]	BC	No	AmC	0.13	6800	4760	4.0	621.3	434.9	2.9	0.06	
10575	[O I]	BC	Yes	Sil	0.06	6800	4964	5.5	621.3	453.6	19.2	10.0	
10575	[O I]	BC	No	Sil	0.05	6800	4964	5.5	621.3	453.6	2.7	2.00	
10575	[O I]	IWC				1400	980	0.1	1000	700.0			
13150	Hα	BC	Yes	AmC	0.20	8900	4005	1.5	1710	855.0	3.6	0.16	0.90
13150	Hα	BC	No	AmC	0.13	8900	4005	1.5	1710	855.0	3.8	0.08	0.87
13150	Hα	BC	Yes	Sil	0.06	8900	4005	1.5	1610	805.0	4.9	3.40	0.95
13150	Hα	BC	No	Sil	0.05	8900	4005	1.5	1610	805.0	1.8	2.45	0.88
13907	[O III]	BC	Yes	AmC	0.15	6700	3618	4.6	805.0	434.7	10.2	0.30	2.50
13907	[O III]	BC	No	AmC	0.13	6700	3618	4.6	805.0	434.7	3.1	0.08	2.90
13907	[O III]	BC	Yes	Sil	0.04	6700	3618	4.9	805.0	434.7	8.1	8.50	2.90
13907	[O III]	BC	No	Sil	0.04	6700	3618	4.9	805.0	434.7	2.6	2.70	3.08
13907	[O III]	IWC				1400	980	0.1	1190	833.0			
13907	[O I]	BC	Yes	AmC	0.20	6600	3696	2.2	793.0	444.1	3.0	0.16	
13907	[O I]	BC	No	AmC	0.13	6600	3696	2.2	793.0	444.1	1.9	0.08	
13907	[O I]	BC	Yes	Sil	0.06	6600	3696	2.2	793.0	444.1	3.6	4.40	
13907	[O I]	BC	No	Sil	0.05	6600	3696	2.2	793.0	444.1	1.6	2.45	
13907	[O I]	BC	Yes	AmC	0.20	6800	3808	2.2	817.1	457.6	3.7	0.16	0.37
13907	[O I]	BC	No	AmC	0.13	6800	3808	2.2	817.1	457.6	1.9	0.06	0.44
13907	[O I]	BC	Yes	Sil	0.06	6800	3808	2.2	817.1	457.6	5.7	4.40	0.43
13907	[O I]	BC	No	Sil	0.05	6800	3808	2.2	817.1	457.6	2.0	2.00	0.43
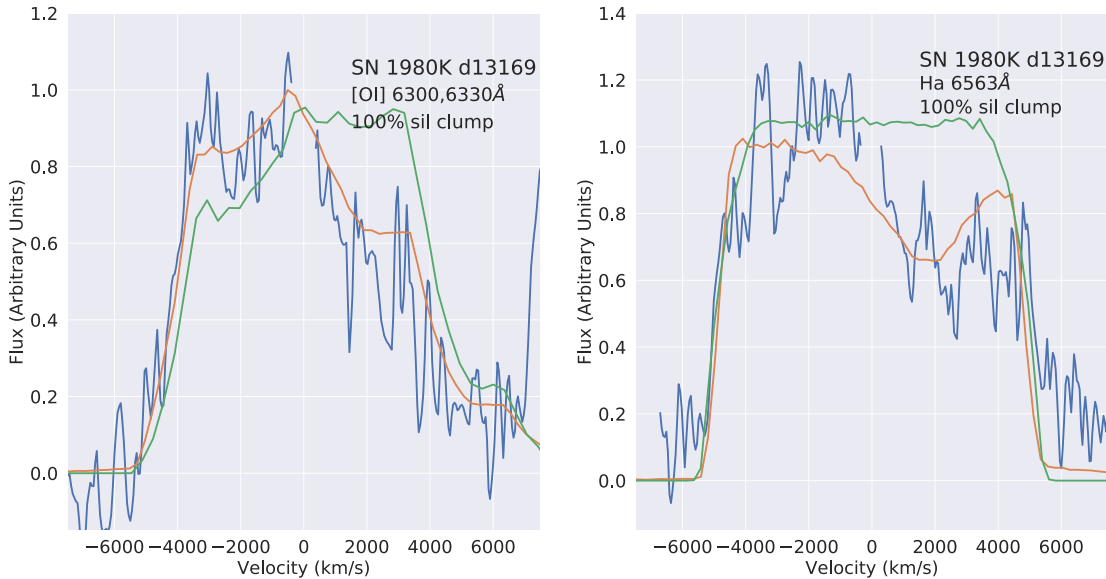
Figure 9. DAMOCLES models of the [O I] (left) and Hα (right) line profiles of SN 1980K at 13 169 d post-explosion. The green line is the dust-free DAMOCLES model, and the orange line is the dust-affected model. Clumped dust models consisting of 100 per cent astronomical silicate grains of 0.1 μm radius are shown.

for a recessional velocity for M81 of 140 km s^{-1} and used the same dust compositions as B17 in our models. Our best-fitting clumped silicate and AmC dust models are shown in Fig. 10, with parameters listed in Table 4.

For a 100 per cent clumped silicate dust distribution with a grain radius of 0.04 μm, as in B17, we found a best-fitting day 8417 dust mass of 0.50 M$_\odot$, from manually fitting the [O III] doublet, versus B17's day 6101 dust mass of 0.15 M$_\odot$. Like B17, we were not quite able to fit the red wing of the [O III] doublet, which could be due to the oversimplification of assuming that all of the emitting oxygen is distributed with a uniform density power law, as discussed by B17 in their section 4.3.

A Bayesian model of the [O III] doublet using a 100 per cent silicate dust composition returned a median dust mass of $0.21^{+0.67}_{-0.20}$ M$_\odot$. However, as the grain species or radius could not be determined for SN 1993J, we adopt the dust mass of $4.00^{+13.0}_{-3.8} \times 10^{-2}$ M$_\odot$ obtained for a 50:50 AmC to silicate dust mass ratio with a grain radius of 0.1 μm, where the error limits are scaled from the percentage errors of the Bayesian best-fitting 100 per cent silicate dust mass of 0.21 M$_\odot$ reported above.

3.2.6 SN 1986E

SN 1986E was discovered on 1986 April 13 in NGC 4302, by G. Candeo at the Asiago Observatory (Rosino 1986). An optical spectrum taken a month later of SN 1986E led Pennypacker et al. (1986) to infer that it was around 2 months past maximum brightness, and they classified SN 1986E as a Type II supernova from the presence of strong, broad Hα and [O I] 6300, 6363 Å lines with P Cygni profiles in the spectra. We adopt an explosion date of 1986 March 13 for our models. Cappellaro et al. (1990) fitted photometric measurements of SN 1986E, taken over the course of 2 yr, with the light curve of the typical Type II-L SN 1979C.

Our optical spectra were corrected for a recessional velocity of NGC 4302 of 1148 km s^{-1}. We have modelled the evolving optical emission Hα line profile of SN 1986E at ages of 3712, 10 619, and 11 723 d, and also modelled the [O I] 6300, 6363 Å doublet at

day 10 619, as the shape of the doublet at the other epochs is too unclear. Our best-fitting models can be found in Fig. 11. The day 3712 spectrum was taken from the Weizmann Interactive Supernova Data Repository (WISeREP) archive[1] and appears to be unpublished: it has a spectral resolution of 12 Å.

There is a strong contribution to both the Hα and [O I] 6300, 6363 Å line profiles from an IWC and a BC, where the brightness of the IWC relative to that of the BC increases between days 3712 and 10 619 post-explosion, and decreases between days 10 619 and 11 723. The IWC of SN 1986E is a much more prominent component to the profiles than for the emission lines of SN 2004et and SN 1979C at similar epochs, and it also varies much less in relative brightness over a longer period of time than for either SN 2004et or SN 1979C. The evolving spectra suggest there could be an interaction between the SN ejecta and an extended, smooth CSM. We assume the BC in both the Hα and [O I] profiles represents the freely expanding ejecta, whereas the IWC represents a collision region between CSM and the ejecta, where the outer radius of the IWC is a free parameter.

The spectrum at day 10 619 has the highest S/N and we consider the model parameters derived for this epoch the most reliable. As much of the BC shape is not visible due to the overlapping IWC and the presence of a scattering wing cannot be determined due to low S/N, we could not accurately constrain the grain species or grain radius of the dust inducing the red–blue asymmetry in the BC. Model parameters using conservative grain sizes for either a 100 per cent AmC or a 100 per cent silicate dust composition in the BC are listed in Table 6. We derived clumped dust masses that minimized the χ^2 values between the model and observed Hα BC profiles of SN 1986E for the three epochs for a 50:50 carbon to silicate composition with a single grain radius of 0.1 μm. These dust masses were $0.03_{-0.024}$ M$_\odot$ at day 3712 and $\sim 0.07_{-0.065}$ M$_\odot$ at 10 619 and 11 723 d, where the lower limits were determined by a 35 per cent variation to the best-fitting χ^2 value. We could not determine accurate upper limits for these epochs due to optically thick conditions for dust masses higher than the best-fitting value but the above values indicate some
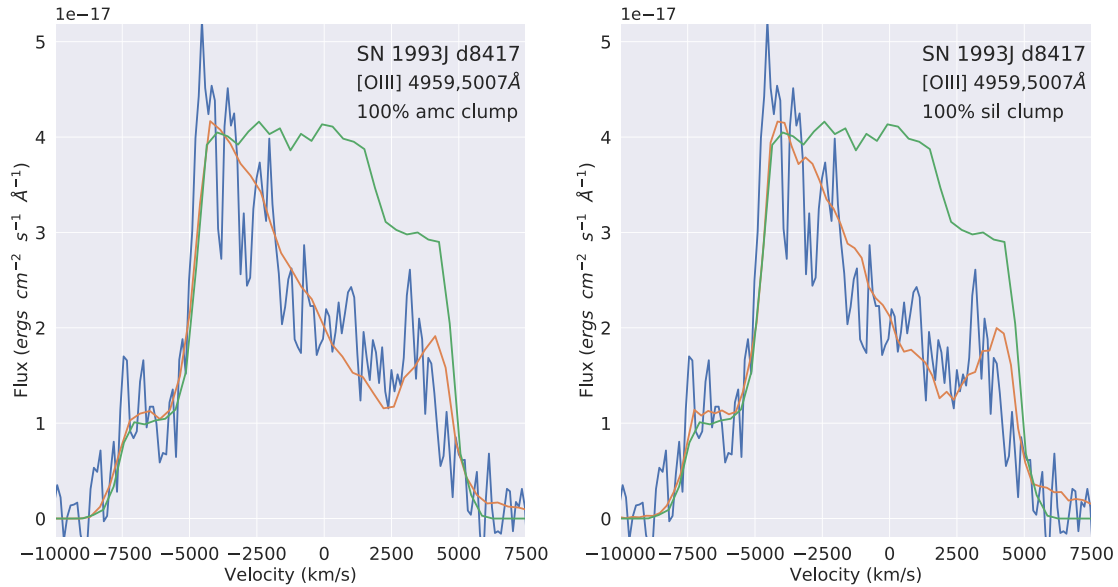
---

[1] https://wiserep.weizmann.ac.il/

Figure 10. DAMOCLES models of the [O III] 4959, 5007 Å doublet profile of SN 1993J at 8417 d post-explosion. The green line is the dust-free DAMOCLES model, and the orange line is the dust-affected model. Clumped dust models for 100 per cent AmC (left) and 100 per cent astronomical silicates (right) are shown.
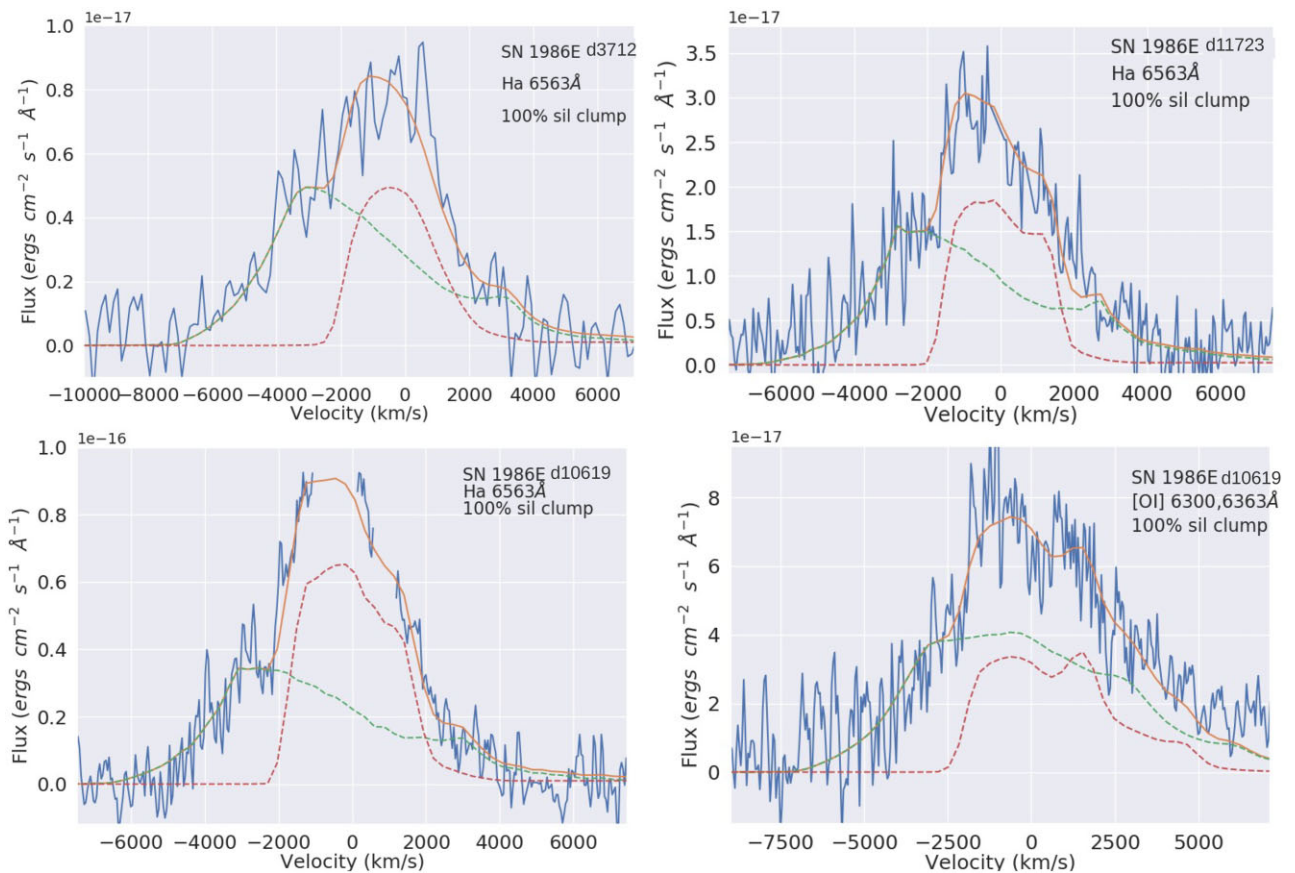

Figure 11. DAMOCLES models of the Hα line profiles of SN 1986E at 3712, 10 619, and 11 723 d post-explosion, and of the [O I] 6300, 6363 Å doublet 10 619 d post-explosion. The green line is the dust-affected BC, the red line is the dust-affected IWC, and the orange line is the sum of the green and red lines. Clumped dust models consisting of 100 per cent astronomical silicates are shown.

Table 6. Parameters used in the DAMOCLES models for SN 1986E's and SN 2004et's broad component (BC) and intermediate-width component (IWC) of Hα and SN 1986E's [O I] 6300, 6363 Å emission lines for spherically symmetric smooth and clumped dust models. 'Sil' stands for 100 per cent astronomical silicate dust, while 'AmC' is 100 per cent AmC dust, each of grain radius a. The optical depth is calculated from R_{in} to R_{out} at the central line wavelengths ([O I] = 6300 Å, Hα = 6563 Å). All SN 2004et models used 100 per cent silicate dust, which was determined from fits to the mid-IR SEDs by Kotak et al. (2009) and Fabbri et al. (2011). The optical depth was calculated from R_{in} to R_{out} at the wavelength of Hα. The grain radius is fixed to 0.2 μm for the BC at both epochs from fits to the IWC at day 646.

| SN	Epoch (d)	Line	Clumped?	Comp.	Species	a (μm)	V_{max} (km s^{-1})	V_{min} (km s^{-1})	β_{gas}	R_{out} (10^{15} cm)	R_{in} (10^{15} cm)	M_{dust} (10^{-2} M$_\odot$)	τ	χ^2
1986E	3712	Hα	Yes	BC	AmC	0.20	7100	3337	2.3	225.8	106.1	1.7	6.55	1.14
1986E	3712	Hα	No	BC	AmC	0.20	7100	3337	3.0	225.8	106.1	0.7	2.34	1.04
1986E	3712	Hα	Yes	BC	Sil	0.55	7100	3337	2.3	225.8	106.1	25	12.2	1.11
1986E	3712	Hα	No	BC	Sil	0.55	7100	3337	3.0	225.8	106.1	7.1	3	1.06
1986E	3712	Hα	Yes	IWC	Sil	0.20	2300	575	−0.5	948.0	237.0	5	1.75	
1986E	10619	[O I]	Yes	BC	AmC	0.20	6600	3102	3.0	603.8	241.5	3.5	1.39	1.02
1986E	10619	[O I]	No	BC	AmC	0.20	6600	3102	3.0	603.8	241.5	2.5	0.97	0.99
1986E	10619	[O I]	Yes	BC	Sil	0.55	6600	3102	3.0	603.8	241.5	25	1.33	1.05
1986E	10619	[O I]	No	BC	Sil	0.55	6600	3102	3.0	603.8	241.5	15	0.78	1.04
1986E	10619	[O I]	Yes	IWC	Sil	0.20	2300	1725	2.0	1000	650.0	5	0.34	
1986E	10619	Hα	Yes	BC	AmC	0.20	6600	3102	3.0	603.8	283.8	2.5	1.13	1.07
1986E	10619	Hα	No	BC	AmC	0.20	6600	3102	3.0	603.8	283.8	2	0.86	1.03
1986E	10619	Hα	Yes	BC	Sil	0.55	6600	3102	3.3	603.8	283.8	25	1.51	1.16
1986E	10619	Hα	No	BC	Sil	0.55	6600	3102	3.3	603.8	283.8	15	0.86	1.09
1986E	10619	Hα	Yes	IWC	Sil	0.20	2100	1365	1.0	1000.0	650.0	5	0.35	
1986E	11723	Hα	Yes	BC	AmC	0.20	6600	2640	3.0	668.3	314.1	3.5	1.39	0.92
1986E	11723	Hα	No	BC	AmC	0.20	6600	2640	3.0	668.3	314.1	2.5	1.04	0.93
1986E	11723	Hα	Yes	BC	Sil	0.55	6600	2640	3.0	668.3	314.1	35	1.77	0.91
1986E	11723	Hα	No	BC	Sil	0.55	6600	2640	3.0	668.3	314.1	25	1.34	0.93
1986E	11723	Hα	Yes	IWC	Sil	0.20	1900	1330	2.0	1100.0	770.0	5	0.23	
2004et	646	Hα	No	BC	Sil	0.2	9500	7410	1.7	53.02	39.24	0.03	0.5	
2004et	646	Hα	No	IWC	Sil	0.2	3000	450	1.6	170.0	51.00	0.12	0.39	
2004et	646	Hα	Yes	BC	Sil	0.2	9500	7410	1.7	53.02	39.24	0.05	0.57	
2004et	646	Hα	Yes	IWC	Sil	0.2	3000	450	1.6	170.0	51.00	0.2	0.73	
2004et	3849	Hα	No	BC	Sil	0.2	6000	5400	2	200.5	180.5	0.6	0.81	1.22
2004et	3849	Hα	Yes	BC	Sil	0.2	6000	5400	2	200.5	180.5	1.0	1.31	1.25
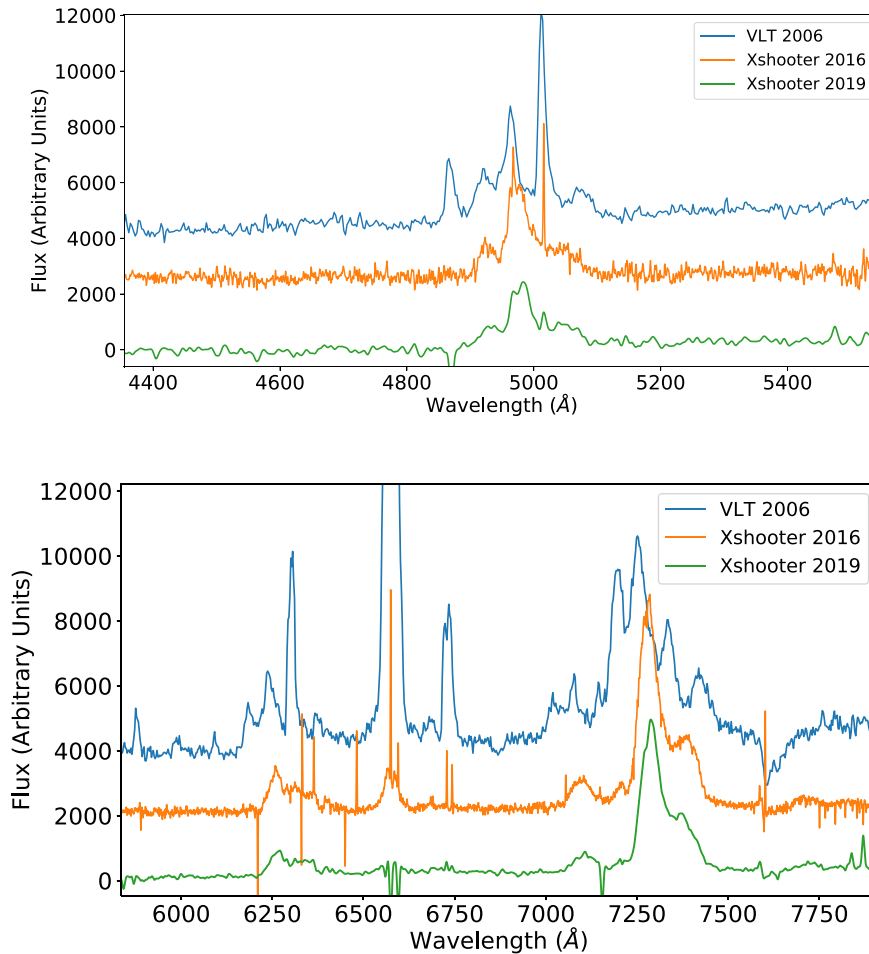
Figure 12. The evolution of the optical spectrum of SN 1996cr between 2006 and 2019. Information on the spectra is summarized in Tables 2 and 3.

dust mass growth in the ejecta of SN 1986E between days 3712 and 11 723.

It is difficult to independently determine a dust mass from the BC of the [O I] doublet profile at day 10 619 due to low S/N. However, we find we can fit the [O I] BC and IWC components with the same dust mass as that used for the Hα model, implying that the oxygen- and hydrogen-emitting gas could be colocated in SN 1986E, differing from the cases of SN 1980K, SN 1979C, and SN 1970G.

We tried a model for the Hα line profile at all three epochs where the dust was coupled to the freely expanding ejecta represented by the BC, and the IWC outer radius was set so that $R_{in,IWC} = R_{out,BC}$, as in the case for our models for SN 2004et at day 646. However, this set-up led to overabsorption of the red wing of the IWC by the dust in the BC. Therefore, the inner radius of the IWC needs to be slightly larger than the outer radius of the BC. A diagram of the distributions adopted for the SN 1986E Hα and oxygen-line emitting regions can be found in Fig. A7. The IWC showed a red scattering wing, most noticeably in the Hα profile at day 10 619 that could be best fit using a mass of $0.05^{+0.13}_{-0.047}$ M$_\odot$ for 0.2 μm silicate dust grains coupled to the IWC gas. As this dust would be located outside the BC-emitting shell, it would not induce a red–blue asymmetry in the BC.

3.2.7 SN 1996cr

SN 1996cr in the Circinus galaxy was first identified as an ultraluminous X-ray source by Bauer et al. (2001). VLT optical spectra of the

source taken by Bauer et al. (2008) revealed broad oxygen emission lines, and strong narrow Hα emission that allowed them to classify the source as an SNR created by a Type IIn supernova explosion. Multiwavelength archival observations helped them constrain the explosion date to between 1995 February 28 and 1996 March 16. We have adopted the latter date in order to calculate the post-explosion ages corresponding to our X-Shooter spectra of SN 1996cr.

The evolution of the optical spectrum of SN 1996cr from 2006 to 2019 is shown in Fig. 12. The oxygen doublets display red–blue asymmetries at every epoch. The 2006 VLT FOcal Reducer and low dispersion Spectrograph 1 (FORS 1) spectrum was first presented by Bauer et al. (2008). The oxygen doublets at this epoch have multiple peaks, indicative of ejecta interactions with a complex, likely asymmetric CSM. 10 yr later, some of the peaks had disappeared from both the blueshifted and redshifted parts of the oxygen doublets, and the strength of the Hα line has decreased substantially between 2006 and 2016, disappearing almost entirely by 2019. We assume that the spectrum of SN 1996cr in 2006 is dominated by the complicated ejecta–CSM interactions, whereas by 2016 the spectrum is dominated by ejecta emission, hence making it an ideal epoch to model with DAMOCLES.

We merged our days 7360, 7362, and 7389 X-Shooter spectra to form a 'day 7370' spectrum. Similarly, we merged our days 8446 and 8474 X-Shooter spectra to form a 'day 8460' spectrum. Our best-fitting DAMOCLES models to the [O I] 6300, 6363 Å, [O II] 7319, 7330 Å, [O III] 4959, 5007 Å, and [S III] 9069 Å lines at 7370 d are
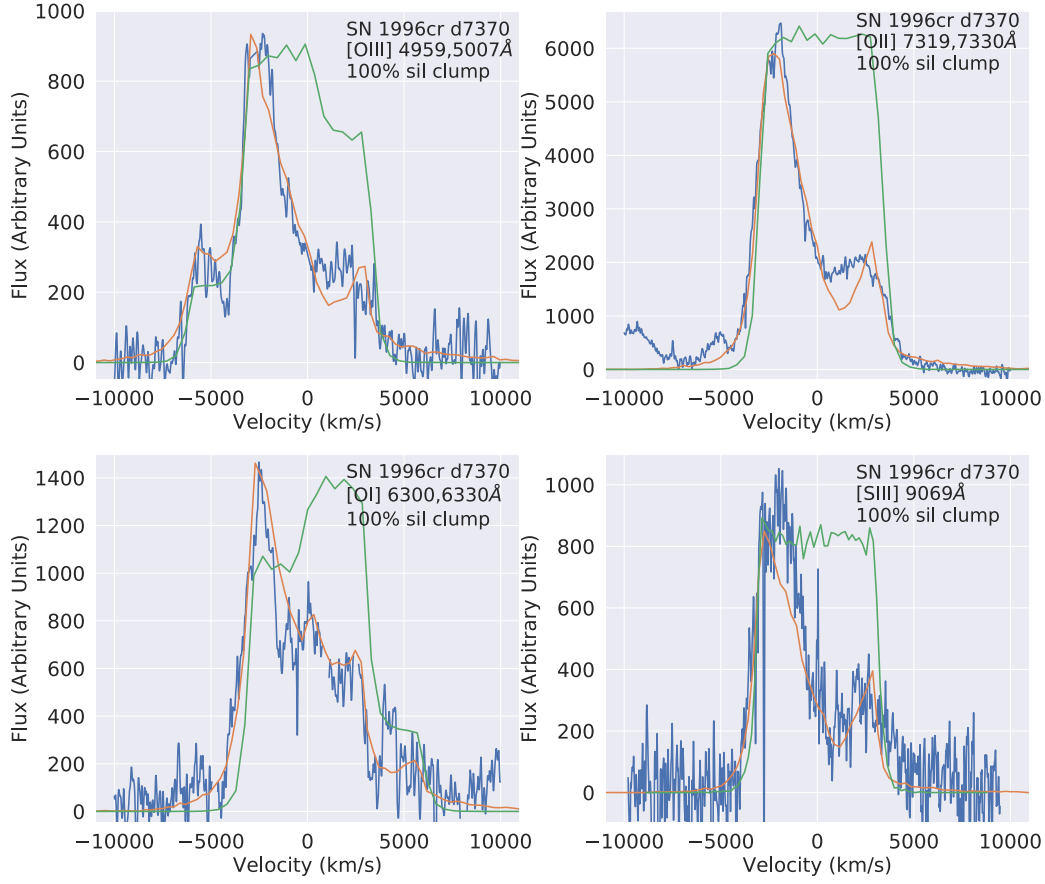
Figure 13. DAMOCLES models for the [O I], [O II], [O III], and [S III] X-shooter line profiles of SN 1996cr, 7370 d post-explosion. The green lines are the dust-free DAMOCLES models, and the orange lines are the dust-affected model. Clumped dust models of 100 per cent astronomical silicates are shown.
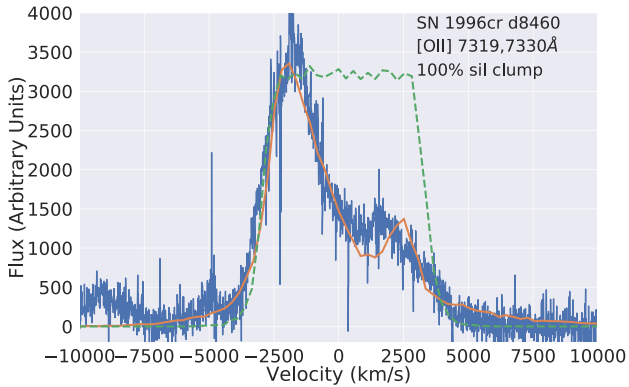

Figure 14. DAMOCLES models of the [O II] X-Shooter line profile of SN 1996cr 8460 d post-explosion. The green line is the dust-free DAMOCLES model, and the orange line is the dust-affected model.

shown in Fig. 13, and for the [O II] doublet 8460 d after explosion in Fig. 14. A recessional velocity of 510 km s^{-1} was adopted for the Circinus galaxy. Model parameters for both epochs are listed in Table 8. We were able to fit all the lines at day 7370 with similar values for V_{max}, β, and R_{in}/R_{out}, implying a mixing of ionization states in the remnant. Since dust absorption has a grain radius to wavelength dependence, we were able to find a single dust grain radius that required a matching dust mass that fit all the doublets simultaneously.

However, due to the lack of a red scattering wing, which if present could have ruled out high AmC dust proportions, we were not able to constrain the dust species. Therefore, we present model fits for smooth and clumped 100 per cent AmC and 100 per cent silicate dust, where in both cases we were able to constrain the dust grain radius for a clumped distribution to 0.12 and 0.05 μm. Because of the strength of the oxygen lines from the ejecta of SN 1996cr, a high proportion of silicates, from 50 per cent to 100 per cent, seems likely.

To try and rigorously constrain the error limits on the grain radius and dust mass, we ran a Bayesian simulation fitting the day 7370 [O III] and [O II] lines simultaneously using 100 per cent silicate dust. The distributions of the [O III]- and [O II]-emitting ions were assumed to be colocated, and coupled to the dust. The resulting corner plot can be seen in Fig. A4. Small silicate grains (<0.1 μm) are seen to be marginally preferable over larger ones. The median grain radius is 0.07 μm, very close to our initial estimate of 0.05 μm. The silicate dust mass probability distribution is strongly peaked at $0.47^{+0.63}_{-0.37}$ M$_\odot$, and the error limits are well defined. For a 50:50 ratio of carbon to silicate dust with a single grain radius of 0.11 μm, we obtain a dust mass of $0.10^{+0.13}_{-0.088}$ M$_\odot$. The quoted uncertainties on this value are derived from the Bayesian errors, which are taken as percentage errors on the median value and then used for the dust mass derived for the 50:50 carbon to silicate dust mix in order to obtain absolute uncertainties.

We only modelled the [O II] 7319, 7330 Å doublet in the day 8460 spectrum, as all the other lines had a low S/N. For a 50:50 ratio of AmC to silicate dust, using a single grain radius of 0.11 μm, $0.15^{+0.30}_{-0.14}$
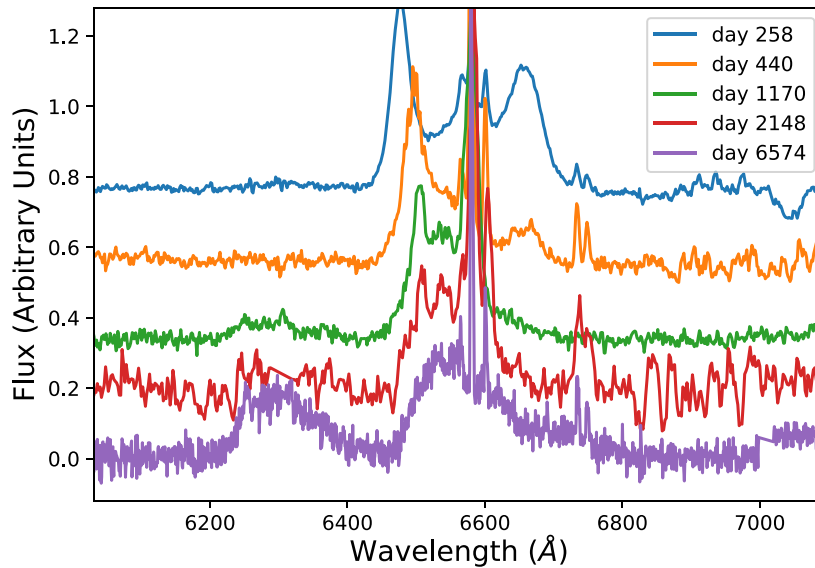
Figure 15. The evolution of the red region of the optical spectrum of SN 1998S between days 258 and 6574. Information on the sources of the spectra is summarized in Table 3.

$M_\odot$ of dust was required to fit the profile, where error limits were determined by a Bayesian analysis. The formal uncertainties on the dust masses are too high to infer anything about the evolution of the dust mass of SN 1996cr between 2016 and 2019.

3.2.8 SN 1998S

SN 1998S was a Type IIn object discovered in NGC 3877 on 1998 March 2 (Li et al. 1998). Its optical spectrum has changed extensively over the first 6000 d post-explosion. The spectrum was dominated by a CSM interaction at very early times. After 100 d the fairly symmetric line profiles changed drastically, and the Hα and He I 10 830 Å lines showed a highly asymmetrical triple-peaked structure (Gerardy et al. 2000). Fransson et al. (2005) attributed the multipeaked Hα line profile to a geometrically thin cool dense shell (CDS) behind the reverse shock, at large optical depths. Between days 258 and 440 (see Fig. 15) this multipeaked structure can be seen to exhibit a pronounced red–blue asymmetry that could be attributable to newly formed dust.

Mauerhan & Smith (2012) noted that after 10 yr the optical spectrum had become more dominated by ejecta emission, with the oxygen forbidden lines brightening relative to Hα (Fig. 15), although the high Hα luminosity indicated that SN 1998S was still interacting with dense circumstellar material.

There is potential evidence for dust formation in SN 1998S. Near-infrared (NIR) photometry and spectra between days 305 and 1242 (Gerardy et al. 2000; Pozzo et al. 2004) showed CO emission and a significant IR excess in the SED, although it was unclear how much this could be due to IR echoes reflecting off pre-existing dust clouds in the outer CSM (Sugerman et al. 2012). However, Mauerhan & Smith (2012) also noted blueshifted peaks to the Hα and oxygen line profiles and the disappearance of a redshifted peak in the Hα spectral line between days 1093 and 2900, which could indicate dust formation. It is unclear as to what quantities of dust were being formed in the ejecta or in a CDS around SN 1998S.

We model the Hα line from archival spectra at days 1170, 2148, and 6574 post-explosion; [O I] 6300, 6363 Å is bright enough at day

6574 to model as well. The sources of these published archival data are listed in Table 3. The spectra were corrected for a recessional velocity of NGC 3877 of 847 km s^{-1} (Fassia et al. 2000). The days 1170 and 2148 Hα lines show a sharp blueshifted emission spike around -4000 km s^{-1}, in the same location as that seen on day 440. We do not try to fit this feature in our models, as it is likely a feature leftover from the CSM–ejecta collision. The spectra at these epochs have fairly low resolution, so much of the profile is also taken up by narrow Hα emission features. We try and fit our ejecta models to the underlying shape similar to that seen at day 6574 in the more ejecta-dominated era, where the narrower peaks have disappeared.

At day 6574 the Hα, and to a lesser extent the [O I] profile, exhibited a red scattering wing, and we found that a 100 per cent silicate dust model improved the χ^2 value by a factor of 1.5 compared to the best-fitting 100 per cent AmC dust model. Hence we only show models consisting of a 100 per cent silicate dust distribution for all epochs in Fig. 16, with parameters listed in Table 8. We note, however, that it is possible for the earlier epochs to be tracing dust in a CDS region. We cannot determine the degree of similarity of the underlying Hα profile between earlier and later epochs due to the earlier line profiles being affected by narrow components between -2000 and 1000 km s^{-1}, but it is clear that a red scattering wing is much more evident at day 6574 than at days 1170 and 2148. Because of S/N limitations, for the days 1170 and 2148 line profiles the χ^2 value is the same for a 100 per cent carbon or 100 per cent silicate dust species.

We cannot determine whether SN 1998S's dust mass grew between days 1170 and 2148, as the dust required to attenuate the line profiles is optically thick at both epochs (see τ values in Table 8), and the line profiles have significant 'gaps' as discussed above. Because of this, our clumped models use a clump mass fraction of 0.85, with the rest of the dust being smoothly distributed. The optical depth of a single dust clump at day 1170 was calculated to be 28. We find a dust mass of roughly $2.5^{+4.10}_{-1.60} \times 10^{-2}$ M$_\odot$ at day 1170 and $4.0^{+6.00}_{-3.30} \times 10^{-2}$ M$_\odot$ at day 2148, with uncertainties at day 2148 given by a 35 per cent variation about the best-fitting χ^2 value, and those at day 1170 taken from the 1D posterior distribution of the dust mass found from a Bayesian model of the Hα line for a 100 per cent silicate dust species.
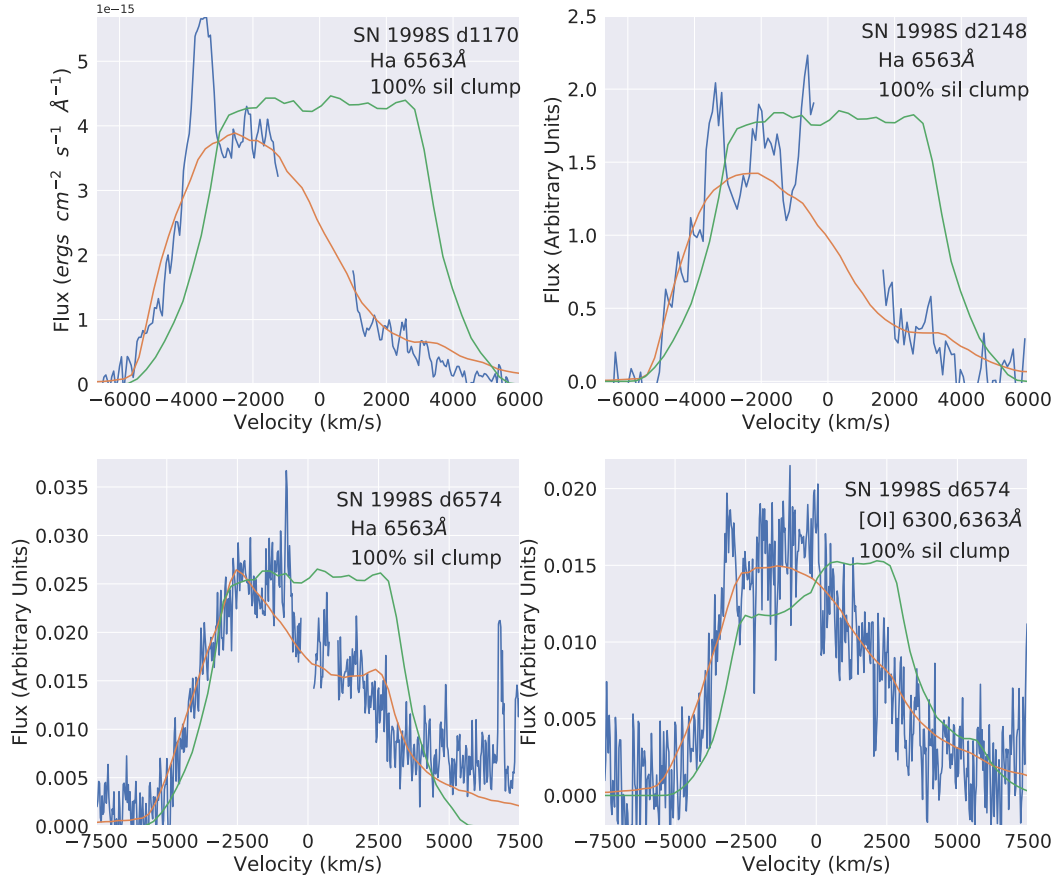
Figure 16. The orange lines represent the best-fitting clumped silicate dust-affected models for the Hα profiles of SN 1998S at three epochs and the [O II] 6300, 6363 Å lines at day 6574. Parameters of the best-fitting models can be found in Table 8. The dust-free model profiles are shown by the green lines.

At day 6574 we found that the Hα and [O I] lines could be well fitted with matching parameters, implying a colocation of the emitting species. We found that a grain radius of 0.08 μm for clumped silicate dust fitted both profiles best, and this grain radius and dust species was fixed for the other two epochs. It was close to the median grain radius of 0.20 μm found from a Bayesian analysis run with 100 per cent silicate dust for Hα and [O I] simultaneously. We can fit both lines with a clumped silicate dust mass of around $0.15^{+0.54}_{-0.14}$ M$_\odot$, with the uncertainties also taken from the Bayesian model referenced previously. This represents a significant increase in dust mass from the earlier epochs (a factor of 10).

3.2.9 SN 2004et

SN 2004et was a Type II-P supernova discovered on 2004 September 22 (Zwitter, Munari & Moretti 2004) in NGC 6946, the same galaxy that hosts SN 1980K. We adopt the discovery date as the explosion date. The optical spectrum was monitored from day 8 to 451 by Sahu et al. (2006), who noted that the emission peaks became blueshifted at around day 300, suggesting early dust formation.

Kotak et al. (2009) and Fabbri et al. (2011) continued to monitor the late-time optical spectra, where the Hα line became box-like around 2 yr post-explosion, perhaps indicative of an ejecta collision with a CSM, forming a CDS. Kotak et al. (2009) presented *Spitzer* observations between days 64 and 1406, where they inferred from modelling the SED that ∼10^{-4} M$_\odot$ of newly formed radioactively heated silicate dust was present in the ejecta. Fabbri et al. (2011) also

modelled the optical and mid-IR SED of SN 2004et, and found dust masses, made from 80 per cent silicate and 20 per cent AmC, that increased from ∼10^{-4} M$_\odot$ at day 300 to ∼10^{-3} M$_\odot$ at day 690.

We have modelled the Hα line profile of SN 2004et at days 646 and 3686 post-explosion (information on the spectra can be found in Tables 1 and 3). The spectra were corrected for a recessional velocity of NGC 6946 of 40 km s^{-1}. As both the work of Kotak et al. (2009) and Fabbri et al. (2011) found that a high proportion of silicates was required to fit the IR SED of SN 2004et, we only use 100 per cent silicate dust grains for our DAMOCLES models. From a visual inspection, the Hα line appears very different between the two epochs. The spectrum at day 646 also has a clear IWC not present at day 3686, possibly due to a CDS formed by ejecta–CSM interaction, or else due to flash-ionized CSM gas, as well as a BC representing the fast-expanding ejecta.

We assumed a simple model set-up where the ejecta emit the BC, and a separate component emits the IWC, where $R_{in,IWC} = R_{out,BC}$. The dust required for a good fit to the day 646 Hα BC, around 5×10^{-4} M$_\odot$, barely introduced an asymmetry in the IWC profile and we found that a separate dust mass component of around ∼2×10^{-3} M$_\odot$ was required to fit the IWC. Parameters for our models can be found in Table 6, with the line profile fits shown in Fig. 17.

Because of the presence of a scattering wing in the day 646 IWC, we were able to constrain the silicate grain radius to around 0.2 μm. From a Bayesian analysis of the BC (Fig. A5), we were able to quantify the uncertainties on the dust mass that had formed in the
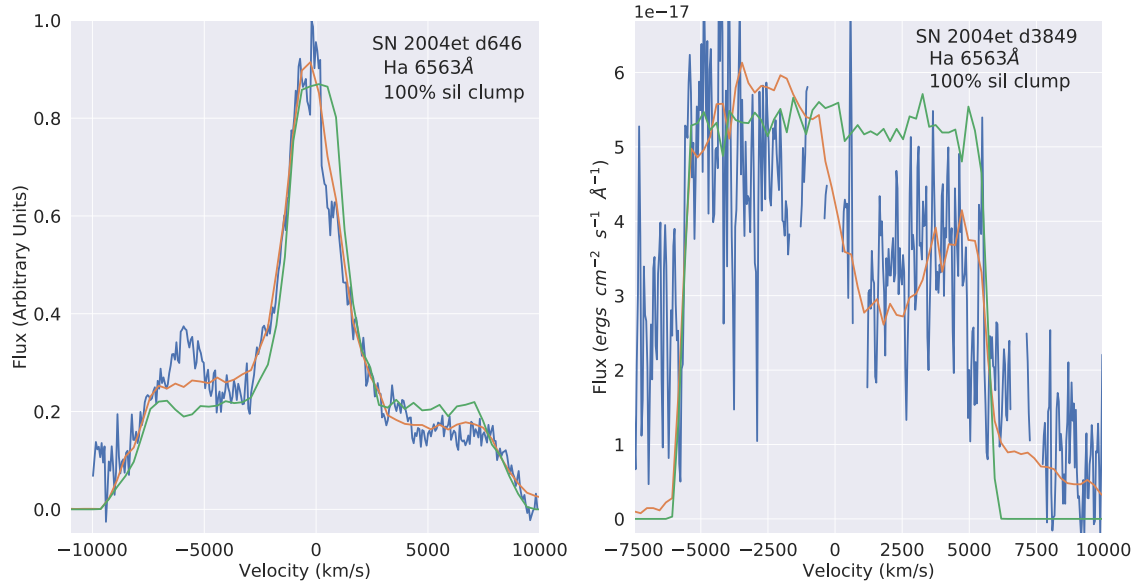
Figure 17. DAMOCLES models of the Hα line profiles of SN 2004et at 646 and 3849 d post-explosion. The green line is the dust-free DAMOCLES model, and the orange line is the dust-affected model. For day 646, the orange line consists of a BC and IWC summed together. Clumped dust models for 100 per cent astronomical silicates and 100 per cent AmC are shown.

ejecta, the lower and upper limits being 4×10^{-5} and 2.9×10^{-3} M$_\odot$, but we were not able to constrain the grain radius due to uncertainties in the continuum level. We have therefore adopted the same grain radius for the BC dust component as was required to fit the IWC. The dust mass derived for this grain radius functions roughly as a lower limit, as smaller or larger silicate grains require more dust to produce the same optical depth.

By day 3849, the Hα line emission from the IWC had faded, and the Hα emission is dominated by the ejecta. The S/N in this spectrum is low (Fig. 17), but there does appear to be a red scattering wing in the profile, which limits the silicate dust grains to >0.1 μm in radius, and rules out larger grain radii >0.5 μm. A grain radius of 0.2 μm and a dust mass of around 0.01 M$_\odot$ gave a χ^2 value of 1.2 when comparing the observed spectra and the model, with a lower limit of 2×10^{-4} M$_\odot$ and an upper limit of 0.9 M$_\odot$ taken from a varying best-fitting χ^2 of 35 per cent when all other parameters were fixed. This indicates a likely growth by a factor of 20 of the dust mass in the ejecta of SN 2004et between days 646 and 3849.

3.2.10 SN 2007it

SN 2007it was discovered in NGC 5530 by R. Evans on 2007 September 13 at $V = 13.5$ mag (Evans, Nitschki & Quirk 2007; Itagaki et al. 2007). Pre-discovery images taken with the All Sky Automated Survey 3 (ASAS-3) constrained the explosion date to be between 2007 September 4 and 6 (Pojmanski & Pojmanski 2007). We adopt an explosion date of 2007 September 5. Andrews et al. (2011b) studied SN 2007it in the optical and IR regime between 10 and 944 d after explosion. They classified it as a Type II-P supernova based on the plateau in its optical light curve between days 20 and 107.

At day 540 the optical lines of SN 2007it showed an IWC in the [O I] and Hα profiles. Andrews et al. (2011b) also analysed the IR SEDs at four epochs between days 351 and 944. Day 351 showed the presence of an IR excess, well before the estimated time of new dust formation from the optical light curves, which they attributed to scattering dust in a CSM producing a light echo. They also found

that the IR flux doubled in intensity at 5 μm between days 351 and 561, and at the same time saw a dimming in the visible light curve, which they attributed to dust formation in the ejecta. They modelled the 0.1–10 μm SED with MOCASSIN between days 351 and 944 and found that up to 1×10^{-4} M$_\odot$ of dust had formed in the ejecta by day 944.

We combined our day 3136 X-Shooter spectrum with our days 2780 and 3830 GMOS spectra, as all three spectra initially had fairly low S/N ratios and overplotting the three spectra did not show significant differences in line profile shape over time. The spectra were corrected for a recessional velocity of NGC 5530 of 1170 km s^{-1}. DAMOCLES models were made for 'day 3248' post-explosion, the average of the three epochs. The presence of a red scattering wing implies a silicate dust proportion larger than 50 per cent. The best-fitting models for a 50:50 AmC to silicate dust mixture and for 100 per cent silicate dust are plotted in Fig. 18, with model parameters listed in Table 8. A model using 50:50 AmC to silicate dust species with a grain radius of 0.3 μm and a dust mass of $\sim 0.008^{+0.05}_{-0.007}$ M$_\odot$, minimized the χ^2 value. The uncertainties on this value are taken from a Bayesian model of the Hα line of SN 2007it. It should be noted that it is difficult to accurately delineate the shape of the Hα profile, due to the low S/N of the combined spectra and the fact that the blue edge of the Hα profile is blended with the [O I] 6300, 6363 Å profile. Therefore, there is a large degree of uncertainty in the values of the model parameters.

3.2.11 SN 2010jl

SN 2010jl was discovered in UGC 5189A on 2010 November 3. Stoll et al. (2011) established an explosion date for SN 2010jl of 2010 October 9, from its detection in pre-discovery images, and noted that SN 2010jl was very luminous with a peak absolute magnitude of ~ -20. It was classified as a Type IIn near maximum light, from the presence of narrow lines emitted by flash-ionized CSM (Benetti et al. 2010; Yamanaka et al. 2010). It has been well studied at optical and IR wavelengths, with many authors estimating
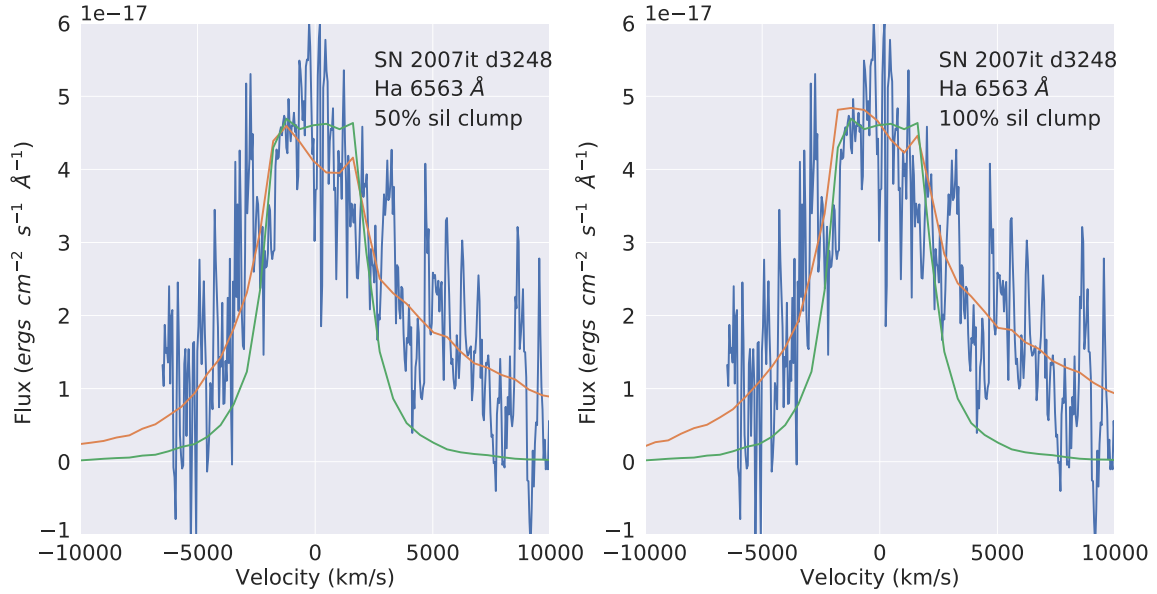
Figure 18. DAMOCLES models SN 2007it's Hα line profiles 3248 d post-explosion. The green line is the dust-free DAMOCLES model, and the orange line is the dust-affected model. Clumped dust models of 100 per cent astronomical silicates (left) and for a 50:50 astronomical silicate to AmC ratio (right) are shown. The gap blueward of -6000 km s^{-1} is where contaminating [O I] emission has been removed.

dust masses present in SN 2010jl. Several authors have modelled the optical and NIR line profiles first noted by Smith et al. (2012) after 30 d, and others have modelled the IR excess, also commencing 30 d after maximum light. Andrews et al. (2011a), Fransson et al. (2014), Sarangi, Dwek & Arendt (2018), and Bevan et al. (2020) all concluded that a light echo from pre-existing CSM dust was responsible for the IR excess before day 400, while Bevan et al. (2020) found that ejecta/CSM dust dominated the IR SED after this time. Estimates of the newly formed dust mass, likely present in the CDS/ejecta, range from $\sim(2.5\text{–}9.0) \times 10^{-4}$ M$_\odot$ at day 500 to $(1.5\text{–}3.0) \times 10^{-3}$ M$_\odot$ at day 800 (Maeda et al. 2013; Gall et al. 2014; Chugai 2018; Sarangi et al. 2018; Bevan et al. 2020).

We obtained a good S/N detection of the Hα emission profile in our day 1906 Gemini GMOS spectrum. Narrow nebular lines of Hα and [N II] 6584, 6548 Å were removed using the DIPSO ELF routine. The spectrum was corrected for a recessional velocity of UGC 5189A of 3167 km s^{-1}. We extrapolated the Bevan et al. (2020) day 1286 Hα model parameters for SN 2010jl to model our day 1906 Hα profile. We summarize their model below, which is described in more detail in section 4.2 of their paper. Their model consists of three components: a smooth slowly expanding CSM gas region emitting an IWC; a rapidly expanding smooth ejecta gas component producing a BC; and a clumped dust component. The bounds of the model were set by $R_{\rm out}$, representing the location of the forward shock, and $R_{\rm in}$, the location of the reverse shock. Instead of assuming free expansion, the velocity of emitting packets in the CSM were sampled from a power-law velocity distribution $p(v) \propto v^\alpha$, between the limits $V_{\rm max,IWC}$ and $V_{\rm min,IWC}$. The BC used a radius-independent power-law velocity distribution, $p(v) \propto v^\beta$, between the limits $V_{\rm max,BC}$ and $V_{\rm min,BC}$ where for continuity $V_{\rm min,BC} = V_{\rm max,IWC}$. A gas emissivity law $\rho \propto r^{-4}$ was used for both the ejecta and CSM components. The AmC dust was clumped with a filling factor of 0.1.

The best-fitting Hα model is shown in Fig. 19, with the model parameters listed in Table 7. We derive a day 1906 dust mass of 0.018 M$_\odot$, corresponding to a large optical depth of $\tau = 12.6$. This dust mass is larger than the dust mass of 0.005 M$_\odot$ derived by Bevan

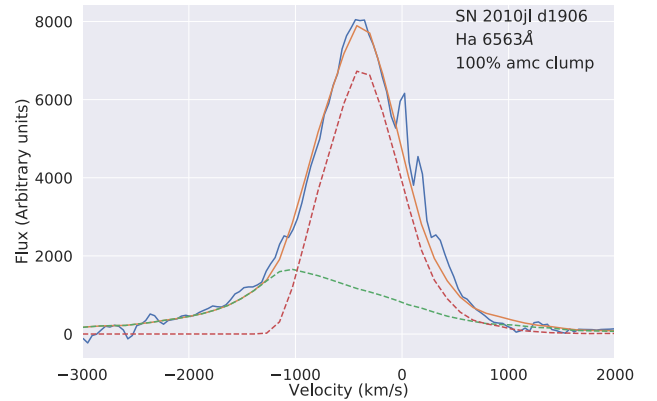
Figure 19. DAMOCLES models of SN 2010jl's Hα profile in the Gemini GMOS spectrum taken 1906 d post-explosion. The red and green dashed lines are the dust-affected DAMOCLES models of the IWC and BC, and the orange line is the sum of these two components. The clumped dust models are for 100 per cent AmC dust.

et al. (2020) for day 1286. As we could not quantify the uncertainty on the parameters using Bayesian inference due to the complex nature of the line profile, the uncertainties on the dust mass were found by fixing the other parameters and varying the dust mass until the best-fitting χ^2 value changed by 35 per cent. We also determined an uncertainty on the grain radius using the same method. The grain radius and its error limits were found to be $0.15^{+0.21}_{-0.14}$ µm, which is in agreement with the grain radius of 0.2 µm used by Bevan et al. (2020) in their DAMOCLES models.

3.2.12 SN 2011ja

SN 2011ja was discovered on 2011 December 18 in the galaxy NGC 4945, and was determined to be a Type II-P supernova with an explosion date of 2011 December 12 after a spectrum taken on
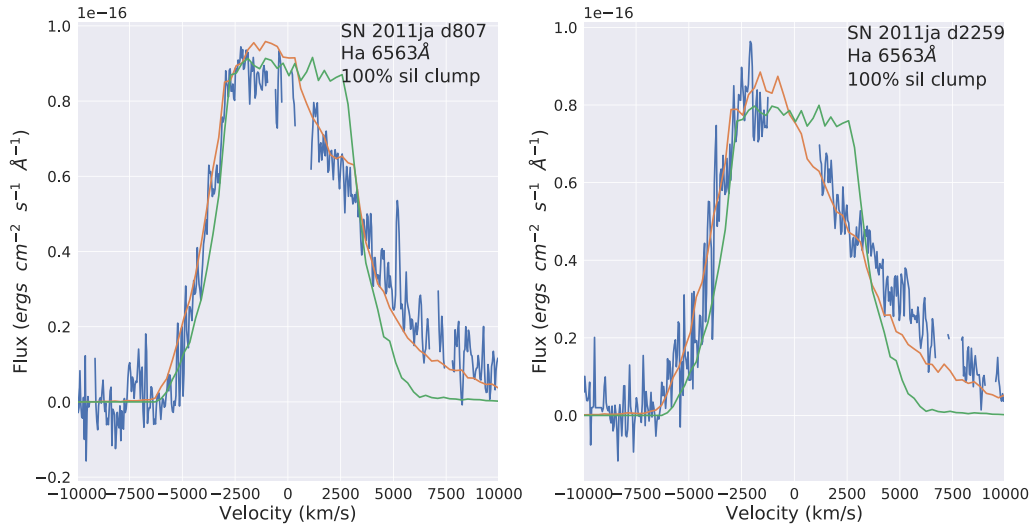
Figure 20. DAMOCLES models of SN 2011ja's Hα profile (orange line) in Gemini GMOS spectra (blue line) taken 807 d (left) and 2259 d (right) post-explosion. The green line is the dust-free model. Clumped dust models of 100 per cent silicate dust are shown.

Table 7. Parameters used in the DAMOCLES models of the Hα line of SN 2010jl 1906 d post-explosion for the best-fitting clumped AmC dust model. R_{out} and R_{in} are the outer and inner radii of the post-shock region. The optical depth is calculated from R_{in} to R_{out} at a wavelength of 6563 Å. α is the radius-independent gradient of the velocity distribution for the IWC, and β is the gradient of the velocity distribution for the BC.

$V_{max,IWC}$ (km s^{-1})	1150
$V_{min,IWC}$ (km s^{-1})	370
$V_{max,BC}$ (km s^{-1})	15 000
$V_{min,BC}$ (km s^{-1})	1150
α	0.8
β	−2.5
a (μm)	0.15
M_{dust} (10^{-2} M$_\odot$)	1.8
τ	12.6
R_{out} (10^{15} cm)	230
R_{in} (10^{15} cm)	26.4

2011 December 19 bore a strong resemblance to the spectrum of SN 2004et at an age of 7 d (Monard et al. (2011).

Andrews et al. (2016) studied the optical emission from SN 2011ja between days 84 and 807, from Gemini GMOS photometry and spectroscopy, and the near- and mid-IR emission using the *Spitzer* InfraRed Array Camera (IRAC) and the New Technology Telescope (NTT)/Son of ISAAC (SofI) data for days 8–857. They also noted signs of an early interaction with circumstellar material, from the emergence of a double peak in the broad Hα line in the optical spectrum, around the same time as noted by Chakraborti et al. (2013). They compared it to several Type IIn supernovae, stating it could belong in between Type II-P and IIn. Andrews et al. (2016) also noticed several indicators of dust formation starting around the same time as the CSM interaction. The optical line profiles started becoming visibly more blueshifted between days 84 and 112, and a near-IR excess was observed. To quantify the newly formed dust mass they modelled the dust emission SEDs from days 100 to 857 using the radiative transfer code MOCASSIN, finding $\sim 1 \times 10^{-4}$ M$_\odot$ of clumpy AmC dust at the latest epoch. They surmised this dust to have been formed in a CDS, similar to SN 1998S (Pozzo et al. 2005) and SN 2010jl (Gall et al. 2014). Tinyanont et al. (2016)

also modelled the *Spitzer* SED of SN 2011ja over several epochs, including at day 1382, as part of their large mid-IR survey SPitzer InfraRed Intensive Transients Survey (SPIRITS). They estimated the presence of 4×10^{-4} M$_\odot$ of graphite dust at day 807 and 10^{-3} M$_\odot$ of graphite dust at day 1382 post-explosion.

From a manual parameter investigation, we found best-fitting models to the Hα line in the GMOS spectra of SN 2011ja over four epochs: 807, 1275, 1611, and 2259 d post-explosion. All spectra were corrected for a recessional velocity of NGC 4945 of 560 km s^{-1} (Crook et al. 2007). We found the presence of a persistent red scattering wing in the Hα line at all four epochs, which became more pronounced with time, and the best-fitting models required a silicate dust composition with a grain radius of 0.15 μm. This disagrees with Tinyanont et al. (2016) and Andrews et al. (2016), who did not detect a 9–10 μm silicate emission feature in their IR SEDs of SN 2011ja. Our best-fitting models for the days 807 and 2259 Hα spectra using a 100 per cent silicate dust composition can be found in Fig. 20, while parameters for the models for all four epochs are listed in Table 8.

We ran a Bayesian simulation of the Hα line at 2259 d using 100 per cent silicate dust, the corner plot for which can be seen in Fig. A6. The median values for the dust mass and grain radius in the 1D posterior probability distributions closely matched our manually found best-fitting model values. Because of this, and the fact all line profiles had a similar S/N, we extrapolated the errors calculated from the Bayesian MCMC model on the dust mass to all other epochs. There is a steady increase of dust mass with time in SN 2011ja, with the mass increasing by a factor of $\sim$10 between day 807 ($2.3^{+0.67}_{-1.9} \times 10^{-4}$ M$_\odot$) and day 2259 ($2.5^{+0.75}_{-2.1} \times 10^{-3}$ M$_\odot$). Despite the difference in dust composition used, our dust masses at days 807 and 1275 agree well with those derived by Andrews et al. (2016) and by Tinyanont et al. (2016) at similar epochs, when taking into account our upper and lower limits.

3.2.13 SN 2012au

SN 2012au in NGC 4790 was discovered in on 2012 March 14 by the SNHunt project (Howerton et al. 2012) and shortly after was classified as a Type Ib supernova (Silverman et al. 2012; Soderberg et al. 2012). Milisavljevic et al. (2013) and Takaki et al. (2013) noted

Table 8. Parameters used in the DAMOCLES models of the broad emission lines of SN 1996cr, SN 1998S, SN 2007it, SN 2011ja, and SN 2012au for spherically symmetric smooth and clumped dust models. The 'Per cent Sil' column stands for percentage of the dust species that is astronomical silicate, while the remainder of the dust is AmC dust. The optical depth is calculated from R_{in} to R_{out} at the central line wavelengths ([O III] = 5007 Å, [O II] = 7319 Å, [O I] = 6300 Å, Hα = 6563 Å, and [S III] = 9069 Å).

SN	Epoch (d)	Line	Clumped?	Per cent Sil	a (μm)	V_{min} (km s^{-1})	V_{max} (km s^{-1})	β_{gas}	R_{out} (10^{15} cm)	R_{in} (10^{15} cm)	M_{dust} (10^{-2} M$_\odot$)	τ	χ^2
1996cr	7370	[O III]	No	0	0.15	2940	7000	6.0	442.8	186.0	0.80	1.46	
1996cr	7370	[O III]	Yes	0	0.12	2940	7000	6.0	442.8	186.0	3.5	5.18	
1996cr	7370	[O III]	No	100	0.04	2940	7000	6.0	442.8	186.0	20	0.89	
1996cr	7370	[O III]	Yes	100	0.05	2940	7000	6.0	442.8	186.0	120	7.97	
1996cr	7370	[O II]	No	0	0.15	2898	6900	6.0	436.5	183.3	0.80	0.97	
1996cr	7370	[O II]	Yes	0	0.12	2898	6900	6.0	436.5	183.3	3.5	5.33	
1996cr	7370	[O II]	No	100	0.04	2898	6900	6.0	436.5	183.3	40	0.66	
1996cr	7370	[O II]	Yes	100	0.05	2898	6900	6.0	436.5	183.3	120	2.89	
1996cr	7370	[O I]	No	0	0.15	2760	6900	5.6	436.5	174.6	0.80	1.13	
1996cr	7370	[O I]	Yes	0	0.12	2760	6900	5.6	436.5	174.6	3.5	5.52	
1996cr	7370	[O I]	No	100	0.04	2760	6900	5.6	436.5	174.6	20	0.99	
1996cr	7370	[O I]	Yes	100	0.05	2760	6900	5.6	436.5	174.6	120	4.58	
1996cr	7370	[S III]	No	0	0.15	2940	7000	6.0	442.8	186.0	0.80	1.03	
1996cr	7370	[S III]	Yes	0	0.12	2940	7000	6.0	442.8	186.0	3.5	4.21	
1996cr	7370	[S III]	No	100	0.04	2940	7000	6.0	442.8	186.0	40	0.50	
1996cr	7370	[S III]	Yes	100	0.05	2940	7000	6.0	442.8	186.0	120	3.10	
1996cr	8460	[O II]	No	0	0.15	2640	6600	5.5	482.48	192.97	1.0	1.10	
1996cr	8460	[O II]	Yes	0	0.15	2640	6600	5.5	482.48	192.97	3.5	2.80	
1996cr	8460	[O II]	No	100	0.06	2380	6800	5.0	497.04	173.96	50	1.30	
1996cr	8460	[O II]	Yes	100	0.06	2380	6800	5.0	497.04	173.96	80	2.40	
1998S	1170	Hα	No	100	0.08	3410	5500	0.5	55.60	34.47	1.00	2.45	
1998S	1170	Hα	Yes	100	0.08	3410	5500	0.5	55.60	34.47	2.50	10.6	
1998S	2148	Hα	No	100	0.08	3339	5300	0.5	97.63	61.51	1.00	1.51	
1998S	2148	Hα	Yes	100	0.08	3339	5300	0.5	97.63	61.51	4.00	5.44	
1998S	6574	Hα	No	100	0.10	2688	5600	2.3	260.0	124.0	14.0	2.32	
1998S	6574	Hα	Yes	100	0.08	2688	5600	2.3	260.0	124.0	15.0	4.99	
1998S	6574	[O I]	No	100	0.10	2688	5600	2.3	260.0	124.0	14.0	2.47	
1998S	6574	[O I]	Yes	100	0.10	2688	5600	2.3	260.0	124.0	15.0	4.46	1.26
2007it	3248	Hα	No	100	0.40	6860	14000	2.4	39.29	5.11	0.700	0.36	1.28
2007it	3248	Hα	Yes	100	0.40	6860	14000	2.4	39.29	5.11	0.900	0.46	1.91
2007it	3248	Hα	No	50	0.25	6860	14000	2.4	39.29	5.11	0.600	0.56	1.88
2007it	3248	Hα	Yes	50	0.30	6860	14000	2.7	39.29	5.11	0.800	0.61	1.37
2011ja	807	Hα	No	100	0.15	3038	6200	2.00	42.91	21.02	0.021	0.72	1.29
2011ja	807	Hα	Yes	100	0.15	3038	6200	2.00	42.91	21.02	0.023	0.96	1.24
2011ja	1275	Hα	No	100	0.15	2928	6100	2.00	66.88	32.10	0.060	0.81	1.24

Table 8 – *continued*

| SN	Epoch (d)	Line	Clumped?	Per cent Sil	a (μm)	V_{max} (km s^{-1})	V_{min} (km s^{-1})	β_{gas}	R_{out} (10^{15} cm)	R_{in} (10^{15} cm)	M_{dust} (10^{-2} M$_\odot$)	τ	χ^2
2011ja	1275	Hα	Yes	100	0.15	6100	2928	2.00	66.88	32.10	0.060	0.81	
2011ja	1611	Hα	No	100	0.15	6100	2745	2.00	84.91	38.21	0.070	0.52	
2011ja	1611	Hα	Yes	100	0.15	6300	2835	2.00	87.69	39.46	0.080	0.70	
2011ja	2259	Hα	No	100	0.15	6100	2928	2.00	113.5	54.47	0.300	1.51	
2011ja	2259	Hα	Yes	100	0.20	6100	2928	2.00	113.5	54.47	0.250	1.40	
2012au	2277	[O III]	No	0	0.20	4900	1274	3.10	96.40	25.06	0.025	0.57	
2012au	2277	[O III]	Yes	0	0.35	4900	1274	3.10	96.40	25.06	0.040	0.49	
2012au	2277	[O III]	No	100	1.50	4700	1222	3.10	92.46	24.04	0.500	0.66	
2012au	2277	[O III]	Yes	100	1.00	4900	1274	3.30	96.40	25.06	1.200	1.03	
2012au	2277	[O II]	No	0	0.20	5000	1150	3.10	98.37	22.62	0.025	0.48	
2012au	2277	[O II]	Yes	0	0.35	5000	1150	3.10	98.37	22.62	0.040	0.41	
2012au	2277	[O II]	No	100	1.50	5000	1150	3.30	98.37	22.62	0.400	0.48	
2012au	2277	[O II]	Yes	100	1.10	5000	1150	3.30	98.37	22.62	0.500	0.75	
2012au	2277	[O I]	No	0	0.20	5100	1224	3.50	100.3	24.08	0.023	0.51	
2012au	2277	[O I]	Yes	0	0.35	5100	1224	3.50	100.3	24.08	0.046	0.53	
2012au	2277	[O I]	No	100	1.50	5100	1224	3.50	100.3	24.08	0.450	0.60	
2012au	2277	[O I]	Yes	100	1.10	5100	1224	3.50	100.3	24.08	0.500	0.75	
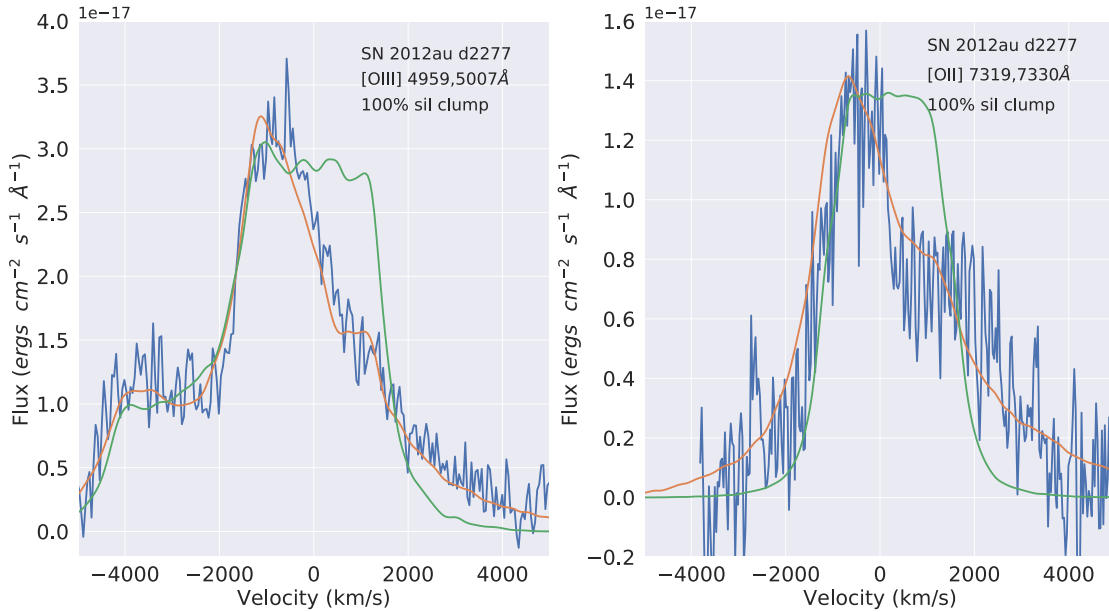
Figure 21. DAMOCLES models of SN 2012au's Hα profile (orange line) from the Gemini GMOS spectra (blue line) taken 2277 d post-explosion. The green line is the dust-free model. Clumped dust models of 100 per cent silicate dust are shown.

its similarity to a Type Ic. Milisavljevic et al. (2018) presented optical spectra of SN 2012au taken 2277 d after explosion, and noted the appearance of strong [O III] 4959, 5007 Å and [O II] 7319, 7330 Å emission, and a stark difference in the [O I] 6300, 6363 Å profile when compared to day 321 spectra. They attributed this to the turn-on of a pulsar wind nebula exciting oxygen-rich ejecta.

Our best-fitting DAMOCLES models for the day 2277 [O II] 7319, 7330 Å and [O III] 4959, 5007 Å spectra published by Milisavljevic et al. (2018) for SN 2012au are shown in Fig. 21 and the parameters can be found in Table 8. The [O III] and [O II] features required similar model parameters for the best-fitting models, implying a colocation of ionization species similar to that found for SN 1996cr. We found that large silicate grains of 1.0 μm radius; carbon grains of 0.4 μm radius; or a 50:50 carbon to silicate mixture of 0.5 μm radius grains, fitted the oxygen line profiles best. The observed [O I] 6300, 6363 Å profile on day 2277 contained what we assumed to be a contaminating emission feature located between −300 and −800 km s⁻¹, of uncertain origin. When it was removed the resulting [O I] profile was well fitted with similar parameters to those required to fit the [O II] and [O III] profiles (Table 8).

We ran a Bayesian model assuming 100 per cent AmC dust, which fit the [O III] and [O II] lines in SN 2012au simultaneously. The median grain radius was 0.3 μm, whose large uncertainty limits comfortably included our initially derived grain radius. Scaling the uncertainties found from the Bayesian analysis to our best-fitting 50:50 AmC to silicate dust mass, gives a dust mass at day 2277 in SN 2012au of $1.0^{+0.43}_{-0.90} \times 10^{-3}$ M$_\odot$, which is similar to the dust mass derived for SN 2011ja at a similar epoch.

4 DUST MASSES AND DUST PROPERTIES

4.1 CCSN dust masses as a function of ejecta age

The ejecta dust masses derived for the CCSNe in our sample from their best-fitting models are summarized in Table 9. The values plotted for SN 2012aw, which were derived as part of the ORBYTS

outreach programme, are presented in more detail by Niculescu-Duvaz et al. (submitted). The dust mass derived for the IWC of SN 2004et is not included, as there is the possibility that this dust could have formed before the supernova explosion. We plot these ejecta dust masses against age since explosion in Fig. 22. As discussed in the individual sections, for epochs where we could not determine the dust species, we use a dust mass for a 50:50 carbon to silicate mass ratio, and where we cannot determine the grain radius, we have plotted the dust mass for a 50:50 carbon to silicate mass ratio using a grain radius of 0.10 μm in order to constrain a lower limit to the dust mass. Some error bars are taken as percentage errors of the 16th and 84th quartiles on the median dust mass value in the marginalized 1D dust mass probability distributions derived from the Bayesian modelling process. As our Bayesian models were generally run for 100 per cent AmC or 100 per cent silicate dust, for supernovae where we could not determine the dust species we then scaled these percentage errors to the best-fitting dust mass derived from a manual fit using a 50:50 AmC to silicate dust ratio, in order to derive upper and lower limits. We justify this approach by the fact that when we ran Bayesian models for 100 per cent AmC or 100 per cent silicate for the [O II] feature of SN 1979C at day 13 903, the error bars from the 1D posterior distribution of the dust mass in both cases only varied by a factor of ∼1.3. Other error limits are taken from a 35 per cent variation in χ^2 when changing the dust mass whilst keeping all other parameters fixed. These values in general tend to have tighter error limits, but this does not mean that the dust mass determined is more accurate. We consider the size of the uncertainties determined from the Bayesian analyses to be a more accurate representation of the dust mass uncertainties.

We used the least-squares function found in the PYTHON SCIPY.OPTIMIZE package to fit our data points in Fig. 22 with a sigmoid curve similar to that used by Wesson et al. (2015), to fit the time evolution of SN 1987A's dust mass, defined by the equation

$$M_{\rm d}(t) = a\,{\rm e}^{b{\rm e}^{ct}}. \tag{3}$$

Table 9. A summary of the best-fitting ejecta clumped dust masses for all the observation epochs of the CCSNe modelled in this sample. These are the values plotted in Fig. 22. The 'Per cent Sil' column stands for the mass percentage of the dust species that consists of astronomical silicate, where the remainder of the dust is AmC dust. The listed optical depths τ_λ are calculated from R_{in} to R_{out} at the central line wavelengths given in column 4.

| SN	Type	Epoch (d)	λ (Å)	a (μm)	% Sil	V_{max} (km s^{-1})	V_{min} (km s^{-1})	β	R_{out} (10^{15} cm)	R_{in} (10^{15} cm)	τ_λ	M_{dust} (M$_\odot$)
1957D	II	11 371	5007	0.40	50	5800	870	2.5	1079.00	140.30	0.42	$1.20^{+4.8}_{-1.18} \times 10^{-2}$
1957D	II	19 459	5007	0.40	50	6800	1020	2.4	1265.00	140.30	0.13	$3.50^{+7.50}_{-3.00} \times 10^{-2}$
1957D	II	21 535	5007	0.40	50	7500	962	2.5	1377.00	140.30	0.29	$5.00^{+49.80}_{-4.78} \times 10^{-2}$
1970G	II-L	16 733	6563	0.10	100	6600	3960	−0.1	954.20	572.50	1.12	$0.10^{+1.41}_{-0.097}$
1979C	II-L	5146	7319	0.10	50	6800	5440	4.5	297.00	237.00	15.00	$0.10^{+0.40}_{-0.07}$
1979C	II-L	10 575	7319	0.15	50	6600	4950	5.5	603.00	452.30	11.00	$0.65^{+0.87}_{-0.43}$
1979C	II-L	13 903	7319	0.15	50	6600	3696	2.2	793.00	444.10	4.58	$0.30^{+0.13}_{-0.15}$
1980K	II-L	13 706	6563	0.10	100	5300	4505	1.5	593.10	504.00	2.91	$0.60^{+3.29}_{-0.57}$
1986E	II-L	3712	6563	0.10	50	7100	3337	3.0	225.80	106.10	2.15	$3.00^{+0.00}_{-2.40} \times 10^{-2}$
1986E	II-L	10 619	6563	0.10	50	6600	3102	3.0	603.80	283.80	1.07	$7.00^{+0.00}_{-6.50} \times 10^{-2}$
1986E	II-L	11 723	6563	0.10	50	6600	2640	3.0	668.30	314.10	1.02	$7.00^{+0.00}_{-6.50} \times 10^{-2}$
1993J	IIn	8417	5007	0.10	50	5800	4408	5.0	421.80	320.60	2.17	$4.00^{+13.0}_{-3.8} \times 10^{-2}$
1996cr	IIn	7370	7319	0.11	50	6900	2898	6.0	436.50	183.30	5.47	$0.10^{+0.13}_{-0.078}$
1996cr	IIn	8460	7319	0.11	50	6900	2380	5.0	497.04	173.96	4.11	$0.15^{+0.30}_{-0.14}$
1998S	IIn	1170	6563	0.08	100	5500	3410	0.5	55.60	34.47	10.60	$2.50^{+4.10}_{-1.60} \times 10^{-2}$
1998S	IIn	2132	6563	0.08	100	5300	3339	0.5	97.63	61.51	5.44	$4.00^{+6.00}_{-3.30} \times 10^{-2}$
1998S	IIn	6574	6563	0.10	100	5600	2688	2.3	260.00	124.00	4.99	$0.15^{+0.54}_{-0.14}$
2004et	II-P	646	6563	0.20	100	9500	7410	1.7	53.02	39.24	0.57	$5.00^{+24.00}_{-0.60} \times 10^{-4}$
2004et	II-P	3868	6563	0.20	100	6000	5400	2.0	200.50	180.50	1.31	$1.00^{+89}_{-0.98} \times 10^{-2}$
2007it	II	3248	6563	0.30	50	14 000	6860	2.7	39.29	5.11	0.61	$8.00^{+3.00}_{-5.00} \times 10^{-3}$
2010jl	IIn	1906	6563	0.15	0	1150	370	2.0	230.00	26.40	12.60	$1.80^{+0.75}_{-0.75} \times 10^{-2}$
2011ja	II	801	6563	0.15	100	6200	3038	2.0	42.91	21.02	0.72	$2.30^{+7.11}_{-1.93} \times 10^{-4}$
2011ja	II	1269	6563	0.15	100	6100	2928	2.0	66.88	32.10	0.81	$6.00^{+18.50}_{-5.04} \times 10^{-4}$
2011ja	II	1611	6563	0.15	100	6300	2835	2.0	87.69	39.46	0.70	$8.00^{+24.72}_{-6.72} \times 10^{-4}$
2011ja	II	2153	6563	0.20	100	6100	2928	2.0	113.50	54.47	1.40	$2.50^{+7.73}_{-2.10} \times 10^{-3}$
2012au	Ib/c	2277	5007	0.50	50	5000	1150	3.3	98.37	22.62	0.75	$1.20^{+4.29}_{-0.95} \times 10^{-3}$
2012aw	II-P	1158	6563	0.30	100	5500	1100	1.3	55.03	11.01	0.70	$2.00^{+8.86}_{-1.55} \times 10^{-4}$
2012aw	II-P	1863	6563	0.30	100	5100	663	1.5	82.09	10.67	1.02	$6.00^{+21.9}_{-3.60} \times 10^{-4}$
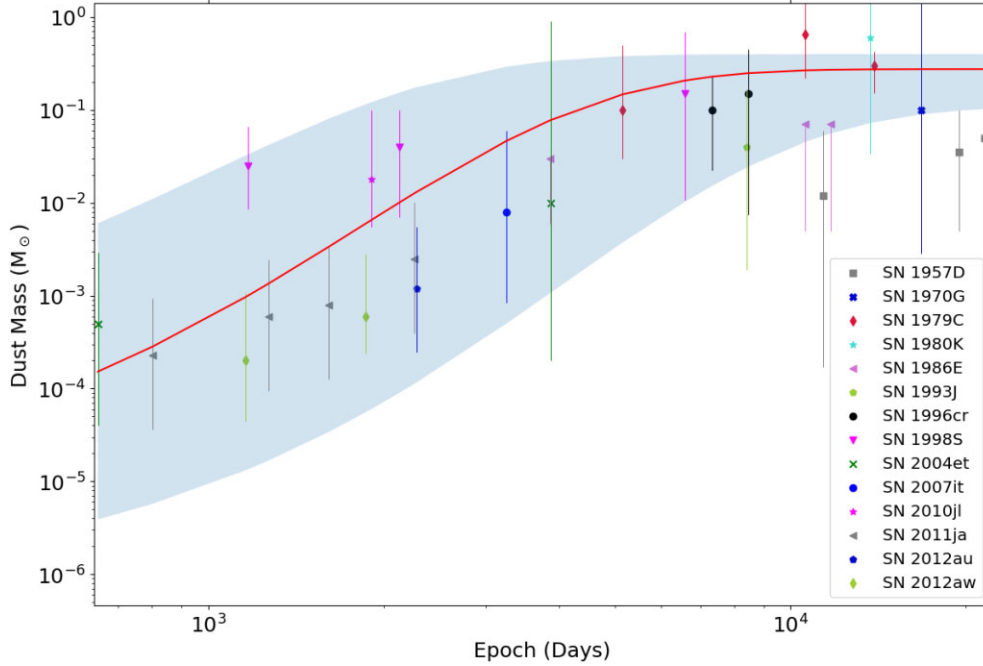
Figure 22. Dust mass against time post-explosion, for the sample of CCSNe modelled in this work (see Table 9), with the least-squares minimized sigmoid curve defined by equation (3) overplotted. The grey band encloses the error region on the best-fitting sigmoid curve parameters, where the errors are derived from a Monte Carlo bootstrap simulation and are provided in the text.

Such a curve provides a natural limit to the growth of the parameter being fitted, which might correspond in this case to the exhaustion of condensable heavy elements. a can be interpreted as the dust mass at saturation, in $M_\odot$, that is formed by CCSNe, b describes when the peak dust formation epoch occurs such that a more negative b leads to a later onset of dust formation, and c describes the rate of peak dust formation, such that a more negative value of c corresponds to faster dust formation. We used a Monte Carlo simulation to bootstrap our data plotted in Fig. 22. We generated 1000 data sets randomly drawn from a normal distribution to quantify the best-fitting curve parameters and their associated uncertainties. We derived curve fit parameters of $a = 0.23^{+0.17}_{-0.12}$ $M_\odot$, $b = -10.51^{+4.51}_{-1.49}$, and $c = -4.73^{+2.25}_{-5.37}) \times 10^{-4}$ d^{-1}, where the best-fitting parameter values for a and c were taken as the median of the resulting parameter distributions of the bootstrapped samples, and all uncertainties are taken as the 16th and 84th quartiles of this distribution. The mean for the b value was taken as the least-squares fitting algorithm bimodally preferred values between the upper and lower quartiles. The median and quartiles were preferred to the mean and standard deviation as the parameter distributions were non-Gaussian.

Fig. 23 supplements our DAMOCLES-derived dust masses with dust masses from various sources in the literature, as listed with references in Table A1. As discussed in Section 1, for supernovae observed during their photospheric phase (up to ∼150 d post-explosion) we discount dust mass measurements made via line profile fitting, as blueshifted emission line peaks before these times can be created by occultation of redshifted emission by the optically thick, steeply distributed ejecta gas (see Anderson et al. 2014).

Although some of the dust masses taken from the literature were determined using DAMOCLES, many were determined from optical–IR SED fitting. For the latter cases we excluded dust masses based on 'warm' *Spitzer* photometry that only extended to 4.5 μm or less, potentially missing cooler dust emitting at longer wavelengths.

Overall, the data points that we took from the literature consisted of dust masses at additional epochs for six of our Fig. 22 sample, together with multi-epoch dust mass determinations for 11 further CCSNe and dust mass estimates for six CCSNRs older than 300 yr. Since a large number of the literature dust masses plotted in Fig. 23 did not have any uncertainty limits associated with them, the fit to Fig. 23 did not take individual error limits into account.

A sigmoid curve using equation (3) was fit to the data points in Fig. 23, using the same method as described for the curve fit procedure on the data in Fig. 22, yielding $a = 0.42^{+0.09}_{-0.05}$ $M_\odot$, $b = -8.0^{+4.0}_{-2.0}$ and $c = -2.88^{+1.03}_{-1.27}) \times 10^{-4}$ d^{-1}. The sigmoid curve fits plotted in Figs 22 and 23 require very similar values for b and c. At $0.42^{+0.09}_{-0.05}$ $M_\odot$, the value of a, the dust mass at saturation, is derived to be larger for the Fig. 23 sample than the value of $a = 0.23^{+0.17}_{-0.12}$ $M_\odot$ found for our DAMOCLES data set plotted in Fig. 22. For the sigmoid curve plotted in Fig. 23, the dust mass reaches 75 per cent of its saturation value within 30 yr.

The uncertainties on the value of b are large for the sigmoid curve plotted in Fig. 22 due to the relative lack of dust mass samples at early times (<1000 d post-explosion), such that it is difficult to determine the floor of the sigmoid curve: this explains why the error band on the best-fitting sigmoid curve at early times is so broad. However, the value of the dust mass parameter a is well constrained in both cases (as is the value of c in the case of the larger sample).

There appears to be a real dispersion in some of the SNR dust masses plotted in Fig. 23. Cas A has three dust mass determinations from independent methods that all lie between 0.5 and 1.1 $M_\odot$ (B17; De Looze et al. 2017; Niculescu-Duvaz et al. 2021), while the dust mass determined for the Crab Nebula by De Looze et al. (2019) was 0.040 ± 0.008 $M_\odot$. The sigmoid curve fits plotted in Figs 22 and 23 have similar slopes to that found by Wesson et al. (2015) for SN 1987A alone, but have a lower value for the saturation dust mass parameter compared to the Wesson et al. (2015) value of $a =$
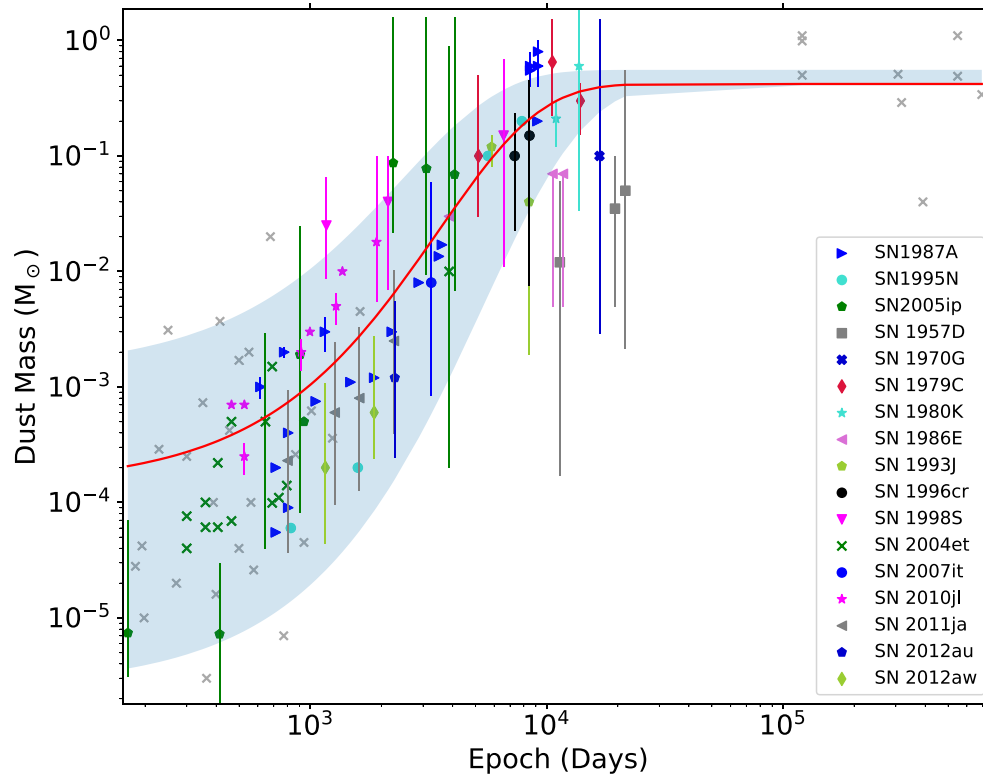
Figure 23. Dust mass against time (age post-explosion) for the sample of CCSNe modelled with DAMOCLES (coloured points), combined with literature dust mass determinations (grey crosses) with details summarized in Table A1. A least-squares minimized sigmoid curve defined by equation (3) is overplotted in red. The grey band encloses the error region on the best-fitting sigmoid curve parameters, where the errors are derived from a Monte Carlo bootstrap simulation and are provided in the text. Individual dust mass error limits were not taken into account in the fitting, since many of the literature values lacked such error estimates. The CCSNe for which DAMOCLES dust mass determinations exist are identified by the key in the inset box. As a function of increasing age, the six SNRs for which dust masses are plotted are Cas A, G29.7−0.3, G21.5−0.9, the Crab Nebula, G54.1+0.3, and G11.2−0.3, with ages ∼330, 850, 880, 1100, 1500, 1900 yr, respectively. Note that many of the supplementary data points plotted below 1500 d are based on *Spitzer* mid-IR flux measurements; we only used such dust masses when the spectral coverage extended to at least 8 μm.

$1.0 \, M_\odot$ derived from a range of observations of SN 1987A at multiple epochs. It is therefore possible that SN 1987A has formed a larger dust mass than other SNe of similar ages. The curve plotted by Bevan et al. (2019) in their fig. 10, which was a fit to the dust mass evolution for just SN 1987A and SN 2005ip, does not fit most of the data points in our Fig. 22. Their curve exhibits larger dust masses at early times, a less steep dust mass growth with time, a later dust mass growth plateau, and a larger dust mass saturation than that found by our best-fitting sigmoid curve. However, their curve well fitted our Type IIn dust mass data points for SN 2010jl and SN 1998S. Their curve would also fit the dust masses found here for SN 1996cr assuming a 100 per cent silicate dust composition.

The dust mass growth plot in fig. 1 of Gall & Hjorth (2018) has a plateau value of $0.40 \pm 0.07 \, M_\odot$, similar to the saturation value of $0.42^{+0.09}_{-0.05} \, M_\odot$ for the curve in Fig. 23. The latter curve predicts that SNe produce less dust on average at ages <40 yr than that plotted by Gall & Hjorth (2018), which has a steeper dust growth rate before this time, and plateaus sooner at an age of 20 yr rather than at 40 yr.

Of the 14 CCSNe in our sample, four were Type II-L supernovae, namely SN 1970G, SN 1979C, SN 1980K, and SN 1986E. All had spectra taken beyond 30 yr after outburst, so from the sigmoid curve fit to the dust mass versus ejecta age distribution in Fig. 23, we should expect dust masses of $0.42^{+0.09}_{-0.05} \, M_\odot$, while the average dust mass from the latest observed epochs for these four Type II-L SNe was $0.35 \pm 0.33 \, M_\odot$. We found that there was a large spread in the

radial gas/dust distributions of these Type II-L supernovae, perhaps indicating a diversity in the evolutionary history of their progenitor stars. SN 1970G and SN 1980K both exhibit similar optical spectra and required similar [O I] and Hα emitting gas distributions, however SN 1970G was found to have a lower dust mass than SN 1980K by a factor of ∼6. The dust mass found for SN 1979C is the highest of the four Type II-L objects and its optical spectrum exhibits the highest degree of ionization of the four. It has been suggested to have a black hole at its centre (Patnaude, Loeb & Jones 2011), which would imply a large progenitor mass and this could possibly account for its larger dust mass when compared to other CCSNe of a similar age.

Four of the CCSNe in our sample were of Type IIn (SN 1993J, SN 1996cr, SN 1998S, and SN 2010jl), a classification indicating the presence of circumstellar material that produces a narrow emission line, usually superposed on a broader profile from the supernova ejecta. Of the four, SN 1998S and SN 2010jl are outliers to the sigmoid dust growth curve, presenting high dust masses at early epochs of up to 2000 d in comparison to other Type IIL/IIP supernovae. Their data points are well fit by the SN 2005ip dust growth curve seen in fig. 11 of Bevan et al. (2019). The increased dust mass could be due to the fact that there is an additional CDS component at early times that produces extra dust. For SN 1998S, at the late epoch of 6500 d the dust mass derived is comparable to those of SN 1979C, SN 1987A, and SN 1996cr, the latter another Type IIn.
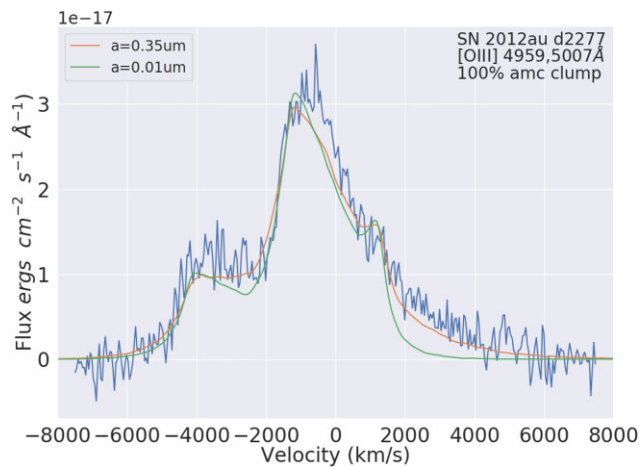
Figure 24. The best-fitting model for SN 2012au's day 2277 [O III] 4959, 5007 Å doublet feature, using a clumped amorphous carbon dust distribution with a grain radius of 0.35 μm and a dust mass of 4×10^{-4} M$_\odot$, with the other parameters described in Table 8. This can be seen to provide a better fit to the observed profile than the best-fitting model using clumped amorphous carbon dust with a smaller grain radius of 0.01 μm and a dust mass of 1×10^{-4} M$_\odot$, with otherwise matching model parameters.

The use of the nucleosynthetic yields of Woosley & Heger (2007), as extracted by Temim et al. (2017), predicts that a star with an initial mass of 15 M$_\odot$ can produce 0.13 M$_\odot$ of carbon and 0.23 M$_\odot$ of silicate constituents, while an 18 M$_\odot$ star can produce 0.20 M$_\odot$ of carbon and 0.35 M$_\odot$ of silicates. Comparing these limits with the carbon and silicate dust masses that can be found in Table 9 indicates that the only values that may exceed these constraints are the day 10 575 dust mass for SN 1979C ($0.65^{+0.87}_{-0.43}$ M$_\odot$ split equally between amorphous carbon and silicates) and the day 13 706 silicate dust mass for SN 1980K ($0.60^{+3.3}_{-0.57}$ M$_\odot$).

4.2 CCSN dust grain properties

We were able to put some constraints on the dust grain albedo for most of the CCSNe in our sample, either from the presence of an extended red scattering wing in the line profiles, or from exploiting the wavelength dependence of dust absorption. For some objects, such as SN 1979C, we also obtained 1D probability density distribution curves for the grain radii from a Bayesian analysis. Six of the CCSNe in our sample (SN 1970G, SN 1980K, SN 1998S, SN 2004et, SN 2007it, and SN 2011ja) showed large red scattering wings in their line profiles, which required close to 100 per cent silicate dust to fit. For all these SNe, silicate grain radii of the order of 0.1–0.3 μm were required, which yield an optical albedo of ~0.9. For the SNe where we were able to constrain the dust grain albedo but not the species, we could constrain the grain size for the cases of either 100 per cent AmC, 100 per cent silicate, or 50:50 carbon to silicate mixes. From their 1D probability distributions values derived from a Bayesian analysis, SN 2012au and SN 1957D require median grain radii of 0.2 and 0.3 μm, respectively, for 100 per cent AmC grains, where the probability distributions plateau at large grain radii of ~1 μm.

Fig. 24 demonstrates how the grain radius affects the presence of a scattering wing in a model of the [O III] 4959, 5007 Å profile of SN 2012au at 2277 d post-explosion. The orange line shows the best-fitting model of SN 2012au for a 100 per cent amorphous carbon dust species using a grain radius of 0.35 μm and a dust mass of

4×10^{-4} M$_\odot$, whereas the green line is the best-fitting model using a smaller grain radius of 0.01 μm, a dust mass of 1×10^{-4} M$_\odot$, and otherwise matching parameters as those generating the orange line. It is clear that in this case, as was the case for other SNe modelled in this work, a visual inspection can rule out small dust grain radii based on goodness of fit to the red scattering wing in emission line profiles.

SN 1979C and SN 1996cr are the two objects in our sample that are most likely to have grain radii <0.2 μm. In the case of SN 1996cr, for dust grain radii ~0.1 μm there should be a wavelength dependence of dust extinction for wavelengths $>2\pi a = 0.63$ μm, while its spectra had broad emission lines ranging between 6300 and 9069 Å. This, and the fact that in our models multiple emitting ionic species were found to be colocated, allowed us to constrain the 100 per cent clumped AmC grain radius to be 0.12 μm, and 0.05 μm for SN 1996cr for clumped 100 per cent silicate dust. The high S/N of the line profiles in our spectra of SN 1979C allowed us to use a Bayesian analysis to constrain the median 100 per cent AmC grain radius to be 0.1 μm, with an upper limit of 0.3 μm. This translates for a 50:50 AmC to silicate mix to a single grain radius of ~0.2 μm. For SN 1970G, SN 1993J, and SN 1986E we were unable to constrain the dust grain species or radius, while for our model of SN 2010jl at day 1906, we utilized previous grain radius information from Bevan et al. (2020) for our models. Therefore, we find that the majority of the objects in our sample require 'medium-sized' dust grains with radii from 0.1 to 0.5 μm, regardless of composition. The large grain radii that we find are in agreement with other works (e.g. Gall et al. 2014; Owen & Barlow 2015; Wesson et al. 2015; B17; Priestley et al. 2020).

From hydrodynamic grain destruction modelling, Slavin et al. (2020) found that, considering grain sputtering only, 30 per cent of carbonaceous grains with radius of >0.1 μm and 10 per cent of silicates with a radius of 0.2 μm, increasing up to 20 per cent for larger silicate grains, can survive processing through a typical supernova reverse shock. From their hydrodynamic grain destruction models Kirchschlager et al. (2019) and Kirchschlager, Barlow & Schmidt (2020) found that for initial lognormal grain size distributions peaking at 0.1 μm, between 15 per cent and 50 per cent of silicate grains would survive an encounter with the reverse shock, for a range of clump density contrasts, where their simulations treated sputtering, grain–grain collisions and ion impact trapping. Currently it is difficult to predict theoretically what fraction of CCSNe will have surviving dust masses >0.1 M$_\odot$, the minimum dust mass needed per CCSN, according to Morgan & Edmunds (2003) and Dwek et al. (2007), in order for them to be candidates as the main stellar dust producers in the Universe.

5 CONCLUSIONS

We have modelled the red–blue asymmetries in the optical line profiles of 13 supernovae, using DAMOCLES to determine dust masses and other ejecta parameters. Prior to this work, many dust mass measurements existed for CCSNe aged <4 yr, corresponding to when IR dust emission may have been detectable by *Spitzer*, but relatively few dust mass measurements existed for CCSNe older than this. We have greatly increased the sample of dust mass measurements available for CCSNe with ages between 5 and 60 yr, Our measurements, combined with literature values, are plotted in Fig. 23 to generate the most well-sampled and informative supernova dust mass growth curve to date.

A striking aspect of our results is that apart from SN 1998S, which had a dust mass of $2.5^{+4.1}_{-1.6} \times 10^{-2}$ M$_\odot$ at day 1170, at epochs earlier

than 2200 d none of the derived dust masses listed in Table 9 exceed 2.5×10^{-3} M$_\odot$. This stands in contrast with predictions from a range of recent theoretical studies of dust formation in CCSN ejecta, which have typically predicted that ≥ 0.1 M$_\odot$ of dust should have formed within 1000 d after outburst (e.g. Sarangi & Cherchneff 2013, 2015; Biscaro & Cherchneff 2014; Mauney & Lazzati 2018; Sarangi et al. 2018; Sluder et al. 2018; Brooker et al. 2022). Our results indicate that CCSNe can indeed form dust masses >0.1 M$_\odot$, but over much longer time-scales.

The dust mass growth with time for all the CCSN epochs modelled in this work is well described by a sigmoid curve similar to that fitted to SN 1987A's dust mass evolution by Wesson et al. (2015). The sigmoid curve plotted in Fig. 22 implies that 90 per cent of the saturation dust mass of $0.23^{+0.17}_{-0.12}$ M$_\odot$ is reached after about 10^4 d ($\sim$30 yr) post-outburst. For the expanded sample that includes supplementary dust mass estimates from the literature, we find a similar period to reach 75 per cent of the saturation dust mass of $0.42^{+0.09}_{-0.05}$ M$_\odot$ (Fig. 23).

For most of the CCSNe modelled we have put constraints on the dust grain radii for dust species consisting of either 100 per cent AmC, 100 per cent astronomical silicates, or a 50:50 mixture of the two species. Inferred grain radii $>0.1\,\mu$m for either carbon or silicate dust species are common in our models. For SN 1970G, SN 1986E, and SN 1993J, where we could not constrain the grain radii or dust species, we have provided a lower limit for the dust mass, assuming the dust is made from a 50:50 AmC to silicate dust grain mixture with a grain radius of 0.1 μm. For SN 1980K, SN 1998S, SN 2007it, and SN 2011ja we constrained the grain species to have a high silicate proportion. Slavin et al. (2020) and Kirchschlager et al. (2020) predicted a dust destruction rate for grain radii $>0.1\,\mu$m of $\sim$20–50 per cent for a silicate composition, and Slavin et al. (2020) predicted a dust destruction rate of $\sim$30 per cent for an amorphous carbon composition. Given our value of 0.42 M$_\odot$ produced by an average CCSN and given these dust destruction rates, 0.1–0.2 M$_\odot$ would survive the passage of the reverse shock. This suggests that CCSNe can contribute a large proportion of the dust formed in high-redshift galaxies. The model parameters found for the CCSNe studied here, particularly their dust masses, compositions and grain radii, will hopefully help contextualize further calculations of dust destruction rates, which are crucial to determining the overall contribution of CCSNe to the dust budget of the Universe.

Out of the eight SNe in our DAMOCLES sample that are over 20 yr old, six have formed dust masses >0.1 M$_\odot$. Amongst the four Type II-L SNe studied here (SN 1970G, SN 1979C, SN 1980K, and SN 1986E), there is a large range in the dust masses that have formed 30 yr or more after outburst (0.07–0.60 M$_\odot$; see Table 9) and in their deduced geometries (see Fig. A7). For SN 1979C we find that the oxygen- and hydrogen-emitting regions are not colocated. We find a best-fitting model in each case where the dust must be coupled to the freely expanding oxygen ejecta, and where the Hα emitting shell is outside the dusty oxygen-emitting regions. For the other Type II-L's, the hydrogen- and oxygen-emitting regions were found to be colocated, although SN 1986E exhibited an IWC in both its hydrogen and oxygen emission line profiles, which was not the case for SN 1980K or SN 1970G.

Our work indicates that at similar epochs the four Type IIn objects may have formed more dust than the five Type II and II-P objects (see Table 9). More dust masses are needed for each CCSN subtype at a range of ages, while tighter progenitor mass limits are required if we are to establish clear links between CCSN subtypes, progenitor masses, and ejecta dust properties.

Many of the objects modelled in this work warrant follow-up observations over an extended period of time, since for many their dust masses are inferred to have not finished increasing.

DATA AVAILABILITY

The DAMOCLES code, with Bayesian implementation, is available at https://github.com/damocles-code/damocles. Wavelength-calibrated copies of our Gemini GMOS and VLT X-Shooter spectra for the SNe listed in Tables 1 and 2 are available in the WISeREP archive (https://wiserep.weizmann.ac.il/).

REFERENCES

Anderson J. P. et al., 2014, MNRAS, 441, 671
Andrews J. E. et al., 2010, ApJ, 715, 541
Andrews J. E. et al., 2011a, AJ, 142, 45
Andrews J. E. et al., 2011b, ApJ, 731, 47
Andrews J. E. et al., 2016, MNRAS, 457, 3241
Arendt R. G., Dwek E., Kober G., Rho J., Hwang U., 2014, ApJ, 786, 55
Baluja K. L., Zeippen C. J., 1988, J. Phys. B: At. Mol. Opt. Phys., 21, 1455
Barbon R., Ciatti F., Rosino L., 1979, A&A, 72, 287
Baron E., Hauschildt P. H., Branch D., Wagner R. M., Austin S. J., Filippenko A. V., Matheson T., 1993, ApJ, 416, L21
Bauer F. E., Brandt W. N., Sambruna R. M., Chartas G., Garmire G. P., Kaspi S., Netzer H., 2001, AJ, 122, 182
Bauer F. E., Dwarkadas V. V., Brandt W. N., Immler S., Smartt S., Bartel N., Bietenholz M. F., 2008, ApJ, 688, 1210
Benetti S., Bufano F., Vinko J., Marion G., Pritchard T., Wheeler J., Chatzopoulos E., Shetrone M., 2010, Cent. Bureau Electron. Telegrams, 2536, 1
Bertoldi F., Carilli C. L., Cox P., Fan X., Strauss M. A., Beelen A., Omont A., Zylka R., 2003, A&A, 406, L55
Bevan A., 2018, MNRAS, 480, 4659
Bevan A., Barlow M. J., 2016, MNRAS, 456, 1269
Bevan A., Barlow M. J., Milisavljevic D., 2017, MNRAS, 465, 4044 (B17)
Bevan A. et al., 2019, MNRAS, 485, 5192
Bevan A. M. et al., 2020, ApJ, 894, 111
Biscaro C., Cherchneff I., 2014, A&A, 564, A25
Bocchio M., Jones A. P., Slavin J. D., 2014, A&A, 570, A32
Bouchet P., Danziger I. J., Gouiffes C., della Valle M., Moneti A., 1996, in McCray R., Wang Z., eds, Proc. IAU Colloq. 145, Supernovae and Supernova Remnants. Cambridge Univ. Press, Cambridge, p. 201
Brooker E. S., Stangl S. M., Mauney C. M., Fryer C. L., 2022, ApJ, 931, 85
Buta R. J., 1982, PASP, 94, 578
Cappellaro E., della Valle M., Iijima T., Turatto M., 1990, A&A, 228, 61
Cappellaro E., Danziger I. J., Turatto M., 1995, MNRAS, 277, 106
Chakraborti S. et al., 2013, ApJ, 774, 30
Chawner H. et al., 2019, MNRAS, 483, 70
Chugai N. N., 2018, MNRAS, 481, 3643

Crook A. C., Huchra J. P., Martimbeau N., Masters K. L., Jarrett T., Macri L. M., 2007, ApJ, 655, 790

De Looze I., Barlow M. J., Swinyard B. M., Rho J., Gomez H. L., Matsuura M., Wesson R., 2017, MNRAS, 465, 3309

De Looze I. et al., 2019, MNRAS, 488, 164

Detre L., Lovas M., 1970, IAU Circ., 2269, 1

Draine B. T., Lee H. M., 1984, ApJ, 285, 89

Dwek E., 1983, ApJ, 274, 175

Dwek E., Galliano F., Jones A. P., 2007, ApJ, 662, 927

Dwek E., Sarangi A., Arendt R. G., 2019, ApJ, 871, L33

Evans R. O., Nitschki D., Quirk S., 2007, Cent. Bureau Electron. Telegrams, 1065, 1

Fabbri J. et al., 2011, MNRAS, 418, 1285

Fassia A. et al., 2000, MNRAS, 318, 1093

Fesen R. A., Weil K. E., 2020, ApJ, 890, 15

Fesen R. A. et al., 1999, AJ, 117, 725

Foreman-Mackey D., Hogg D. W., Lang D., Goodman J., 2013, PASP, 125, 306

Fox O. D., Chevalier R. A., Dwek E., Skrutskie M. F., Sugerman B. E. K., Leisenring J. M., 2010, ApJ, 725, 1768

Fransson C. et al., 2005, ApJ, 622, 991

Fransson C. et al., 2014, ApJ, 797, 118

Freudling W., Romaniello M., Bramich D. M., Ballester P., Forchi V., García-Dabló C. E., Moehler S., Neeser M. J., 2013, A&A, 559, A96

Gall C., Hjorth J., 2018, ApJ, 868, 62

Gall C. et al., 2014, Nature, 511, 326

Gallagher J. S. et al., 2012, ApJ, 753, 109

Gerardy C. L., Fesen R. A., Höflich P., Wheeler J. C., 2000, AJ, 119, 2968

Gerasimovic B., 1933, Z. Astrophys., 7, 335

Gomez H. L. et al., 2012, ApJ, 760, 96

Goodman J., Weare J., 2010, Commun. Appl. Math. Comput. Sci., 5, 65

Howarth I. D., Murray J., Mills D., Berry D. S., 2014, Astrophysics Source Code Library, record ascl:1405.016

Howerton S. et al., 2012, Cent. Bureau Electron. Telegrams, 3052, 1

Indebetouw R. et al., 2014, ApJ, 782, 11

Itagaki K. et al., 2007, IAU Circ., 8874, 3

Kirchschlager F., Schmidt F. D., Barlow M. J., Fogerty E. L., Bevan A., Priestley F. D., 2019, MNRAS, 489, 4465

Kirchschlager F., Barlow M. J., Schmidt F. D., 2020, ApJ, 893, 70

Kotak R. et al., 2009, ApJ, 704, 306

Kozma C., Fransson C., 1998, ApJ, 497, 431

Laporte N. et al., 2017, ApJ, 837, L21

Li W. D., Li C., Filippenko A. V., Moran E. C., 1998, IAU Circ., 6829, 1

Liu N., Nittler L. R., Alexander C. M. O. D., Wang J., 2018, Sci. Adv., 4, eaao1054

Long K. S., Blair W. P., Krzeminski W., 1989, ApJ, 340, L25

Long K. S. et al., 2012, ApJ, 756, 18

Lucy L. B., Danziger I. J., Gouiffes C., Bouchet P., 1989, in Tenorio-Tagle G., Moles M., Melnick J., eds, Lecture Notes in Physics Vol. 350, Structure and Dynamics of the Interstellar Medium. Springer-Verlag, Berlin, p. 164

Lucy L. B., Danziger I. J., Gouiffes C., Bouchet P., 1991, in Woosley S. E., ed., Supernovae. Springer, New York, p. 82

Maeda K. et al., 2013, ApJ, 776, 5

Matsuura M. et al., 2011, Science, 333, 1258

Matsuura M. et al., 2015, ApJ, 800, 50

Mattei J., Johnson G. E., Rosino L., Rafanelli P., Kirshner R., 1979, IAU Circ., 3348, 1

Mauerhan J., Smith N., 2012, MNRAS, 424, 2659

Mauney C. M., Lazzati D., 2018, Mol. Astrophys., 12, 1

Meikle W. P. S. et al., 2007, ApJ, 665, 608

Meyer M. J. et al., 2004, MNRAS, 350, 1195

Micelotta E. R., Dwek E., Slavin J. D., 2016, A&A, 590, A65

Milisavljevic D., Fesen R. A., Kirshner R. P., Challis P., 2009, ApJ, 692, 839

Milisavljevic D., Fesen R. A., Chevalier R. A., Kirshner R. P., Challis P., Turatto M., 2012, ApJ, 751, 25

Milisavljevic D. et al., 2013, ApJ, 770, L38

Milisavljevic D., Patnaude D. J., Chevalier R. A., Raymond J. C., Fesen R. A., Margutti R., Conner B., Banovetz J., 2018, ApJ, 864, L36

Monard L. A. G. et al., 2011, Cent. Bureau Electron. Telegrams, 2946, 1

Montes M. J., Weiler K. W., Van Dyk S. D., Panagia N., Lacey C. K., Sramek R. A., Park R., 2000, ApJ, 532, 1124

Morgan H. L., Edmunds M. G., 2003, MNRAS, 343, 427

Nath B. B., Laskar T., Shull J. M., 2008, ApJ, 682, 1055

Niculescu-Duvaz M., Barlow M. J., Bevan A., Milisavljevic D., De Looze I., 2021, MNRAS, 504, 2133

Nozawa T., Kozasa T., Umeda H., Maeda K., Nomoto K., 2003, ApJ, 598, 785

Nozawa T. et al., 2008, ApJ, 684, 1343

Ott U., Stephan T., Hoppe P., Savina M. R., 2019, ApJ, 885, 128

Owen P. J., Barlow M. J., 2015, ApJ, 801, 141

Panagia N. et al., 1980, MNRAS, 192, 861

Patnaude D. J., Loeb A., Jones C., 2011, New Astron., 16, 187

Pennypacker C. et al., 1986, IAU Circ., 4219, 1

Pojmanski G., Pojmanski G., 2007, IAU Circ., 8875, 1

Pozzo M., Meikle W. P. S., Fassia A., Geballe T., Lundqvist P., Chugai N. N., Sollerman J., 2004, MNRAS, 352, 457

Pozzo M., Meikle W. P. S., Fassia A., Geballe T., Lundqvist P., Chugai N. N., Sollerman J., 2005, in Turatto M., Benetti S., Zampieri L., Shea W., eds, ASP Conf. Ser. Vol. 342, 1604-2004: Supernovae as Cosmological Lighthouses. Astron. Soc. Pac., San Francisco, p. 337

Priestley F. D., Barlow M. J., De Looze I., 2019, MNRAS, 485, 440

Priestley F. D., Barlow M. J., De Looze I., Chawner H., 2020, MNRAS, 491, 6020

Priestley F. D., Chawner H., Matsuura M., De Looze I., Barlow M. J., Gomez H. L., 2021, MNRAS, 500, 2543

Rho J. et al., 2008, ApJ, 673, 271

Rho J., Reach W. T., Tappe A., Hwang U., Slavin J. D., Kozasa T., Dunne L., 2009, ApJ, 700, 579

Rho J. et al., 2018, MNRAS, 479, 5101

Ripero J. et al., 1993, IAU Circ., 5731, 1

Rosino L., 1986, IAU Circ., 4202, 1

Sabater J., Verdes-Montenegro L., Leon S., Best P., Sulentic J., 2012, A&A, 545, A15

Sahu D. K., Anupama G. C., Srividya S., Muneer S., 2006, MNRAS, 372, 1315

Sandstrom K. M., Bolatto A. D., Stanimirovic S., van Loon J. T., Smith J. D. T., 2009, ApJ, 696, 2138

Sarangi A., Cherchneff I., 2013, ApJ, 776, 107

Sarangi A., Cherchneff I., 2015, A&A, 575, A95

Sarangi A., Dwek E., Arendt R. G., 2018, ApJ, 859, 66

Silverman J. M., Cenko S. B., Miller A. A., Nugent P. E., Filippenko A. V., 2012, Cent. Bureau Electron. Telegrams, 3052, 2

Silvia D. W., Smith B. D., Michael Shull J., 2010, ApJ, 715, 1575

Slavin J. D., Dwek E., Mac Low M.-M., Hill A. S., 2020, ApJ, 902, 135

Sluder A., Milosavljević M., Montgomery M. H., 2018, MNRAS, 480, 5580

Smith N., Foley R. J., Filippenko A. V., 2008, ApJ, 680, 568

Smith N., Silverman J. M., Filippenko A. V., Cooper M. C., Matheson T., Bian F., Weiner B. J., Comerford J. M., 2012, AJ, 143, 17

Smith N. et al., 2017, MNRAS, 466, 3021

Soderberg A. et al., 2012, Astron. Telegram, 3968, 1

Stoll R., Prieto J. L., Stanek K. Z., Pogge R. W., Szczygieł D. M., Pojmański G., Antognini J., Yan H., 2011, ApJ, 730, 34

Storey P. J., Zeippen C. J., 2000, MNRAS, 312, 813

Sugerman B. E. et al., 2006, Science, 313, 196

Sugerman B. E. et al., 2012, ApJ, 749, 170

Szalai T., Vinkó J., 2013, A&A, 549, A79

Szalai T., Vinkó J., Balog Z., Gáspár A., Block M., Kiss L. L., 2011, A&A, 527, A61

Takaki K. et al., 2013, ApJ, 772, 17

Temim T., Dwek E., Arendt R. G., Borkowski K. J., Reynolds S. P., Slane P., Gelfand J. D., Raymond J. C., 2017, ApJ, 836, 129

Tinyanont S. et al., 2016, ApJ, 833, 231

Tinyanont S. et al., 2019, ApJ, 887, 75

Van Dokkum P. G., 2001, PASP, 113, 1420

Van Driel W. et al., 2016, A&A, 595, A118

Watson D., Christensen L., Knudsen K. K., Richard J., Gallazzi A., Michałowski M. J., 2015, Nature, 519, 327

Wesson R., Bevan A., 2021, ApJ, 923, 148

Wesson R., Barlow M. J., Matsuura M., Ercolano B., 2015, MNRAS, 446, 2089

Woosley S. E., Heger A., 2007, Phys. Rep., 442, 269

Yamanaka M., Okushima T., Arai A., Sasada M., Sato H., 2010, Cent. Bureau Electron. Telegrams, 2539, 1

Young T. R., Branch D., 1989, ApJ, 342, L79

Zeippen C. J., 1987, A&A, 173, 410

Zhang X. et al., 2022, MNRAS, 509, 2013

Zsíros S., Nagy A. P., Szalai T., 2022, MNRAS, 509, 3235

Zubko V. G., Mennella V., Colangeli L., Bussoletti E., 1996, MNRAS, 282, 1321

Zwitter T., Munari U., Moretti S., 2004, IAU Circ., 8413, 1

APPENDIX A

In addition to the discussion below of some of the limitations of our DAMOCLES modelling, this appendix contains Table A1 , which summarizes those supplementary dust mass data points taken from the literature and plotted in Fig. 23. Bayesian corner plots for six of the simulations run for this work are also included. The CCSNe modelled with a Bayesian inference and plotted in Figs A1–A6 are SN 1957D, SN 1979C at two epochs, SN 1996cr, SN 2004et, and SN 2011ja. We also include a schematic, in Fig. A7, of the oxygen and hydrogen spatial distributions deduced for three of the Type II-L CCSNe that were modelled, SN 1979C, SN 1986E, and SN 1980K. Finally, we include plots in Figs A8 and A9 that compare the best-fitting DAMOCLES model parameters derived by the manual-fitting process and by the Bayesian process.

A1 Limitations to our DAMOCLES modelling

First, our method is only sensitive to dust distributed cospatially or internally to the emitting gas. For those CCSNe where we only modelled oxygen lines (SN 1957D, SN 1993J, SN 1996cr, and SN 2012au) it is possible our modelling has missed some dust present in any CDS outside of the oxygen shell, a region which would typically be traced by hydrogen gas. However, in our spectra of SN 1979C at 13 150 and 13 907 d, presented in Section 3.2.3, where we have high S/N line profiles of Hα and the forbidden oxygen line doublets, we find that the hydrogen shell is external to the oxygen ejecta and that it is not coupled to any dust, and that red-wing attenuation of the Hα line is caused by dust colocated with the ejecta. It is difficult to say how applicable this scenario is to the other CCSNe for which we have only modelled the oxygen lines.

Secondly, our models are simplified by the fact that they only use amorphous carbon and astronomical silicate dust. Niculescu-Duvaz et al. (2021) showed that varying the type of silicate species does not change optically derived dust masses significantly. Grains such as Al_2O_3, which has been detected in Cas A (Rho et al. 2008), are unlikely to make up a large part of the dust species, due to aluminium being a trace element. Therefore, we do not include Al_2O_3 dust in

our models. The observed line profiles could also be fit with iron grains, which behave similarly to amorphous carbon. Because of its higher mass density, 100 per cent iron grain dust would require a much larger dust mass to fit the line profiles of our sample CCSNe than 100 per cent amorphous carbon.

Degeneracies exist between some of the DAMOCLES model parameters. The clearest way to visualize these is in the corner plots in this appendix. One of the main degeneracies is between the dust mass, M_d, and grain radius, a. This is because the radius of a dust grain affects its absorption and scattering efficiencies, which changes the cross-sectional area available for interaction and hence its opacity. The degeneracy between M_d and a is particularly clear in the bottom left-hand panel in the corner plot for the [O II] 7319, 7330 Å doublet in SN 1979C at day 13 903 (Fig. A3), where it can be seen that larger amorphous carbon dust grains require a higher dust mass to fit the line profile. In this case, as there is no scattering wing in the observed profile, it is difficult to constrain the grain size for a single line. However, from manually fitting the [O I], [O II], and [O III] lines simultaneously we were able to constrain the grain radius, which was well within the uncertainties of the 1D posterior for a. This then allowed us to constrain the dust mass. This was also the case for SN 1996cr. In some cases where the grain radius could be well constrained from the scattering wing, this degeneracy is far less prominent (e.g. bottom left-hand panel in Fig. A6, the Bayesian model for SN 2011ja at day 2259).

If the posterior curve is above zero for all possible values of a given parameter, this means that the model is unable to fully exclude any of these values, and that parameter cannot be considered to be well constrained. In some cases, the grain radius cannot be constrained well at all, such as for the case of SN 2004et at day 646, for which the corner plot can be found in Fig. A5. In cases like this, the minimum dust mass can still be determined for the grain radius at which a dust grain is at its most absorbing, but the maximum value of the dust mass cannot be quantified.

For more complex multicomponent profiles we were not able to run a Bayesian model for every CCSN in our sample. We also did not run Bayesian models for every SN epoch due to time restrictions. In these cases, we derived uncertainties on our dust masses from manual fits by varying the dust mass until the χ^2 value increased by 35 per cent, whilst fixing all other parameters. We did not quantify uncertainties in these cases on the other parameters, and the uncertainty on the dust mass is likely to be smaller using this method than for a Bayesian method, where the dust mass posterior distribution is marginalized over other parameters with which it can be degenerate. Fig. A8 compares the V_{max}, R_{in}/R_{out}, β, and grain radius parameters derived from a manual fit (black arrowheads), with the median values (circles) of the parameters taken from the 1D posterior distribution from Bayesian models, for a range of CCSNe studied in this work. The 16th and 84th quartiles of the 1D distribution for each parameter are plotted as the error bars. Fig. A9 is the same but for the dust mass. For all observations, the manually selected parameters were generally well within the uncertainties determined from the Bayesian models.

Table A1. Sources for all supplementary data points plotted in Fig. 23.

Object	Epoch (d)	M_d ($M_\odot$)	Reference
G11.2−0.3	693 500	0.34 ± 0.14	Chawner et al. (2019)
G54.1+0.3	547 900	1.1 ± 0.8	Temim et al. (2017)
G54.1+0.3	547 900	0.49 ± 0.41	Rho et al. (2018)
Crab	348 955	$(4.0^{+0.9}_{-0.8}) \times 10^{-2}$	De Looze et al. (2019)
G21.5−0.9	317 550	0.29 ± 0.08	Chawner et al. (2019)
G29.7−0.3	306 600	0.51 ± 0.13	Chawner et al. (2019)
Cas A	120 300	0.5 ± 0.1	De Looze et al. (2017)
Cas A	119 700	1.1	Bevan et al. (2017)
Cas A	117 600	0.99 ± 0.10	Niculescu-Duvaz et al. (2021)
SN 1980K	10 958	0.21	Bevan et al. (2017)
SN 1987A	615	$(1.0 \pm 0.2) \times 10^{-3}$	Wesson et al. (2015)
SN 1987A	714	2.0×10^{-4}	Bevan & Barlow (2016)
SN 1987A	714	5.5×10^{-5}	Bevan & Barlow (2016)
SN 1987A	775	$(2.0 \pm 0.20) \times 10^{-3}$	Wesson et al. (2015)
SN 1987A	806	4.0×10^{-4}	Bevan & Barlow (2016)
SN 1987A	806	9.0×10^{-5}	Bevan & Barlow (2016)
SN 1987A	1054	7.5×10^{-4}	Bevan & Barlow (2016)
SN 1987A	1153	$(3.0 \pm 1.0) \times 10^{-3}$	Wesson et al. (2015)
SN 1987A	1478	1.1×10^{-3}	Bevan & Barlow (2016)
SN 1987A	1862	1.2×10^{-3}	Bevan & Barlow (2016)
SN 1987A	2211	3.0×10^{-3}	Bevan & Barlow (2016)
SN 1987A	2875	8.0×10^{-3}	Bevan & Barlow (2016)
SN 1987A	3500	1.4×10^{-2}	Bevan & Barlow (2016)
SN 1987A	3604	1.7×10^{-2}	Bevan & Barlow (2016)
SN 1987A	8515	0.55 ± 0.15	Matsuura et al. (2011)
SN 1987A	8515	0.6 ± 0.2	Wesson et al. (2015)
SN 1987A	9131	0.20	Indebetouw et al. (2014)
SN 1987A	9200	0.8 ± 0.2	Wesson et al. (2015)
SN 1987A	9200	0.6 ± 0.2	Matsuura et al. (2015)
SN 1993J	5844	0.12	Bevan et al. (2017)
SN 1995N	827	6.0×10^{-5}	Wesson et al. (in preparation)
SN 1995N	1589	2.0×10^{-4}	Wesson et al. (in preparation)
SN 1995N	5648	0.10	Wesson et al. (in preparation)
SN 1995N	7858	0.20	Wesson et al. (in preparation)
SN 1998S	359	1.9×10^{-3}	Gall et al. (2014)
SN 1998S	499	1.7×10^{-3}	Sugerman et al. (2006)
SN 1998S	499	4.0×10^{-5}	Meikle et al. (2007)
SN 1998S	678	2.0×10^{-2}	Sugerman et al. (2006)
SN 2004dj	271	2.0×10^{-5}	Szalai et al. (2011)
SN 2004dj	866	$(2.6 \pm 0.6) \times 10^{-4}$	Szalai et al. (2011)
SN 2004dj	1011	$(6.2 \pm 1.4) \times 10^{-4}$	Szalai et al. (2011)
SN 2004dj	1241	$(3.6^{+1.0}_{-0.6}) \times 10^{-4}$	Szalai et al. (2011)
SN 2004et	300	4.0×10^{-5}	Kotak et al. (2009)
SN 2004et	300	7.6×10^{-5}	Fabbri et al. (2011)
SN 2004et	360	6.1×10^{-5}	Kotak et al. (2009)
SN 2004et	360	1.0×10^{-4}	Fabbri et al. (2011)
SN 2004et	406	6.1×10^{-5}	Kotak et al. (2009)
SN 2004et	406	2.2×10^{-4}	Fabbri et al. (2011)
SN 2004et	464	6.9×10^{-5}	Kotak et al. (2009)
SN 2004et	464	5.0×10^{-4}	Fabbri et al. (2011)
SN 2004et	690	9.9×10^{-5}	Kotak et al. (2009)
SN 2004et	690	1.5×10^{-3}	Fabbri et al. (2011)
SN 2004et	736	1.1×10^{-4}	Kotak et al. (2009)
SN 2004et	795	1.4×10^{-4}	Kotak et al. (2009)
SN 2005ad	198	1.0×10^{-5}	Szalai & Vinkó (2013)
SN 2005ad	364	3.0×10^{-6}	Szalai & Vinkó (2013)
SN 2005af	194	4.2×10^{-5}	Szalai & Vinkó (2013)
SN 2005af	399	1.6×10^{-5}	Szalai & Vinkó (2013)
SN 2005af	576	2.6×10^{-5}	Szalai & Vinkó (2013)
SN 2005af	772	7.0×10^{-6}	Szalai & Vinkó (2013)
SN 2005af	940	4.5×10^{-5}	Szalai & Vinkó (2013)

Table A1 – *continued*

| Object	Epoch (d)	M_d ($M_\odot$)	Reference
SN 2005ip	169	$(7.4\pm^{61.8}_{4.3}) \times 10^{-6}$	Bevan et al. (2019)
SN 2005ip	413	$(7.2\pm^{22.3}_{6.2}) \times 10^{-6}$	Bevan et al. (2019)
SN 2005ip	905	$(1.9\pm^{22.6}_{1.8}) \times 10^{-3}$	Bevan et al. (2019)
SN 2005ip	940	5.0×10^{-4}	Fox et al. (2010)
SN 2005ip	2242	$(8.7\pm^{150.0}_{6.5}) \times 10^{-2}$	Bevan et al. (2019)
SN 2005ip	3099	$(7.8\pm^{151.0}_{6.8}) \times 10^{-2}$	Bevan et al. (2019)
SN 2005ip	4075	$(6.9\pm^{152}_{6.2}) \times 10^{-2}$	Bevan et al. (2019)
SN 2006bc	550	2.0×10^{-3}	Gallagher et al. (2012)
SN 2006jc	229	2.9×10^{-4}	Nozawa et al. (2008)
SN 2007it	944	1.0×10^{-4}	Andrews et al. (2011b)
SN 2007it	944	4.6×10^{-5}	Andrews et al. (2011b)
SN 2007oc	250	3.1×10^{-3}	Szalai & Vinkó (2013)
SN 2007oc	415	3.7×10^{-3}	Szalai & Vinkó (2013)
SN 2007od	300	2.5×10^{-4}	Andrews et al. (2010)
SN 2007od	455	4.2×10^{-4}	Andrews et al. (2010)
SN 2010jl	464	7.0×10^{-4}	Bevan et al. (2020)
SN 2010jl	526	$(2.50 \pm 0.75) \times 10^{-4}$	Bevan et al. (2020)
SN 2010jl	526	7.0×10^{-4}	Bevan et al. (2020)
SN 2010jl	915	$(2.0 \pm 0.6) \times 10^{-3}$	Bevan et al. (2020)
SN 2010jl	996	3.0×10^{-3}	Bevan et al. (2020)
SN 2010jl	1286	$(5.0 \pm 1.5) \times 10^{-3}$	Bevan et al. (2020)
SN 2010jl	1367	1.0×10^{-2}	Bevan et al. (2020)
SN 2014C	1623	$(4.5 \pm 0.2) \times 10^{-3}$	Tinyanont et al. (2019)
SN 2018hfm	182	$(2.8\pm^{99.5}_{2.75}) \times 10^{-5}$	Zhang et al. (2022)
SN 2018hfm	389	$(1.0\pm^{38.8}_{0.7}) \times 10^{-4}$	Zhang et al. (2022)
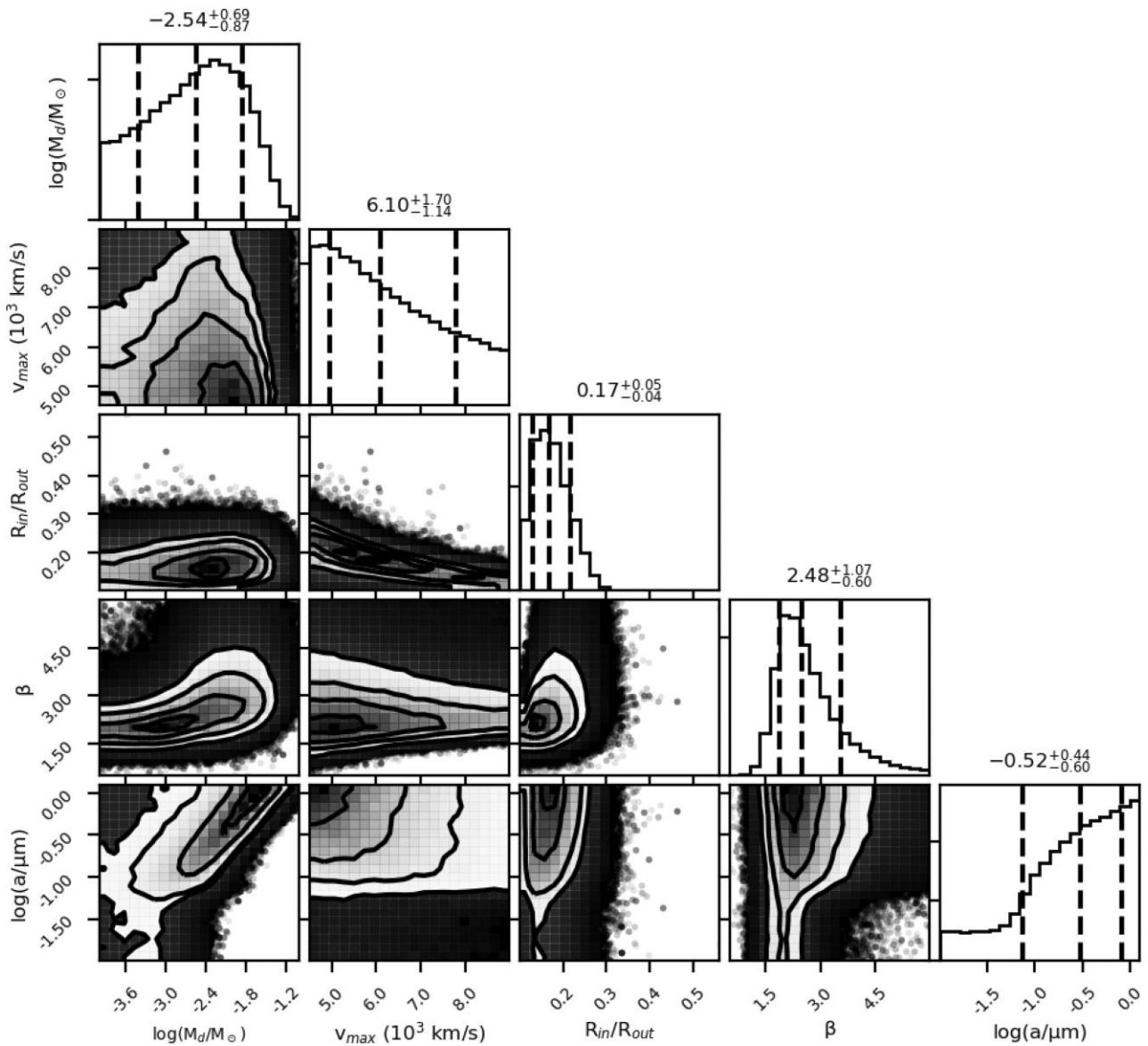
Figure A1. The full posterior probability distribution for the 5D model of SN 1957D's [O III] profile at day 11 371, using 100 per cent carbon dust. The contours of the 2D distributions represent 0.5σ, 1.0σ, 1.5σ, and 2.0σ and the dashed, black vertical lines represent the 16th, 50th, and 84th quantiles for the 1D marginalized probability distributions.
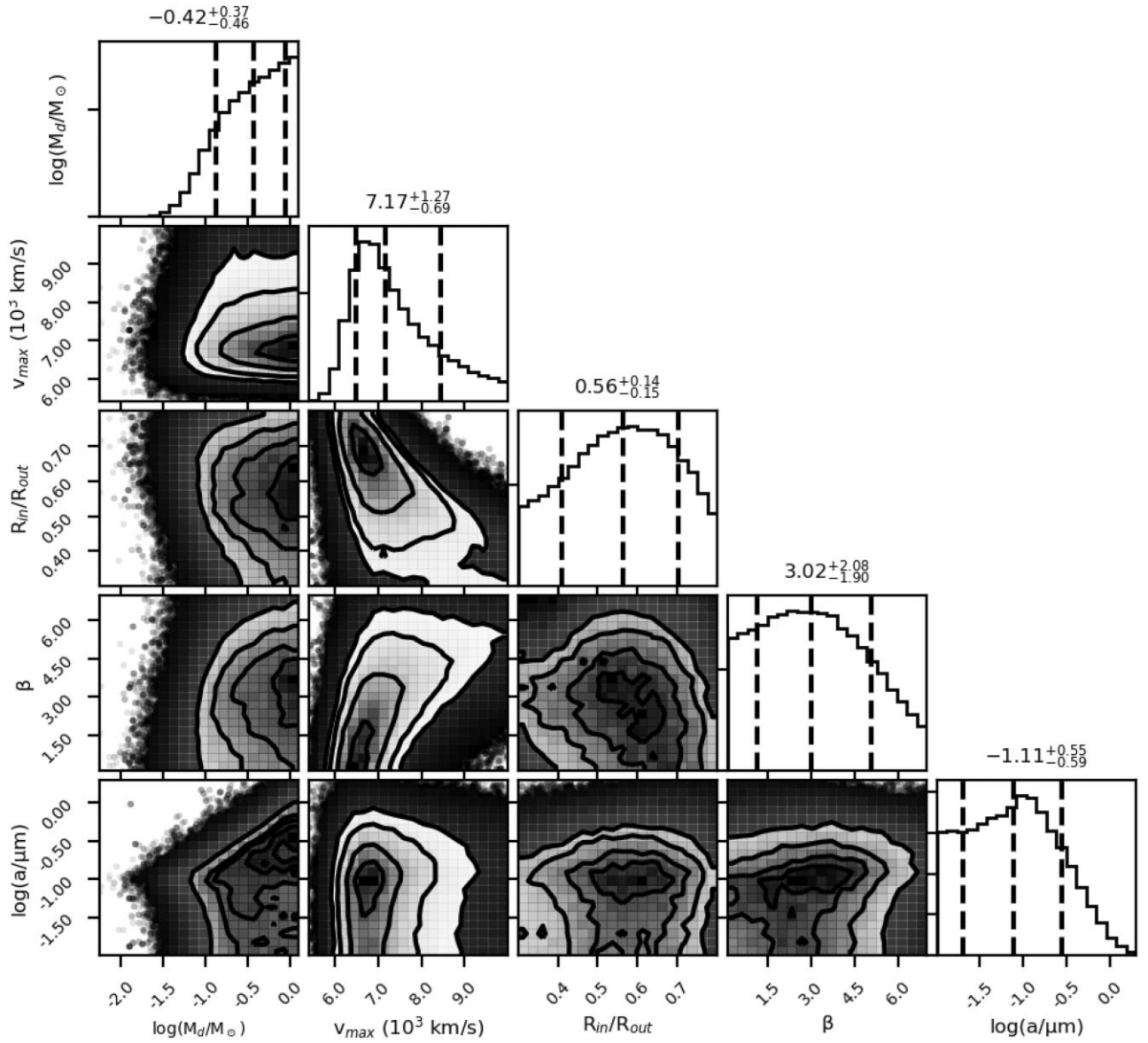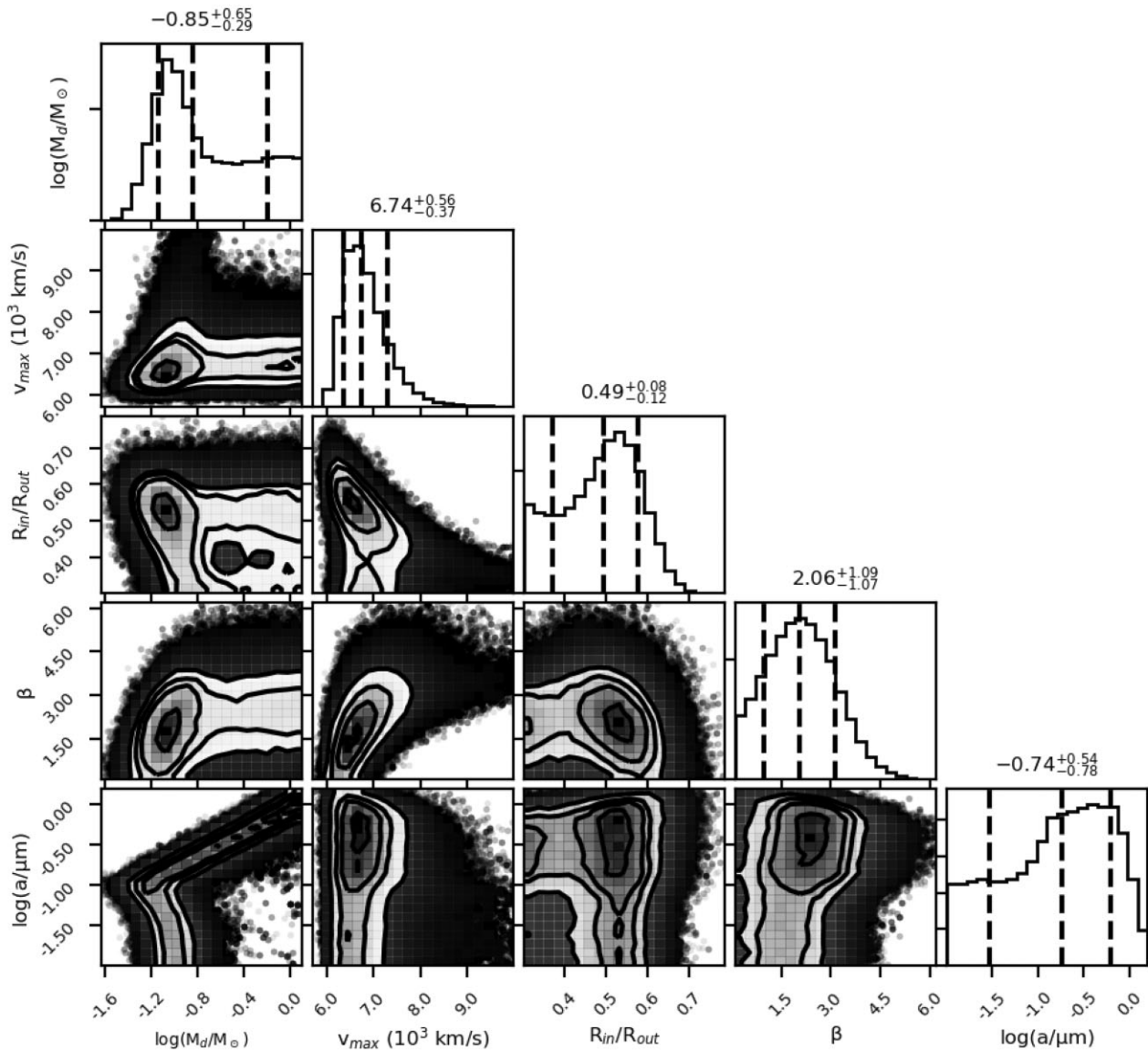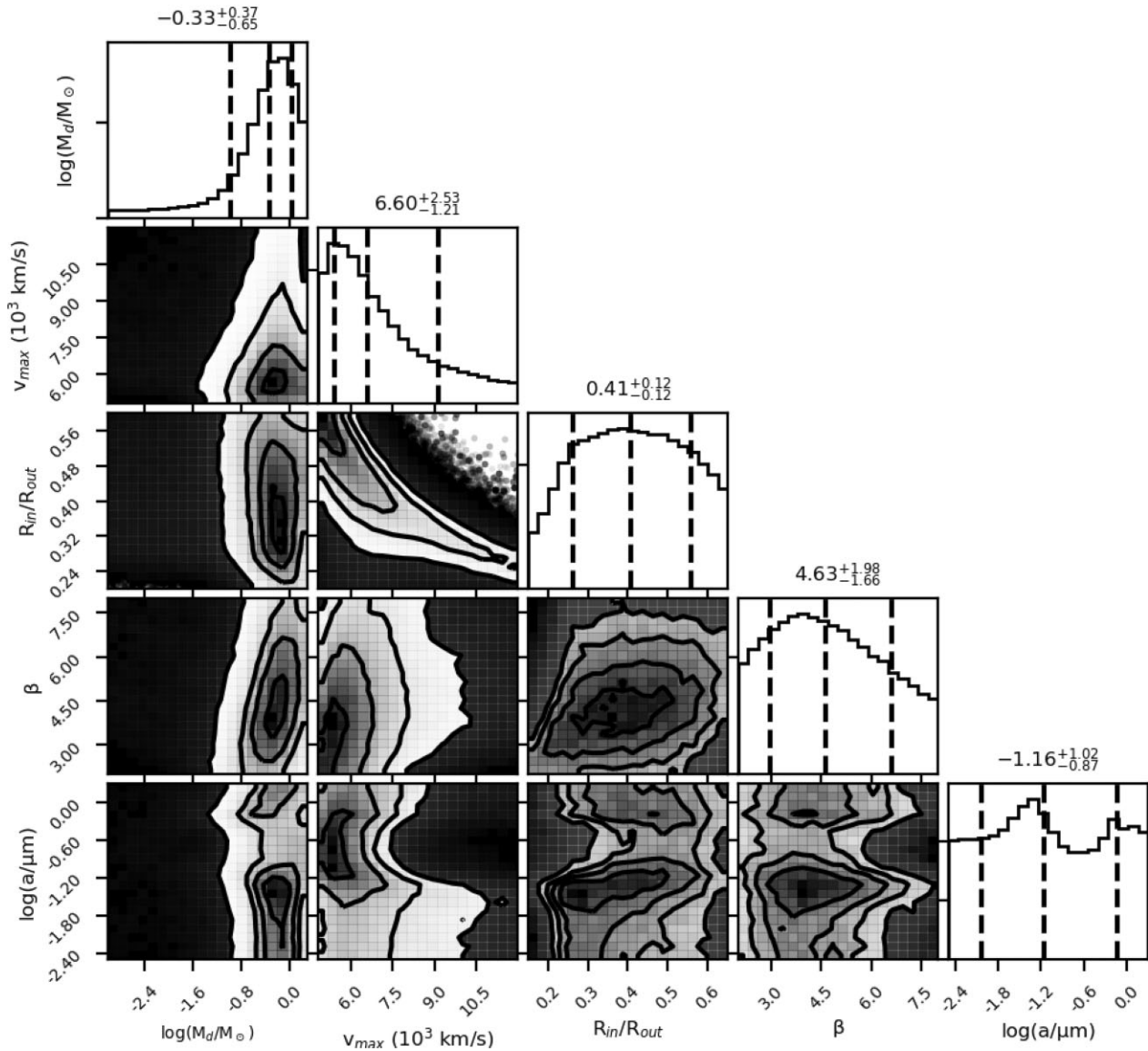
Figure A2. The full posterior probability distribution for the 5D model of SN 1979C's [O II] profile at day 10 575, using 100 per cent carbon dust. The contours of the 2D distributions represent 0.5σ, 1.0σ, 1.5σ, and 2.0σ and the dashed, black vertical lines represent the 16th, 50th, and 84th quantiles for the 1D marginalized probability distributions.
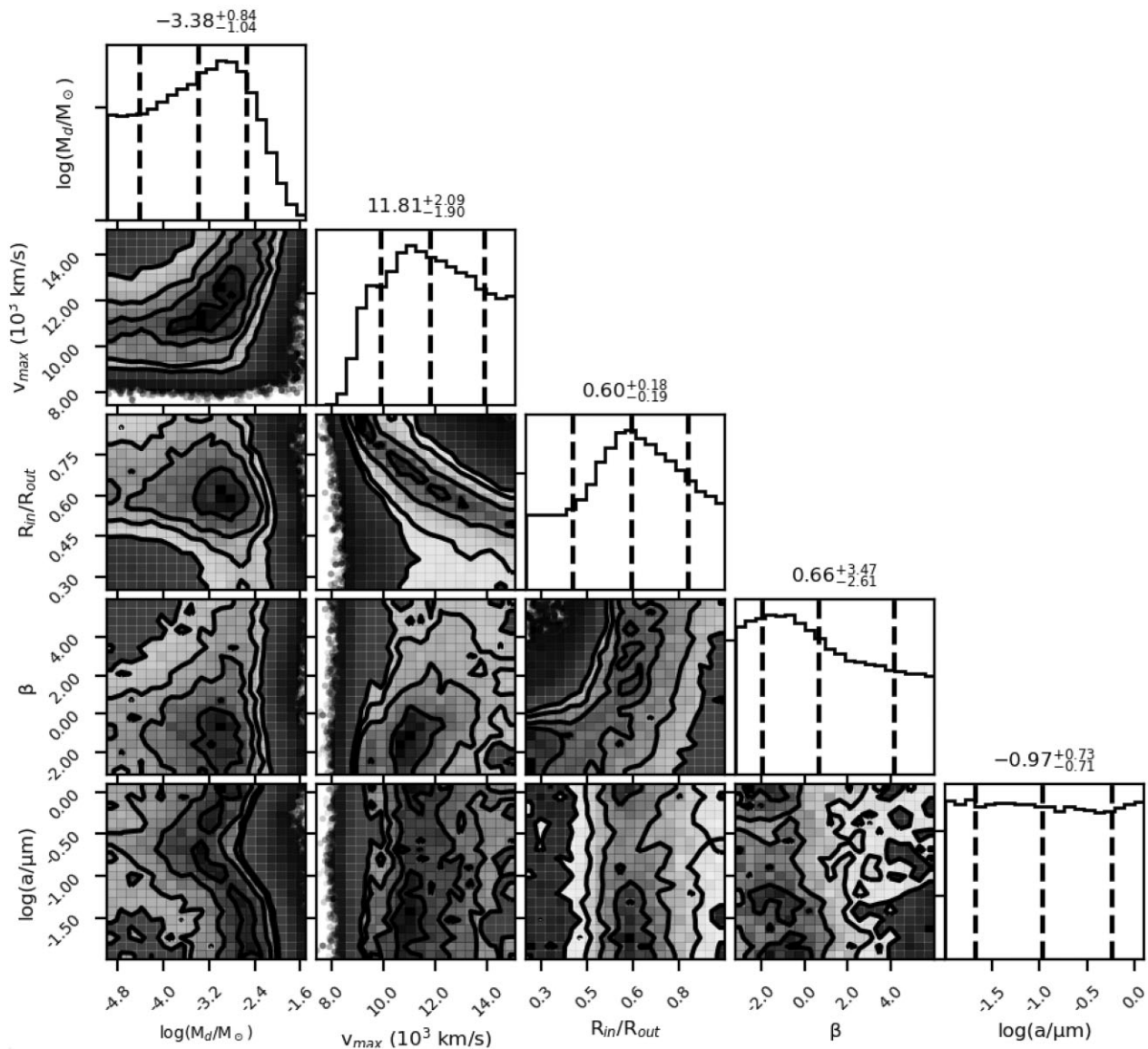
Figure A3. The full posterior probability distribution for the 5D model of SN 1979C's [O II] 7319, 7330 Å profile at day 13 903, using 100 per cent carbon dust. The contours of the 2D distributions represent 0.5σ, 1.0σ, 1.5σ, and 2.0σ and the dashed, black vertical lines represent the 16th, 50th, and 84th quantiles for the 1D marginalized probability distributions.

Figure A4. The full posterior probability distribution for the 5D model of SN 1996cr's [O II] and [O III] profiles at day 7370, using 100 per cent astronomical silicate dust. The contours of the 2D distributions represent 0.5σ, 1.0σ, 1.5σ, and 2.0σ and the dashed, black vertical lines represent the 16th, 50th, and 84th quantiles for the 1D marginalized probability distributions.

Figure A5. The full posterior probability distribution for the 5D model of SN 2004et's Hα profile at day 646, using 100 per cent silicate dust. The contours of the 2D distributions represent 0.5σ, 1.0σ, 1.5σ, and 2.0σ and the dashed, black vertical lines represent the 16th, 50th, and 84th quantiles for the 1D marginalized probability distributions.
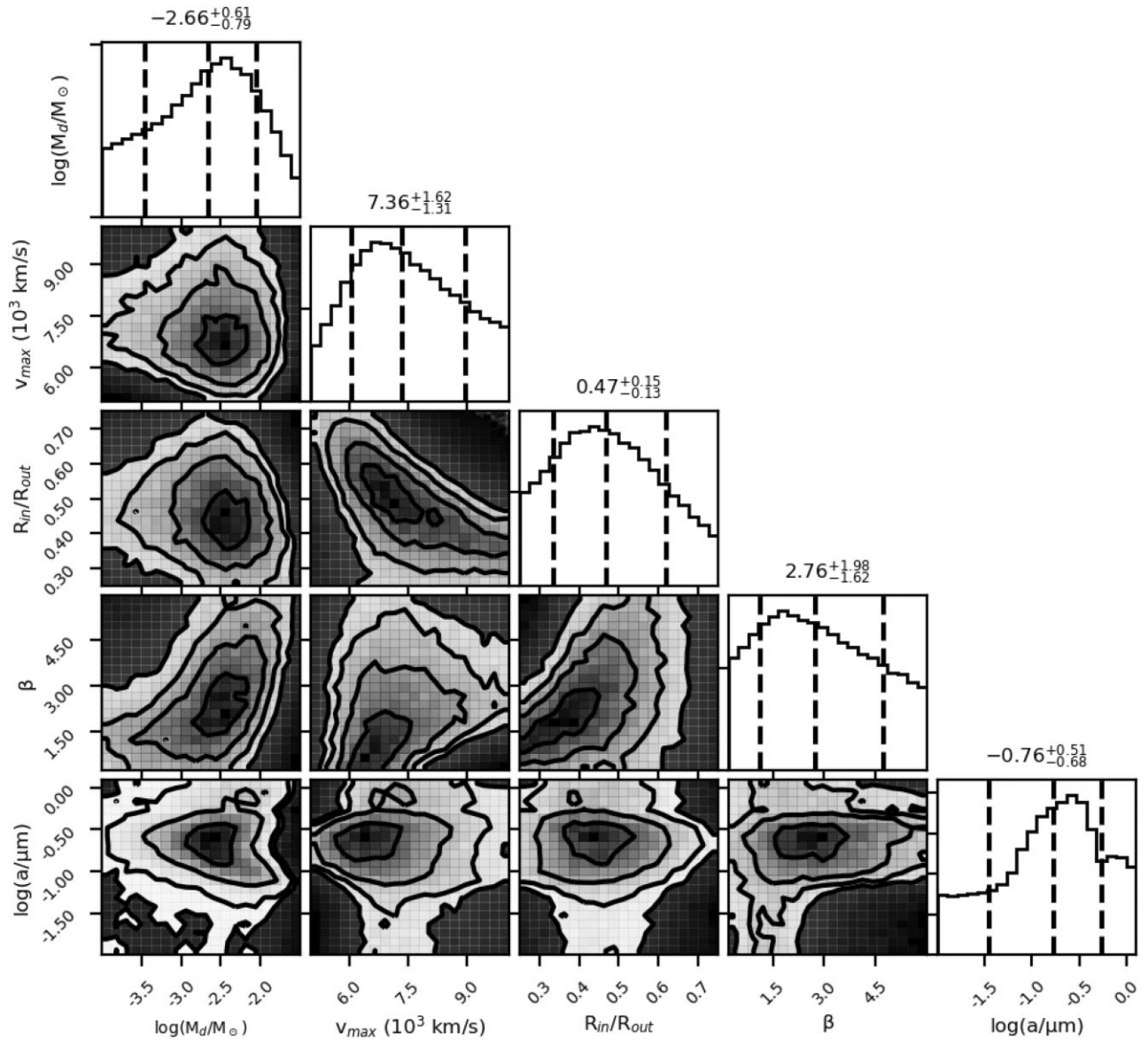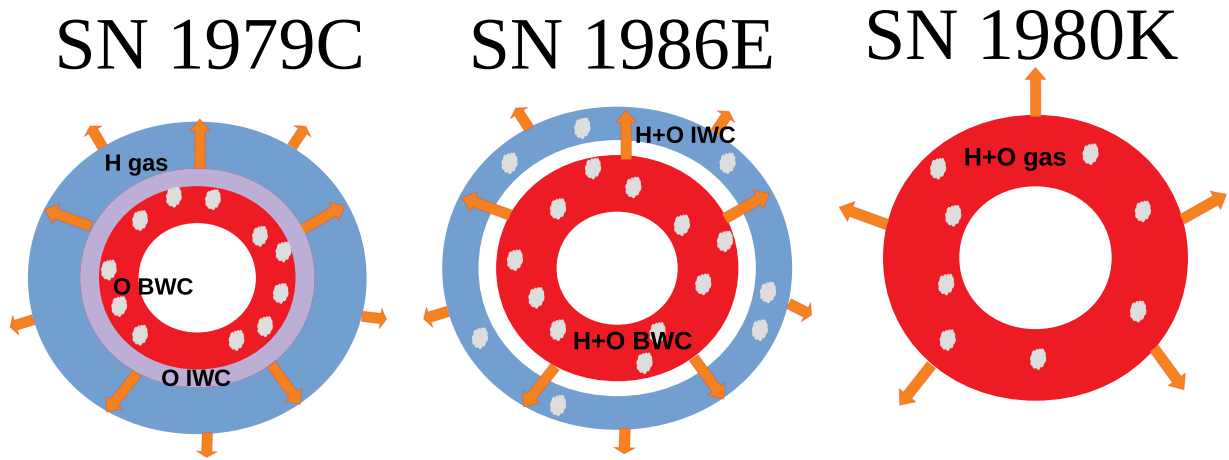
Figure A6. The full posterior probability distribution for the 5D model of SN 2011ja's Hα profile at day 2259, using 100 per cent silicate dust. The contours of the 2D distributions represent 0.5σ, 1.0σ, 1.5σ, and 2.0σ and the dashed, black vertical lines represent the 16th, 50th, and 84th quantiles for the 1D marginalized probability distributions.

Figure A7. Geometry of the Hα and oxygen line emission shells in the Type II-L SN 1979C, SN 1986E, and SN 1980K, as deduced from our DAMOCLES modelling. IWC stands for intermediate-width component and BWC stands for broad-width component. Small grey clouds represent the presence of dust. SN 1998S was deduced to have the same geometry as SN 1980K.
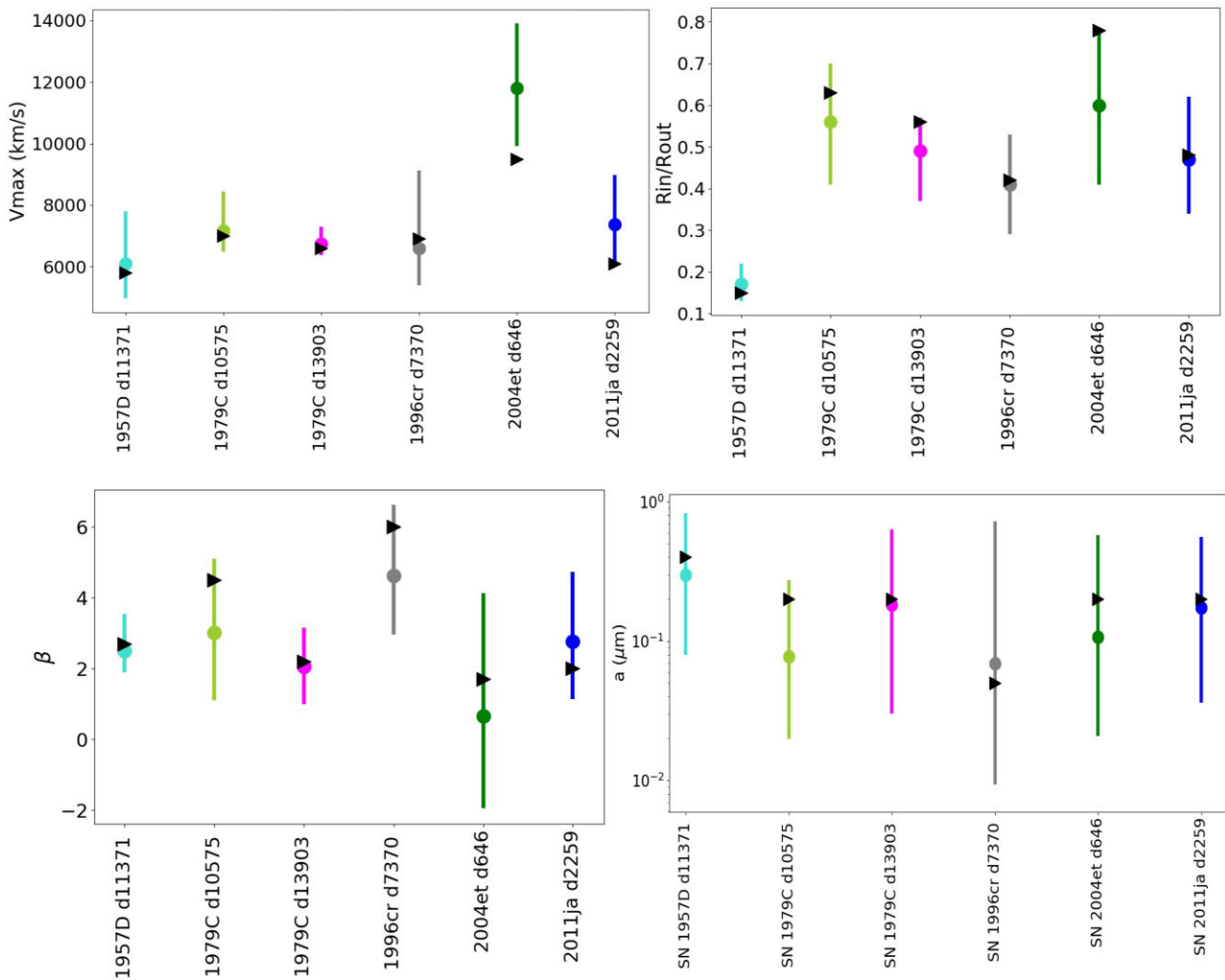

Figure A8. The V_{max}, R_{in}/R_{out}, β, and $\log(a)$ parameters derived from manual fits (black arrowheads), and the median values (circles) of the same parameters taken from the 1D posterior distribution from Bayesian models, with the 16th and 84th quartile of the distribution as the uncertainty limits, for a range of CCSNe studied in this work.
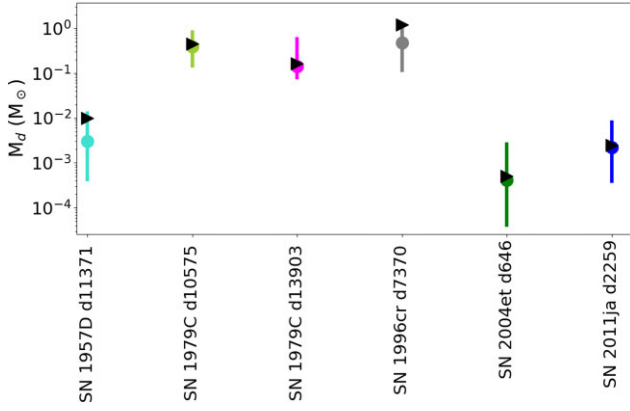
Figure A9. The dust masses, M_d, derived from a manual fit (black arrowheads), and the median values (circles) of the same parameter taken from the 1D posterior distribution from Bayesian models, with the 16th and 84th quartile of the distribution as the uncertainty limits, for a range of CCSNe studied in this work.

This paper has been typeset from a TeX/LaTeX file prepared by the author.